Design and Development of Rechargeable Proton Battery

विद्या वाचस्पति की उपाधि की अपेक्षाओं की आंशिक पूर्ति में प्रस्तुत शोध प्रबंध
A thesis submitted in partial fulfillment of the requirements of the degree of Doctor of Philosophy

द्वारा / By

छात्र का नाम / Name of the Student:
नीतू सी डी/
Neethu C D

पंजीकरण सं. / Registration No.:
20173537

शोध प्रबंध पर्यवेक्षक/ Thesis Supervisor:
प्रोफेसर मुहम्मद मुस्तफा ओ.टी./
Prof. Muhammed Musthafa O. T.

भारतीय विज्ञान शिक्षा एवं अनुसंधान संस्थान पुणे
INDIAN INSTITUTE OF SCIENCE EDUCATION AND RESEARCH PUNE

2024

Dedicated to,

My Parents

भारतीय विज्ञान शिक्षा एवं अनुसंधान संस्थान, पुणे
INDIAN INSTITUTE OF SCIENCE EDUCATION AND RESEARCH, PUNE
[An Autonomous Institution under MHRD, Government of India]
Main Academic Building, Dr Homi Bhabha Road, Pashan, Pune- 411008
www.iiserpune.ac.in

DECLARATION

Name of Student:	Neethu C D
Reg.No.:	20173537
Thesis Supervisor(s):	Prof. Muhammed Musthafa O. T.
Department:	Department of Chemistry
Date of joining program:	1st August 2017
Date of Pre-Synopsis Seminar:	16th October 2023
Title of Thesis:	Design and Development of Rechargeable Proton Battery

I declare that this written submission represents my idea in my own words and where others' ideas have been included; I have adequately cited and referenced the original sources. I declare that I have acknowledged collaborative work and discussions wherever such work has been included. I also declare that I have adhered to all principles of academic honesty and integrity and have not misrepresented or fabricated or falsified any idea/data/fact/source in my submission. I understand that violation of the above will be cause for disciplinary action by the Institute and can also evoke penal action from the sources which have thus not been properly cited or from whom proper permission has not been taken when needed.

The work reported in this thesis is the original work done by me under the guidance of **Prof. Muhammed Musthafa O T,** Associate Professor, Department of Chemistry and Centre for Energy Science, IISER Pune

Signature of the student
Date: 26/03/2024

भारतीय विज्ञान शिक्षा एवं अनुसंधान संस्थान, पुणे
INDIAN INSTITUTE OF SCIENCE EDUCATION AND RESEARCH, PUNE
[An Autonomous Institution under MHRD, Government of India]
Main Academic Building, Dr Homi Bhabha Road, Pashan, Pune- 411008
www.iiserpune.ac.in

CERTIFICATE

This is to certify that this thesis entitled **"Design and Development of Rechargeable Proton Battery"** towards the partial fulfilment of Ph.D. programme at the Indian Institute of Science Education and Research, Pune represents original research carried out by **Neethu C D** at Indian Institute of Science Education and Research, Pune under the supervision of **Prof. Muhammed Musthafa O. T.,** Associate Professor, Department of Chemistry and Centre for Energy Science, IISER Pune during the academic years 2017 - 2023 and that no part of it has been included in any other thesis submitted previously for the award of any degree.

Signature of the Thesis Supervisor
Prof. Muhammed Musthafa O. T.
Associate Professor,
Department of Chemistry and
Centre for Energy Science,
IISER Pune.

26/03/2024
Pune

Acknowledgement

Embarking on the Ph.D. journey has been a transformative experience, and I am deeply indebted to the remarkable individuals who have been instrumental in making this academic pursuit a reality.

Foremost, my heartfelt gratitude goes to my esteemed advisor, Prof. Muhammed Musthafa O T. His unwavering commitment, guidance, and intellectual insights have shaped my research and have definitely challenged me to reach new heights. I do understand being there as a pillar for the students to grow is a commendable task. I am fortunate enough to have one by my side always, ready to discuss work and for welcoming even the stupidest doubts.

I extend my appreciation to my dissertation committee, Prof. Pankaj Mandal & Prof. B.L.V. Prasad, for their invaluable feedback, expertise, and encouragement. The yearly meetings have played a crucial role in refining and enhancing the quality of this work.

A special thanks to Prof. Mohammed Mamlouk and Dr. Ravi Kumar T from the University of Newcastle, United Kingdom for the kind support and help provided during my short time visit as a research student. It has indeed left an indelible mark on my academic journey.

To my fellow colleagues, especially my seniors, your camaraderie, discussions, and shared experiences have made this journey more enriching and enjoyable. I treasure every moment spent with all of you. Indeed, I consider myself to be one of the luckiest person to be part of the team. Thank you very much, to the past and present lab mates.

I am profoundly grateful to IISER Pune for providing an intellectually stimulating environment and the necessary resources for my research. The supportive community at our Department of Chemistry has been integral to my growth as a researcher.

To my Appa & Amma, the most important people in my life, I could not have done anything without you both sticking to me with your constant support, encouragement, understanding, love and a lot more. Your belief in me has been my anchor during the most challenging moments of this Ph.D. expedition. My sisters Neena and Jeena, I do owe a huge amount of gratitude for being around me as my protectors. To my all-time stressbusters Sia and Naithan (my niece & nephew) you are the best.

To my friends, you have put up with a lot of my tantrums during this journey. You guys showed me that real friends don't leave you no matter what. I do appreciate the time you spent for me amidst your struggling journeys, definitely, the group calls we had been therapeutic. I would like to convey my regards to my BS-MS batchmates Fawaz, Thasneem, Navya, Akhil, Anita, Surya, Anagha, Kavya[2], Nithin, my BS-MS juniors Raafi, Aisha, Shana, Jayapriya, and all who are still at IISER Pune.

I extend my thanks to the funding agencies, INSPIRE and UKIERI SPARC whose financial support has been crucial in bringing my research to fruition.

This Ph.D. adventure has been a collective effort, and I am sincerely thankful to all who have contributed in various capacities. Your influence has left an indelible mark on my academic and personal growth.

With deepest gratitude,

Neethu C D

Table of contents

List of figures, tables & calculations

Figure 4	*Figure 4: An All-Solid-State Proton Battery. (a) Cyclic Voltammograms of inorganic transition metal oxide in 0.5 M H_2SO_4 at scan rate 10 mV/s which demonstrates the electrochemical hydrogen insertion/deinsertion at a potential as close as hydrogen redox. The decoupling of capacitive and diffusional contributions suggesting the dominant mode of charge storage as diffusion-controlled insertion process (shaded region). (b) In-situ electrochemical Quartz Crystal Microbalance (EQCM) of inorganic transition metal oxide in 0.5 M H_2SO_4 at scan rate 1 mV/s which exhibits the uptake of protons on reduction (black trace) and their release on oxidation (red trace). (c-e) In-situ electrochemical FTIR spectra of inorganic transition metal oxide reveals the conversion of bridged oxygen to doubly bonded oxygen in tungsten trioxide during reduction with simultaneous insertion of protons. Oxidative scan shows its complete reversal. (f) Schematic representation of the battery with hydrogen inserted inorganic transition metal oxide as negative electrode and hydrogen storing organic molecule as positive electrode. (g) Battery cyclic Voltammogram demonstrating proton shuttling between the inorganic transition metal oxide and the organic-quinone molecule on battery discharge and charge. (h,i) In-situ electrochemical RAMAN spectra of inorganic transition metal oxide in the battery mode exhibiting the peak shift (green, blue, and red trace) as well as intensity (black trace) modulation for all three peaks corresponding to the bridged oxygen-tungsten bonds during battery charge discharge. The peak shift is attributed to the alteration in bond length and strength, however intensity modulation points to the associated alteration in crystal symmetry. (j) XPS spectra show the increased contribution of lower oxidation states/reduced states on battery charge.*	*5*
Figure 5	*A Reversible Atmospheric Water Battery. (a) Cyclic Voltammogram showing the hydrogen storage capacity of the Pd based materials (blue trace). (b) IR Spectra exhibiting the presence of hydrophilic functionality in synthesized GO. (c) XPS spectra demonstrate the comparative composition of hydrophilic functionality incorporation. (d) XRD analysis at varying relative humidity (RH%) demonstrating the water uptake capability of GO. (e, f) Dynamic water sorption study and associated data reveal higher water uptake of GO (green trace) compared to Nafion 117 (brown trace). (g) Schematic representation of the battery with Palladium as the electrocatalyst at the negative electrode and iridium/ruthenium oxide as electrocatalyst at the open air positive half-cell and both the half-cells are separated via a GO membrane. (h) Relative resistance in % for GO (green trace) and Nafion 117 (brown trace) showing the difference in resistance provided by each of the membranes at varying operative voltages that in turn rationalize the higher performance of the device with GO. (i) Battery cyclic voltammogram confirming the proton shuttling between electrodes during the operation. (j) In-situ electrochemical mass spectrometry analysis at positive electrode revealing the oxygen evolution (green trace) suggesting atmospheric water splitting. (k) The image of homemade in-situ electrochemical XRD Cell. (l) In-situ electrochemical XRD analysis of the*	*7*

Abbreviations

CE	Counter Electrode
CV	Cyclic Voltammogram
EIS	Electrochemical Impedance Spectroscopy
EQCM	Electrochemical Quartz Crystal Microbalance
GC	Glassy Carbon Electrode
LSV	Linear Sweep Voltammogram
RDE	Rotation Disc Electrode
RE	Reference Electrode
RHE	Reversible Hydrogen Electrode
RRDE	Rotation Ring Disc Electrode
WE	Working Electrode
KL plot	Koutecky-Levich plot

Symbols

A	Area of electrode (cm^2),
C	Concentration (mol cm^{-3}),
C_{dl}	Electrochemical double layer capacitance (F)
C_s	Specific capacitance (F/cm^2)
D	Diffusion coefficient ($cm^2\ s^{-1}$)
F	Faradays constant (96485 C mol^{-1})
i	Current (A)
i_k	Kinetic current (A)
iL	Limiting current (A)
n	No of electrons
	No: of harmonics of QCM crystal
t	Time (s)
λ	Hydration number
	Wavelength (nm)
ω	Rotation rate (rad s^{-1})
β	Symmetry factor
η	Over potential (V)
υ	Scan rate (V/s)
	Kinematic viscosity ($cm^2\ s^{-1}$)
ΔA	Differential absorption
∆f	Change in frequency (Hz),
∆m	Change in mass (g)
ΔR	Relative reflectance

Design and Development of Rechargeable Proton Battery

The pitfalls of the existing energy grid system such as global warming, depletion of fossil fuel resources, and paramount pollution mandate the focus on renewable, and sustainable energy resources[1-3]. The hydrogen economy has long been touted as a promising energy vector because of its prospects for implementing a zero carbon footprint[2-4]. The hydrogen economy consists mainly of three steps, the first being the production of hydrogen. The second is the storage of the produced hydrogen and its transport, and the third is the utilization of this stored hydrogen for energy conversion[3,4]. However, existing technologies/infrastructure do need at least three different devices for the successful implementation of hydrogen economy[4] that introduce enormous technological and engineering challenges apart from significant cost implications.

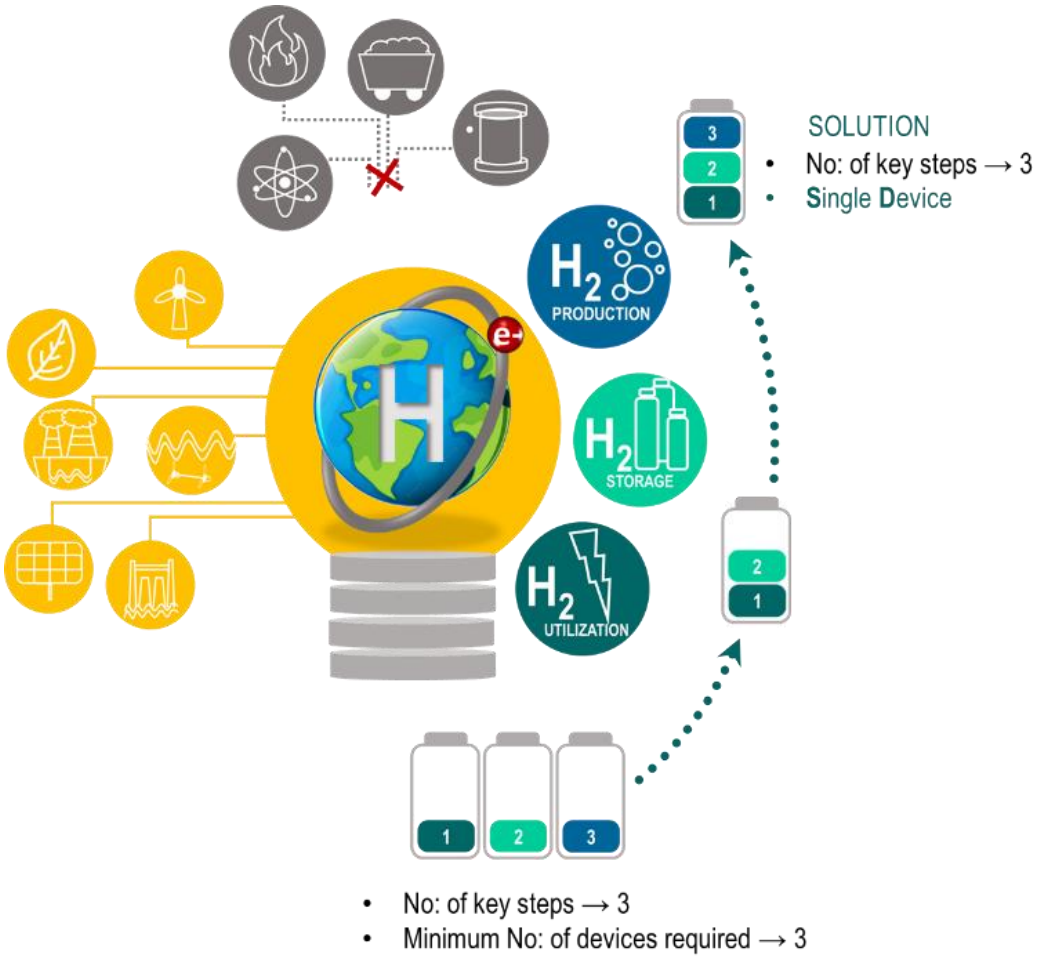

Figure 1: *Schematic representation of the hydrogen battery detailing the sequence of steps involved in fabricating energy devices encompassing all the three key steps of hydrogen economy.*

The prime motive of this thesis is to exploit various methodologies and pathways to couple the key steps of the hydrogen economy under a single energy device. The crust of this research work involves the screening, discerning, synthesizing, elucidating battery-relevant electrochemical parameters, mechanistic understanding, etc., of electrochemically active hydrogen storage materials and molecules and their integration into electrochemical energy devices, so as to successfully fabricate, a single energy device encompassing all the key steps of hydrogen economy (Figure 1). The backbone of these energy devices is primarily shuttling of the protons back and forth between the negative and the positive electrodes during the charging and discharging chemistry. The thesis is subdivided into six main Chapters.

Chapter 1: Introduction

It is a concise account of the current global energy scenario based on non-renewable energy resources and its negative impacts on global climate change, anthropogenic pollution, impacts on the quality of life etc. Special emphasis is given to the Paris Agreement on climate change by the United Nations in 2015 which advocates sustainable development goals by providing directions to shift to an alternative carbon neutral energy economy. In these contexts, the hydrogen economy with its three major steps is introduced as the silver bullet. Its importance in achieving a carbon zero future goal and energy security is highlighted along with the challenges that derail its implementation.

Chapter 2: Materials and Methods

This chapter is a concise description of the materials, procedures, and equipment used, including the details on the experimental setup, data collection and data analysis of various physio-chemical methods.

Chapter 3: An Electrically Chargeable Hydrogen Battery

The Chapter discusses the coupling of gaseous dihydrogen molecule with an electrochemically reversible hydrogen storing organic molecules possessing a positive redox potential for simultaneous energy conversion and hydrogen capture. During the battery discharge, oxidation of the hydrogen molecule at the negative electrode is accompanied by the proton storage in the organic quinone-based molecule at the positive electrode. The electrochemical reversibility of the organic molecule with respect to its hydrogenation/dehydrogenation facilitates the battery recharging via an external potential. This device encompasses two aspects of hydrogen economy such as hydrogen storage as well its utilization in a single energy device, Figure 2.

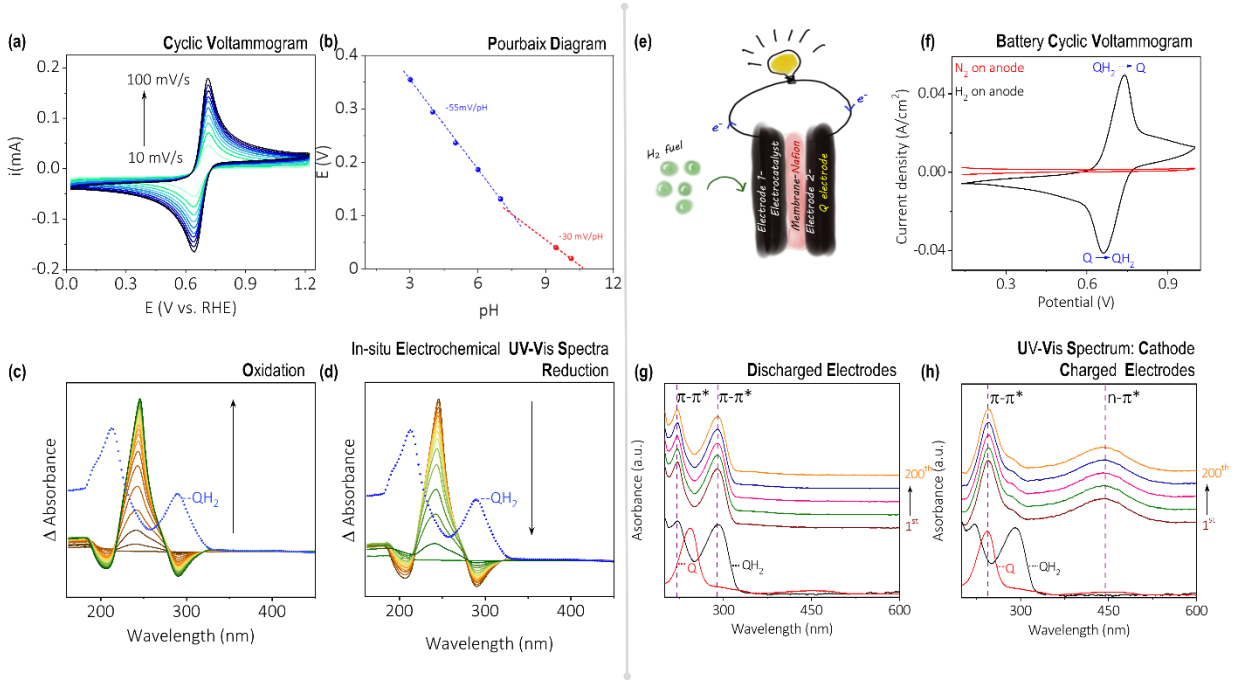

***Figure 2: An Electrically Chargeable Hydrogen Battery**. **(a) Cyclic voltammograms** of hydrogen storing organic-quinone-based molecules (5 mM) in 0.5 M H_2SO_4 at varying scan rates ranging from 10-100 mV/s demonstrating its electrochemically reversible hydrogenation and dehydrogenation. **(b) Pourbaix diagram** detailing the plot of formal potential vs. pH of the organic- quinone-based molecules. **(c, d) In-situ UV-Vis spectroelectrochemistry** of organic-quinone-based molecule during electrochemical oxidation and reduction which also accounts for the absence of any side reactions during the electrochemical redox reactions. **(e) Schematic representation** of rechargeable hydrogen battery with hydrogen as the negative electrode and hydrogen storing organic molecule as the positive electrode. **(f) Battery cyclic Voltammograms** in two electrode device configuration with the organic molecule as the working electrode suggesting its reversible hydrogenation/dehydrogenation. **(g, h) Ex-situ UV-Vis spectra** of the positive organic molecule electrode during battery discharge/charge.*

Chapter 4: An Air Chargeable Hydrogen Battery

This Chapter explores the charging of the developed hydrogen battery in the event of an electric power unavailability, which is important for off-grids application such as in isolated/rural areas and for military operations in challenging geography. In these lines, the possibility of air charging was explored because the electrochemical hydrogenation/dehydrogenation of the organic molecule lies in between the hydrogen redox

and oxygen redox. The fact that the organic molecule demonstrating a negative redox potential with respect to dioxygen suggests that the dehydrogenation of the organic quinone-based molecules or the battery charging chemistry can be triggered in the presence of oxygen. This is also found to reverse the electron flow spontaneously by powering an external load. Therefore, by supplying oxygen, recharging of the battery is actuated along with the generation of electricity. This device again combined two key aspects of the hydrogen economy such as utilization and storage of hydrogen in a single device, Figure 3.

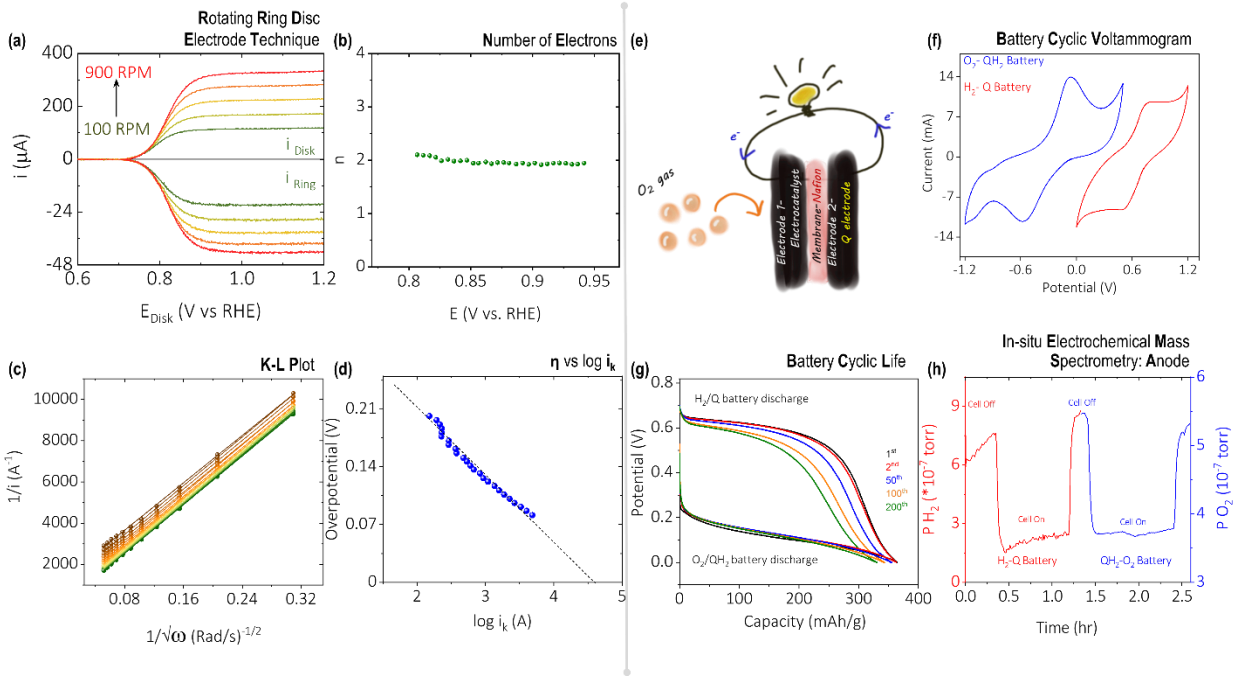

Figure 3: An Air Chargeable Hydrogen Battery. ***(a)Rotating Ring Disc Electrode Studies*** *of hydrogen storing organic- molecules (5mM) in 0.5 M H_2SO_4 at a scan rate of 10 mV/s at varying rotating rates ranging from 100- 900 RPM. The ring electrode was held at reduction potential to sense the products from the disc electrode. The simultaneous disk and ring current prove its electrochemical reversibility and stability at the electrode-electrolyte interface.* ***(b)*** *Associated* ***Koutecky–Levich (K-L) Plot*** *demonstrating a linear fit without a slope change.* ***(c)*** *The calculation of the* ***number of electrons*** *involved in the redox chemistry at varying potentials.* ***(d)*** *The rate constant of reaction and symmetry factor evaluation from the* ***Overpotential vs log of kinetic current (η vs log i_k) plot***. ***(e) Schematic representation*** *of battery fabrication with oxygen at electrode 1 and hydrogen storing organic molecule at electrode 2.* ***(f) Battery cyclic Voltammogram*** *confirming the organic- quinone based molecules undergoing hydrogenation in presence of hydrogen (red trace) and dehydrogenation in presence of oxygen (blue trace).* ***(g) Battery cycle life*** *for 200 cycles.* ***(h) In-situ electrochemical mass spectrometry*** *analysis at electrode 1 showing hydrogen consumption (red trace) during hydrogenation and oxygen consumption (blue trace) during oxygen assisted dehydrogenation.*

Chapter 5: An All-Solid-State Proton Battery

A range of safety challenges are involved in the direct utilization of gaseous hydrogen. In order to address these, hydrogen storage materials with its electrochemical proton insertion/deinsertion potential as close as gaseous hydrogen were explored in this Chapter. Tungsten trioxide WO_3 was opted as the metal oxide for this purpose because of its proton assisted redox chemistry occurring at a potential as close as gaseous hydrogen with a high proton intake capacity and remarkable insertion/deinsertion cyclic stability. Coupling of WO_3 with a hydrogen storing organic molecule whose proton assisted redox chemistry happening at a relatively positive potential allowed the fabrication of a solid-state battery by successfully combining the storage and utilization of hydrogen in a single device, Figure 4.

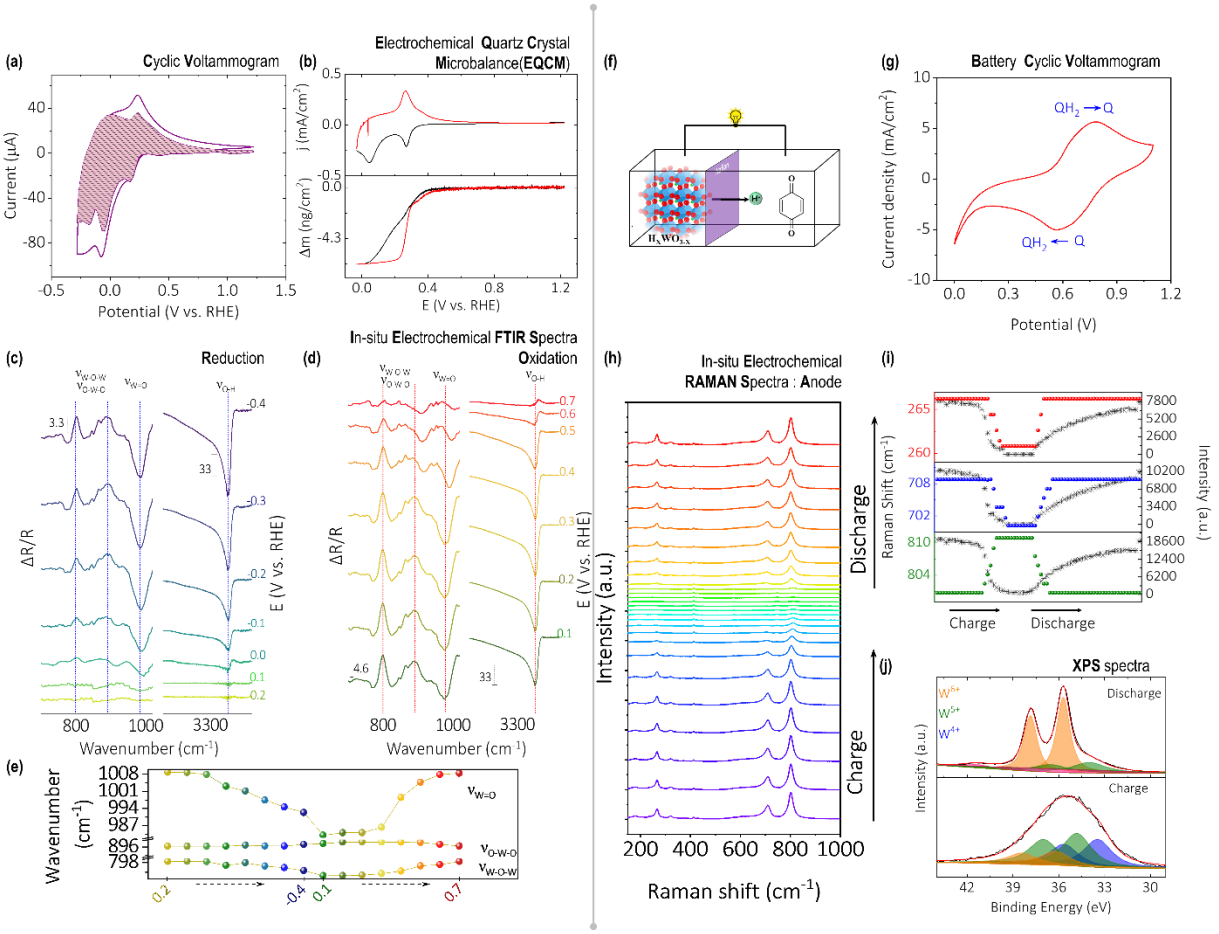

Figure 4: An All-Solid-State Proton Battery. (a) Cyclic Voltammograms *of inorganic transition metal oxide in 0.5 M H_2SO_4 at scan rate 10 mV/s which demonstrates the electrochemical hydrogen insertion/deinsertion at a potential as close as hydrogen redox. The decoupling of capacitive and diffusional contributions suggesting the dominant mode of charge storage as diffusion-controlled insertion process (shaded region).* ***(b) In-situ electrochemical Quartz Crystal Microbalance (EQCM)*** *of inorganic transition*

metal oxide in 0.5 M H_2SO_4 at scan rate 1 mV/s which exhibits the uptake of protons on reduction (black trace) and their release on oxidation (red trace). ***(c-e) In-situ electrochemical FTIR spectra*** *of inorganic transition metal oxide reveals the conversion of bridged oxygen to doubly bonded oxygen in tungsten trioxide during reduction with simultaneous insertion of protons. Oxidative scan shows its complete reversal.* ***(f) Schematic representation*** *of the battery with hydrogen inserted inorganic transition metal oxide as negative electrode and hydrogen storing organic molecule as positive electrode.* ***(g) Battery cyclic Voltammogram*** *demonstrating proton shuttling between the inorganic transition metal oxide and the organic-quinone molecule on battery discharge and charge.* ***(h,i) In-situ electrochemical RAMAN spectra*** *of inorganic transition metal oxide in the battery mode exhibiting the peak shift (green, blue, and red trace) as well as intensity (black trace) modulation for all three peaks corresponding to the bridged oxygen-tungsten bonds during battery charge discharge. The peak shift is attributed to the alteration in bond length and strength, however intensity modulation points to the associated alteration in crystal symmetry.* ***(j) XPS spectra*** *show the increased contribution of lower oxidation states/reduced states on battery charge.*

Chapter 6: A Rechargeable Atmospheric Water Battery

This Chapter majorly discusses attempts to include all the aspects of hydrogen economy in a single device and to achieve this target an extra handle of hydrogen production is introduced into the hydrogen battery system. To meet the primary requirement of hydrogen generation via water electrolysis, a unique pathway of utilizing the atmospheric water was adopted in this Chapter. This strategy of harvesting atmospheric water thereby negates the necessity of ultrapure water and water transport infrastructure. The uptake of atmospheric water into the battery was facilitated by integrating a hydrophilic Graphene Oxide (GO) membrane that can simultaneously shuttle protons with a water uptake capability which is nearly 4 times higher than a commercial Nafion 117 membrane. The electrodes were chosen such that they are active towards water splitting on battery charge and the reversal on battery discharge. The negative half-cell electrocatalyst was chosen in such a way that it not only produces hydrogen but also stores it. This battery has also demonstrated the capability to release hydrogen at the time of discharge leading to electric power generation. Therefore, this device by harvesting atmospheric water connected all the key aspects of the hydrogen economy in a single energy device, Figure 5.

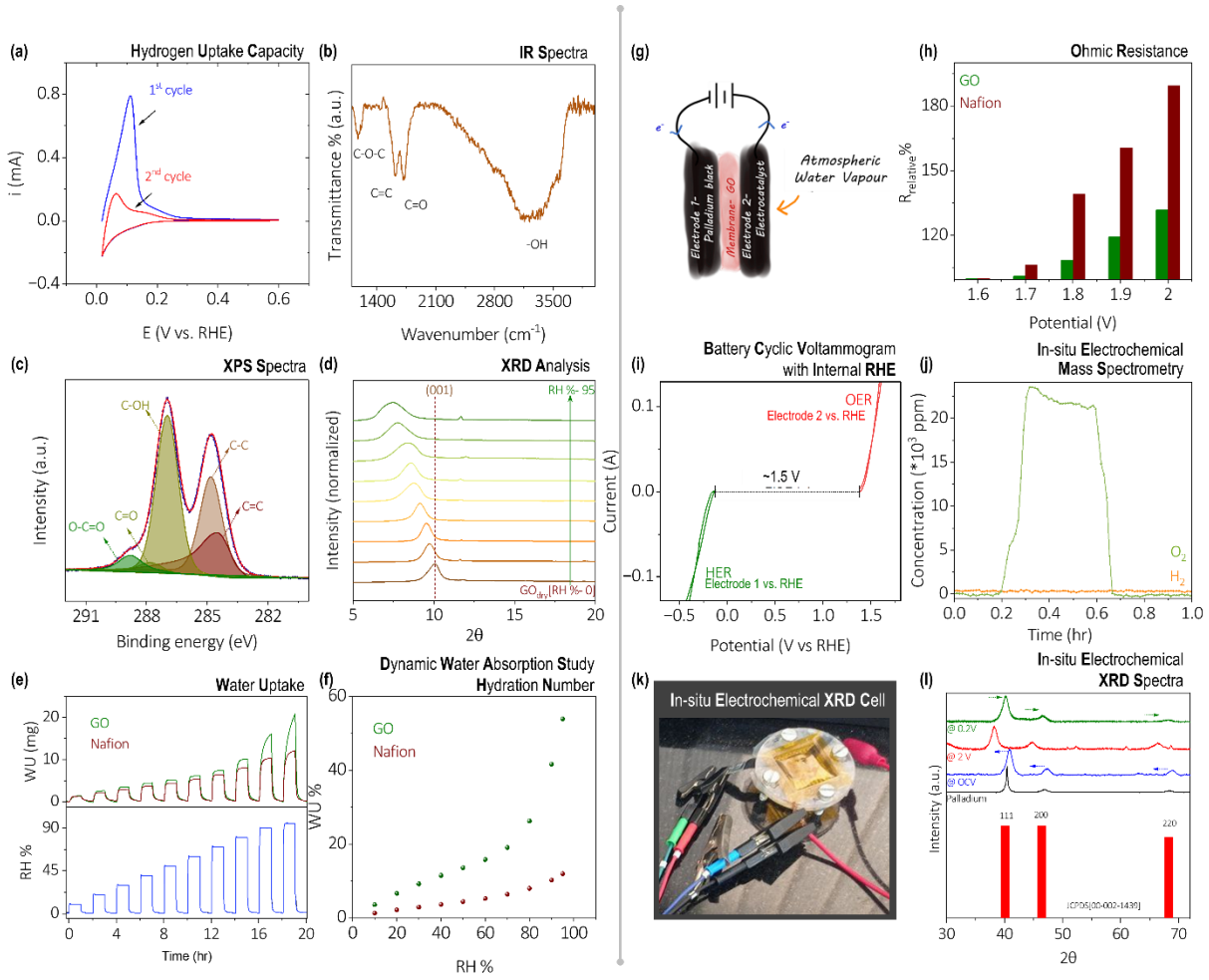

Figure 5: A Reversible Atmospheric Water Battery. (a) Cyclic Voltammogram *showing the hydrogen storage capacity of the Pd based materials (blue trace).* ***(b) IR Spectra*** *exhibiting the presence of hydrophilic functionality in synthesized GO.* ***(c) XPS spectra*** *demonstrate the comparative composition of hydrophilic functionality incorporation.* ***(d) XRD analysis*** *at varying relative humidity (RH%) demonstrating the water uptake capability of GO.* ***(e, f) Dynamic water sorption study*** *and associated data reveal higher water uptake of GO (green trace) compared to Nafion 117 (brown trace).* ***(g) Schematic representation*** *of the battery with Palladium as the electrocatalyst at the negative electrode and iridium/ruthenium oxide as electrocatalyst at the open air positive half-cell and both the half-cells are separated via a GO membrane.* ***(h) Relative resistance*** *in % for GO (green trace) and Nafion 117 (brown trace) showing the difference in resistance provided by each of the membranes at varying operative voltages that in turn rationalize the higher performance of the device with GO.* ***(i) Battery cyclic voltammogram*** *confirming the proton shuttling between electrodes during the operation.* ***(j) In-situ electrochemical mass spectrometry*** *analysis at positive electrode revealing the oxygen evolution (green trace) suggesting atmospheric water splitting.* ***(k)***

*The image of homemade **in-situ electrochemical XRD Cell**. **(I) In-situ electrochemical XRD analysis** of the negative electrode in the battery mode, on charging (red trace) which exhibited peak shift for all three peaks to lower 2 theta values indicating the expansion of the interplanar distance in Pd based materials along with proton storage and the reversal on battery discharge (green trace).*

Chapter 7: Summary and Future Outlook

This chapter provides a brief summary of the work reported in this thesis, Figure 6, with an emphasis on the future outlook.

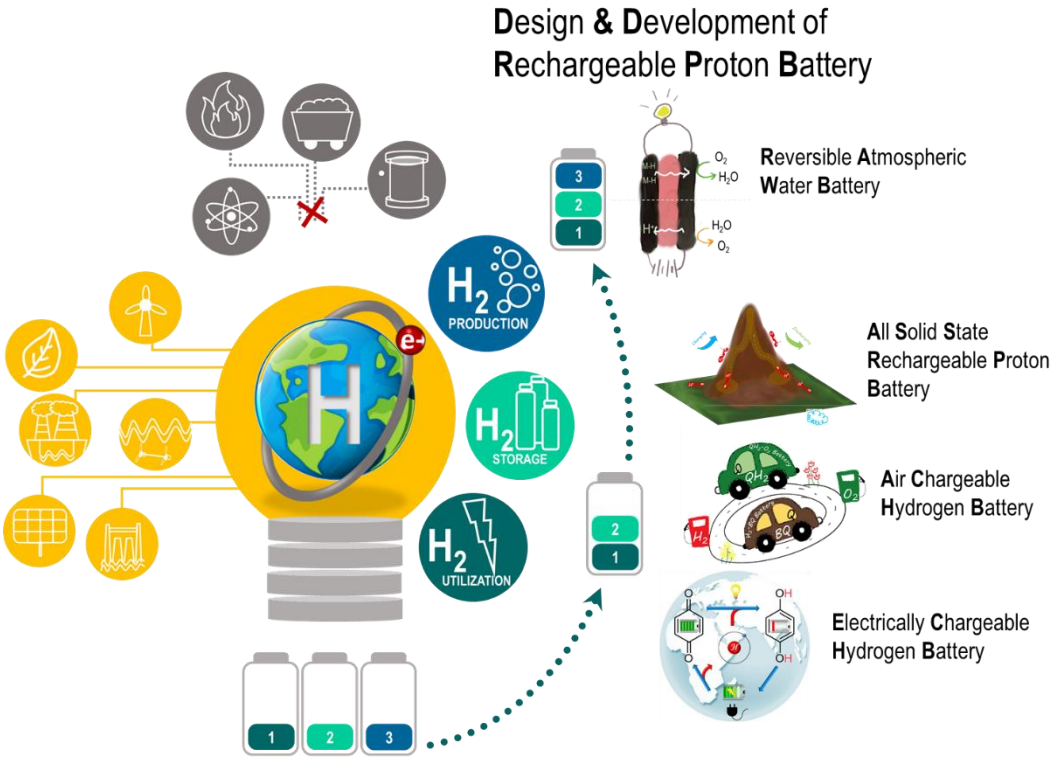

***Figure 6:** Schematics summarizing the work outlined in the thesis.*

References:

1. Welsby, D.; Price, J.; Pye, S.; Ekins, P. *Nature* 2021, ***597* (7875)**, 230–234
2. Schultz, M.; Diehl, T.; Brasseur, G.; Zittel, W.*Science* 2003, ***302* (5645)**, 624–627.
3. Koper, M. T. M. *Nature Chemistry* 2013, ***5* (4)**, 255-256.
4. Bockris, J. O. *Science* 1972, **176 (4041)**, 1323.

Chapter 1:

Introduction

The dawn of industrial revolution has marked energy as the paramount entity which controls economic growth and development of global communities[1 2]. Energy mainly heat, electricity, and fuel have become a necessity for day to day life[2]. Even the gross domestic product (GDP) of several countries today is directly correlated to the generation and utilization of electric energy. Global energy demand (Figure 1.1) is on the rise since then, accounts to nearly about 606 Million terajoules in 2020 [3] and is expected to shoot further by 50% by 2050 [4]. Almost two centuries from 1800s, the energy demand is primarily met by the non-renewable sources – fossil fuels [petroleum, coal, natural gas] resulting in cumulative net CO_2 emission[1] (from 1850 to 2019) of about 2400 $GtCO_2$. Of these, more than half (nearly 58%) occurred between 1850 and 1989 [~1400 $GtCO_2$], and about 42% between 1990 and 2019 [~1000 $GtCO_2$][5]. The booming consumption of fossil fuel leads to huge noticeable impact on the environment, which attracted attention from ecologists, researchers, politicians and economists across the globe[2]. The emission of this greenhouse gases like carbon dioxide (CO_2) cause immense increase in global mean temperatures (global warming) with the threat to disrupt the global carbon cycle. For every 1000 $GtCO_2$ emitted by human activity, global surface temperature rises by 0.45°C (0.25°-0.65°C) which accounts for the increase of global surface temperature by 1.1°C in 2011–2020s from 1850–1900s (Figure 1.2)[4,5]. The ecological imbalances caused by climate change, global warming and pollution contribute to extreme weather conditions including flooding, heat waves and wild fire, storms and droughts, as well as sea level rise and water system disruption, which eventually lead to biodiversity loss, wildlife extinction and food scarcity with unprecedented threats the existence of life on this planet.[2,5,6]

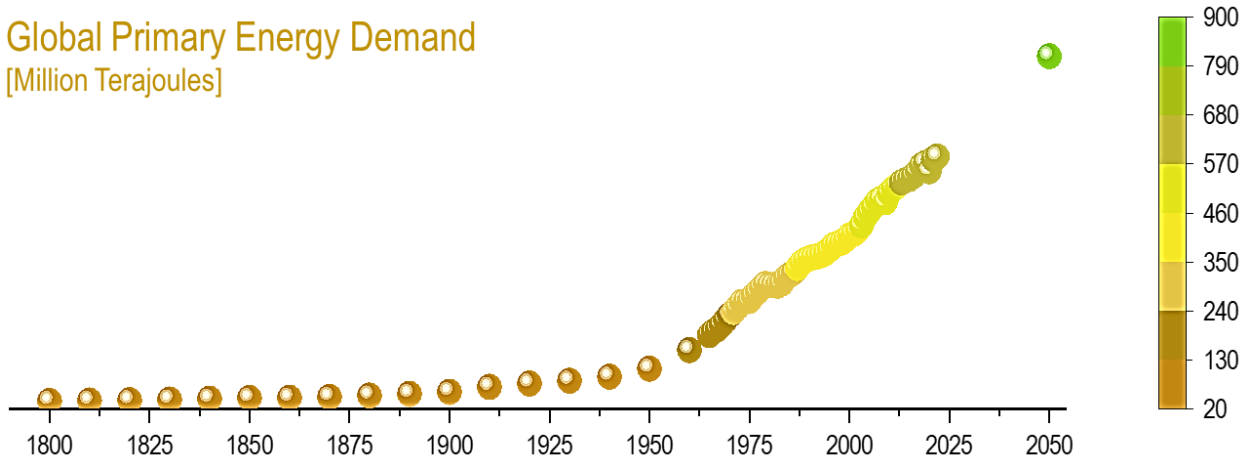

***Figure 1.1**: Global primary energy demand as per the U.S. Energy Information Administration's (EIA)[3] data.*

Taking into consideration of the dependency of economic growth and development on the energy accessibility, we can't just omit energy from our day-to-day life. At the same time continued reliance to the non-renewable/fossil fuel to meet our energy demands would intensify the environmental effects beyond repair and even compromise life existence[7,8]. That is, if we continue to depend on fossil fuel until its exhaustion, reports suggest the reserves still hold more than 10000 $GtCO_2$ and it is safely sequestered if left untouched.[2] But on utilization, it is expected to raise atmospheric CO_2 to around 4 times that of pre- industrial levels, accompanying an average global surface temperature rise by 6.5°C[5]. Even the global warming by 2°C itself is considered to be disastrous as it triggers non-linear irreversible processes leading to drastic climate changes- possibly too harsh for many mammals including mankind[6].

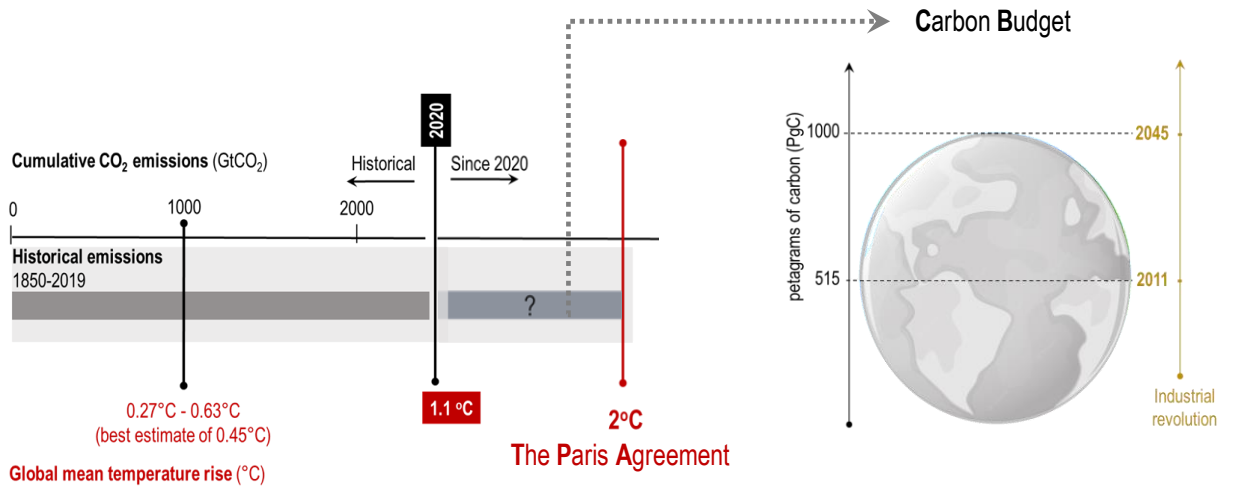

***Figure 1.2**: The Cumulative CO_2 emission past and projected [in $GtCO_2$] along with the associated global temperature changes. Evaluated left out Carbon budget to likely limit the average temperature rises to 2°C [in PgC]. Slightly adapted from* [5,9,10]

Nationally determined contributions (NDCs) demonstrate that the global average inflation of temperature by 1.5°C in the first half of the 2030s[11], and this would make it very hard to control temperature increase by 2°C towards the end of 21st century. Considering its deleterious effects, the UN Climate Change Conference (COP21) held at Paris on 12 December 2015; 196 parties unanimously decided to act towards this major cause and to take measure to get the hold of global average inflation of temperature to 2°C by 2050. Popularly known as The Paris Agreement: a legally binding international treaty on climate change. In-order to achieve this target of 2°C, we have to get hold off the major culprit: atmospheric CO_2 level[12]. Since every 1000 $GtCO_2$ emitted by human activity, global surface temperature rises by 0.45°C (0.25°-0.65°C), the

estimated amount of CO_2 the world can emit while still likely chance of limiting global temperature rise to 2°C from the pre- industrial level is found to be 1000 PgC [PgC : petagrams of carbon or 10^{15} grams of carbon][5]. As per the records, 52% of it have been already consumed by 2011, if the consumption continues at the same rate, it will be exhausted by 2045, leaving us with merely 23 years. This demands an act with immediate effect to reduce the CO_2 emission, and to bring back life on earth to its normalcy[5,13].

***Figure 1.3**: The logos of the proposed seventeen Sustainable Development Goals [SDGs] [14]*

The anthropogenic environmental imbalances, call for an immediate act towards Sustainable development: "the development that meets the needs of the present without compromising the ability of future generations to meet their own needs". The very same year of 2015 in September, witnessed another important policy from UN Sustainable Development Summit in New York titled "Transforming our world: the 2030 Agenda for Sustainable Development". Realizing the immense role of clean energy in achieving sustainable development, it has introduced 17 Sustainable Development Goals (SDGs)[15], Figure 1.3[14]. The proposed SDGs are interlinked and the positive advancement of each of these goals directly/indirectly promotes other goals. Direct promotion of the access to climate-resilient energy i.e. the goals SDGs 7,13 [affordable and clean energy, climate action], indirectly promotes the following as well SDGs 3,4,5,8,9: high-quality education, good health and well-being [at schools and health facilities], gender equality and addressing fragility, conflict, and violence [by leaving no one behind], decent work and economic growth,

industry, innovation, and infrastructure [by stimulating markets and improving regulatory frameworks]. This clearly points out the importance to climate-resilient energy in achieving the clean energy future[4,16–20].

The primary requirement to build a sustainable energy economy for the future is to shift from the existing carbonaceous (fossil fuel/non-renewable energy dependent) energy economy to an alternative which promotes renewable energy (such as sunlight, wind, tides (hydropower), bio mass, and geothermal heat) harvesting economy. This on coupling with a near zero carbon/carbon neutral solutions, it will pave way for clean/green energy solutions, which is the need of the hour. Thus, deep de-carbonization of the existing energy supply with clean, sustainable and renewable energy is inevitable for future energy sustainability and global security[3–5,21].

The clean/green/sustainable energy economy is only possible with the efficient employment of Renewable Energy (RE) resources. However, its variability and intermittency pose challenges for its adaptation. This requires large scale infrastructure to store and release energy to balance the mismatch between variable supply and energy demand. Therefore, energy storage systems and methodologies will be needed to bridge the gap between supply and demand on different time scales[48,17,22].

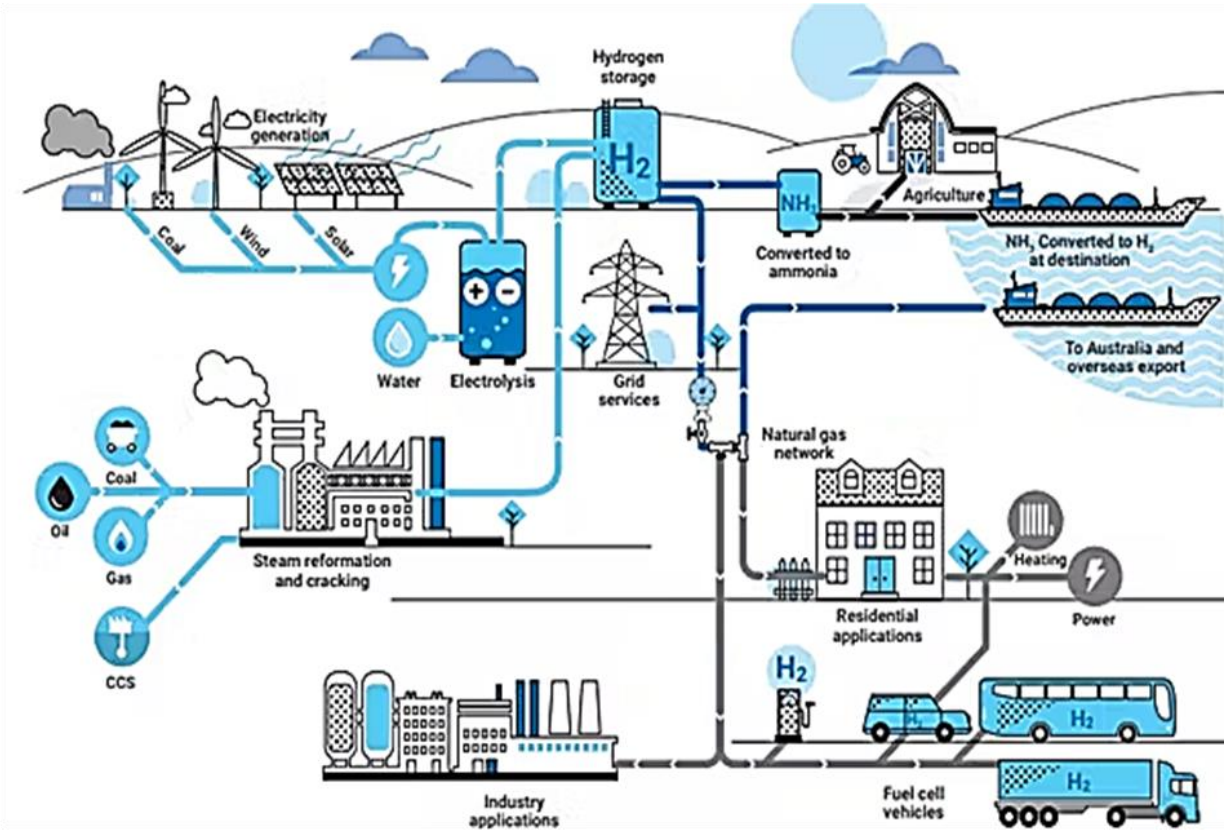

***Figure 1.1.1**: Hydrogen economy pathways* [23]

1.1 Hydrogen Economy:

The scope of utilizing renewable energy to build a sustainable future can be attained with hydrogen as an energy carrier molecule, which is storable, transportable, and utilizable. Hydrogen, the primary element of the periodic table, is the smallest molecule but its profound potential as a clean energy carrier molecule for the global energy transition is the key in sorting all these issues. Hydrogen economy: referring to the use of hydrogen as a low-carbon energy resource[24–31,32]. Gaseous hydrogen as a fuel, is sufficient to power vehicles when burnt in an engine, to produce electricity via fuel cells, or to simply provide heat. It can act as a carrier as well and thereby serve as feedstock or even building blocks for other chemicals. The large-scale renewable energy storage and transport based on hydrogen is gaining attention as it shows potential to fulfill a near 100% renewable energy economy. The hydrogen economy is considered the missing piece of the clean energy puzzle and it consists three key steps. 1) Hydrogen production, hydrogen storage and transportation and 3) hydrogen utilization (Figure 1.1.1).

1.1.1 Key steps of hydrogen economy:

1.1.1.1 Production of hydrogen:

Even though hydrogen is the proposed fuel that can lead us to achieve sustainable goals. the existence of hydrogen in its natural form is not readily available on earth, and it is to be generated from hydrogen-rich compounds. Thereby generation of hydrogen becomes the primary key step of the hydrogen economy. The available pathways often release hydrogen, along with unwanted emissions which is maximum for gasification of coal to net neutral/zero for water electrolysis[23,25,33–35]. To impart the accountability of these unwanted emissions, a universal color spectrum ranging from black to green is in place.

Black, brown, grey, blue, and turquoise hydrogen correspond to hydrogen from coal, natural gas, and methane, which release CO_2 /toxic gases/particulates to the environment[26,32,36]. The hydrogen from the gasification of coal at a high temperature of ~1800 ºC and high pressure of ~100 bar was coined as black/brown hydrogen based on the black/brown coal consumed. The hydrogen produced by steam reformation of natural gas at a high temperature of ~1000 ºC and high pressure of ~25 bar is termed as blue hydrogen when it involves carbon capture (CCU) and grey hydrogen without carbon capture (CCU). The pyrolysis of methane at temperature as high as ~1200 ºC with solid carbon as by-product is titled as turquoise

hydrogen. The involvement of carbonaceous fuel in hydrogen production immensely contributes to the anthropogenic disintegration of our environment [21,26,33].

The most preferred pathway for hydrogen production is via renewable energy-assisted water splitting in an electrolyzer (Scheme 1.1.1). The electrochemical, photo-electrochemical, and photochemical water splitting provide direct pathways for renewable energy conversion to hydrogen[26]. It is important to note that all these pathways occur at room temperature and pressure. This pathway of water electrolysis assisted by renewables is considered to be the cleanest, greenest, and most sustainable pathway since it produces carbon-neutral hydrogen termed as green hydrogen. It is this green hydrogen that is expected to contribute immensely towards the sustainable clean energy development via the hydrogen economy[30,37,38].

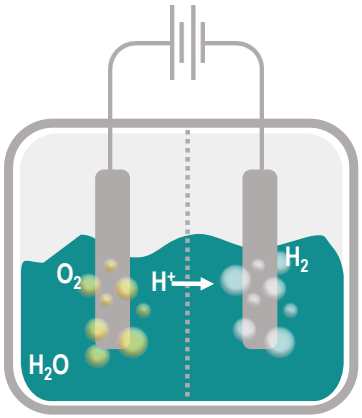

***Scheme 1.1.1**.: Schematic representation of water electrolyzer which split water into its constituent elements, Hydrogen and Oxygen with an external potential bias (which can change based on the source of energy)*

1.1.1.2 Storage/transport of hydrogen:

Hydrogen storage in larger quantities and for longer duration is an important conjunction to the net zero emission targets.[3] The low-density gaseous hydrogen does have the tendency to escape to the atmosphere if not stored. The dimension, efficacy, space utilization, techniques, etc., of the stored hydrogen dictates its application in stationary or mobile applications. The volumetric and gravimetric capacities of the hydrogen storage techniques act as the key to choose for different applications. Existing hydrogen storage strategies can be broadly classified as physical as well as storage in materials[30,39–42].

Physical storage involves compressed hydrogen, liquefied hydrogen, and underground hydrogen storage. Compressed hydrogen is the simplest form of hydrogen storage. Depending upon the applied

pressure this can be categorized into four types (Scheme 1.1.2), however this type of hydrogen storage requires storage tanks for satisfactory storage under specified conditions[39,40]. The common hydrogen tanks used for industrial purpose belongs to Type 1 tanks made of steel which stores hydrogen at a pressure of nearly 200 bar with a gravimetric density of $\sim 1\%$ which is quite low. Type 2 tanks are made of thick aluminum/steel liner which is wrapped with fiber resin composite mesh, and they can store hydrogen at a pressure of nearly 300 bar thereby bringing down the weight by 40% compared to Type 1. Type 3 tanks made of composites with liners covering the entire surface area can hold hydrogen at a pressure of 300-700 bar. Type 4 tanks made of carbon fiber composites as overwrap and high-density polyethylene (HDPE) like polymer as liner, can withstand pressures as high as 750 bar. The gravimetric capacity with type 4 is ~5 times compared to that of type 1. The liquefied hydrogen at -253°C and atmospheric pressure demonstrate an improved gravimetric density of 1.5 times (70.8 kg/m^3) as well as volumetric energy density of 2 times (8.5MJ/T) with respect to hydrogen stored at 700 bar. Liquefaction is a multi-step energy-intensive process which include pathways Linde Hampson liquefaction cycle, Claude liquefaction cycle, and Collins Helium Hydrogen liquefaction cycle. High-pressure hydrogen storage in existing geological structures such as abandoned mines, deserted salt caverns, depleted fossil fuel reserves, etc., impart not only economic benefits but also easiness in integrating it with the distribution channels[39,40].

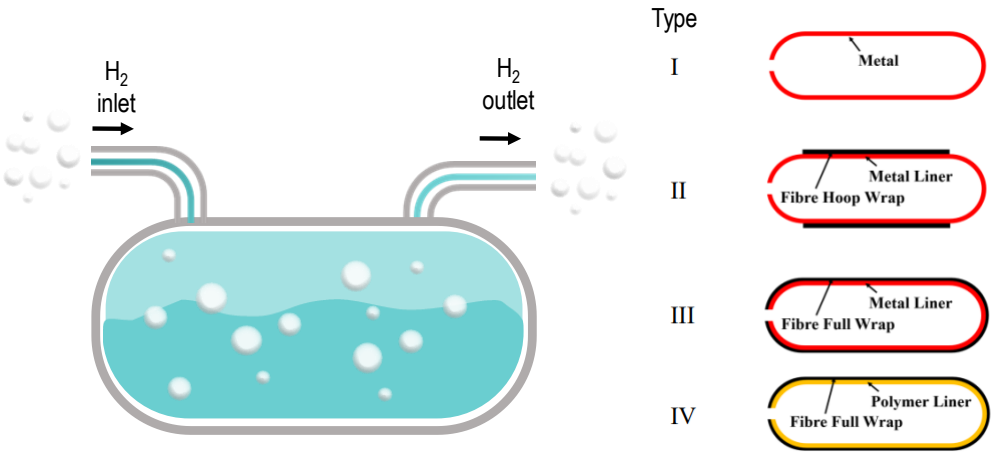

***Scheme 1.1.2**.: Schematic representation of hydrogen storage tanks (on left), its different types and details of materials used (on right) in each type of storage tank. Ref:*[39]

Hydrogen storage in materials imposes extra requirements such as suitable thermodynamic properties, reversible hydrogen sorption/desorption under moderate temperature and pressure, rapid kinetics, easiness of handling and economic implications[41–43]. These materials include carbon-based

materials, carbohydrates, organic materials, metal organic frameworks (MOF), zeolites, metal hydrides (MH) of three types (intermetallic MH, complex MH and chemical MH[4]), chemical hydrides, inorganic nanotubes and clathrates[44,45]. The kinetics and thermodynamics of uptake/release of hydrogen are highly dependent on their type/relative strength of the interaction of hydrogen with the material that in turn leading to three different classes such as physisorption materials, on-board reversible hydrides, and off-board regenerable hydrides[4,5]. Materials such as porous carbon, organic polymers, clathrates, zeolites and MOFs store hydrogen via physisorption on the surface[41–43,45–47]. As per IUPAC, physisorption is the adsorption on the surface of the porous materials via weak Van der Waals interaction which is not expected to alter the electronic structure of the species involved[48]. The absence of activation energy and negligible interaction energy make it reversible with fast adsorption and desorption kinetics. However, the weak Van der Waals interaction affects the storage capacity, in general low at room temperature/pressure but higher at low temperature/high pressure[5]. The on-board reversible hydrides and off-board regenerable hydrides[4,5] fall under chemisorption, as per IUPAC it is the adsorption as a monolayer via strong chemical bonds between the adsorbate and adsorbent[49]. Due to the relatively higher energy for the uptake and release, this types of chemisorption may affect reversibility. The adsorption process involves the dissociation and storage hydrogen covalently/as interstitially bound hydrogen. The endothermic dehydrogenation can support exothermic rehydrogenation, and is best suited for onboard applications, therefore termed as on-board reversible hydride materials. The complex covalent hydrides (metal borohydrides/amides, eg: $LiBH_4$, $NaBH_4$, $Mg(BH_4)_2$, $LiNH_2$, $Mg(NH_2)_2$), interstitial metal hydrides ($LaNi_5H_x$) and covalent metal hydrides (MgH_2, AlH_3) are all belonging to on-board reversible hydride materials. The adsorption process involving the dissociation of hydrogen covalent storage with exothermic dehydrogenation or involving complex hydrogenation process can't be recommended for on board application, termed as Off-board regenerable hydride materials. Hydrocarbons, alane, and ammonia borane fall in this category[41–43,45–47,50,51].

The stored hydrogen should be transported to the site of end usage, the distance between the site of production to utilization and the scale of demand dictates the transportation/ distribution channels. The availability of renewable energy resources at the site can be exploited for on-site hydrogen production and utilization[1]. The compressed hydrogen is the most common one feasible for short-distance transport at a lower hydrogen volume which is generally termed as gaseous trucking[4,34,35]. The more compact form of hydrogen called the liquefied one, with higher gravimetric capacity compared to compressed ones, makes it suitable for longer distance transport which is termed as liquid trucking. To meet the market requirements,

fueling stations and pipeline transportation will be the apt choice. The possibility of utilizing existing natural gas pipelines will be economical as well[14].

1.1.1.3 Utilization of hydrogen:

The advantage of the hydrogen economy lies in the direct utilization of hydrogen in various sectors, including electricity, transport, industries, heating etc. The beauty is that this direct utilization is expected to bring down the hazardous anthropogenic emissions to net zero[4,16,18,30,52].

Hydrogen can be converted to electrical energy with only water as the by-product in a H_2-O_2 fuel cell (Scheme 1.1.3). The electrochemical reaction involves the oxidation of hydrogen oxidation at the negative electrode, releasing protons and electrons (eq. 1.1). Both reach the positive electrode, the electrons travel via an external circuit, and protons shuttles through the proton conducting membrane that combine with oxygen forming water (eq. 1.2). The system gives electricity and water as the by-product (eq. 1.3) and hence it is considered to be the cleanest energy conversion system[53].

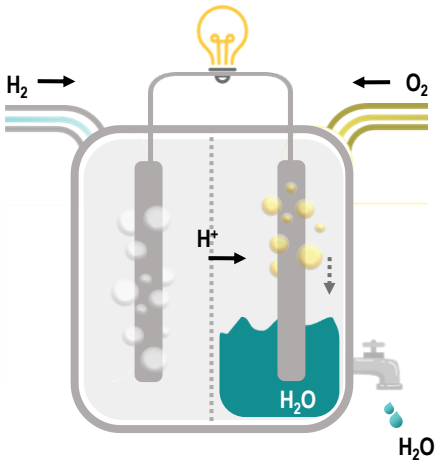

***Scheme 1.1.3**.: Schematic representation of H_2-O_2 fuel cell*

Anode reaction: $2H_2 \rightarrow 4H^+ + 4e^-$ (eq. 1.1)

Cathode reaction: $O_2 + 4H^+ + 4e^- \rightarrow 2H_2O$ (eq. 1.2)

Overall cell reaction: $2H_2 + O_2 \rightarrow 2H_2O$ (eq. 1.3)

The primary industrial consumer; oil refineries utilize hydrogen to remove impurities and thereby upgrade crude oil to heavier crude[54,55]. Chemical production industries such as ammonia and methanol along with several other small-scale chemical processes are the next major consumers. Then iron and steel

industries, where the direct reduction of iron (DRI) route requires hydrogen. The byproduct via the blast furnace route a mixture of gases with hydrogen as well is utilized at the site. High-temperature heat from hydrogen can be an add-up in industries, and the controlled combustion of hydrogen can aid the heating of building structures. The utilization of hydrogen as a fuel in transportation is demonstrated and tested in Light-duty vehicles (Cars and vans), heavy-duty vehicles (trucks and buses), and even in rail. Maritime and aviation demonstration projects are still on the run. The main attraction of the hydrogen economy is the possibility of utilizing green hydrogen not only for power generation but also for its direct employment in hard-to-abate sectors such as industries, heating, and transportation[54,55].

1.1.2. Properties hydrogen

Hydrogen was discovered by 1766/Henry Cavendish and is the primary element of periodic table, with a single electron orbiting its nucleus which is the lightest and simplest one known. It makes up about 90% of all matter and thereby the most abundant element of the universe.[34] It is diatomic gaseous molecule at standard temperature and pressure [STP] is tasteless, odorless, and nontoxic however flammable.

Table 1: Hydrogen properties and specifications. [26,56–58]

Properties	**SI Units**
Isotopes	^{1}H (99.98%), ^{2}H, ^{3}H, (^{4}H-^{7}H Unstable)
Equivalences; Hydrogen solid, liquid and Gas at Pressure = 981 mbar and Temperature = 20 °C	1 kg = 14,104, l= 12,126 m^3
Molecular weight	1.00794 u
Vapor pressure at (-252.8 °C)	101.283 kPa
Density of the gas at boiling point and 1 atm	1.331 kg/m^3
Specific gravity of the gas at 0 °C and 1 atm (air = 1)	0.0696
Specific volume of the gas at 21.1 °C and 1 atm	11.99 m^3/kg
Specific gravity of the liquid at boiling point and 1 atm	0.0710
Density of the liquid at boiling point and 1 atm	67.76 kg/m^3
Boiling point at (101.283 kPa)	-252.8 °C
Freezing/Melting point at (101.283 kPa)	-259.2 °C
Critical temperature	-239.9 °C

Critical pressure	1296.212 kPa, abs
Critical density	30.12 kg/m^3
Triple point	-259.3 °C at 7.042 kPa, abs
Latent heat of fusion at the triple point	58.09 kJ/kg
Latent heat of vaporization at boiling point	445.6 kJ/kg
Solubility in water vol/vol at 15.6 °C	0.019
Dilute gas viscosity at 26 C (299 K)	9 x 10^{-6} Pa s
Molecular diffusivity in air	6.1 x 10^{-5} m^2/s
C_p	14.34 kJ/(kg) (°C)
C_v	10.12 kJ/(kg) (°C)
Ratio of specific heats (C_p/C_v)	1.42
Lower heating value, weight basis	120 MJ/kg
Higher heating value, weight basis	141.8 MJ/kg
Lower heating value, volume basis at 1 atm	11 MJ/m^3
Higher heating value, volume basis at 1 atm	13 MJ/m^3
Stoichiometric air-to-fuel ratio at 27 °C and 1 atm	34.2 kg/kg
Flammable limits in air	4% - 75%
Explosive (detonability) limits	18.2 to 58.9 vol % in air
Maximum combustion rate in air	2.7 to 3.46 m /s
Maximum flame temperature	1526.85 °C
Auto-ignition temperature in air	400 to 571 °C

1.1.3. Benefits of hydrogen economy

1.1.3.1 Flexibility to the power grid:

An instantaneous shift to the green/clean energy economy is impractical. However, the coinciding pathway of the hydrogen economy with both the renewable/non-renewable sources undoubtedly can smooth the transition from the existing fossil fuel based carbonaceous economy, to a sustainable economy reliant on renewable energy resources. The beauty lies in the hydrogen economy that it can sustain primarily on renewable energy resources. Hydrogen is unique as it serves both as a fuel and

as an energy storage molecule, making it one of the keys to a clean energy future. This is expected to provide extreme flexibility to the power grid, as hydrogen can store renewable energy whenever available and later can be utilizes on demand. The primary hurdle in utilizing renewable energy resources to their fullest potential is their intermittency and variability in their availability, which can be bridged smoothly with this carrier molecule. The hydrogen economy not only smooths the transition; but also provides great flexibility to power grid[4,17–19].

1.1.3.2. Environment and health benefits:

Hydrogen serves as the ultimate solution to the damages caused by the unrestricted exploitation of environmental resources via the carbonaceous economy for the past two centuries. Shift to hydrogen economy is expected to bring down emissions (GHGs, toxic gases, particulates) drastically, thereby promoting the envisioned net carbon zero/ carbon neutral future. Harvesting renewable energy is a one-on-one process in the hydrogen economy without any intermediacy or emissions, which can be directly converted to hydrogen with extreme purity. Hydrogen on direct combustion as well as during indirect combustion fuel cells, generate water (H_2O) without any by-product/unwanted emissions. Hydrogen can contribute immensely in hard-to-abate fields like aviation, shipping, iron and steel production, chemical manufacture, long-distance and long-haul road transport, and, especially in dense urban environments or off-grid, heat for buildings. It fits well within the target of sustainable development focused on carbon neutrality[4,5,17,33,36].

1.1.3.3. Energy security:

The available amount of energy dictates the growth and development of any society. The existence and development of each and every community solely depend on the carbonaceous fuel deposits/reserves, which have geological variations in their availability. The continued dependence on these energy reserves has caused a hierarchy and associated socio-economic crisis. Locally produced hydrogen from the available renewable resources is expected to provide energy sustenance and thereby lower the dependence on energy imports. The possible direct conversion of renewable energy to hydrogen is expected to provide an extra handle to off-grid applications. Thus, hydrogen economy is a yardstick for energy security[4,8,17,18,52].

1.1.4. The challenges in implementing hydrogen economy

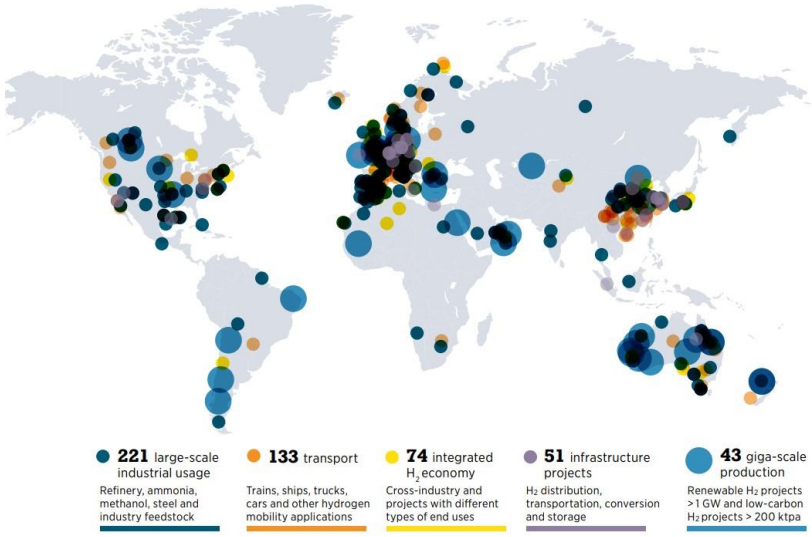

***Figure 1.1.2**: Clean hydrogen projects and investment as of November 2021*[4,59]

The profound importance of adapting the hydrogen economy has gained attention from around the globe[4,7,32–36,38,52,59,8,17,18,21,23,27,29,30]. The need for the immediate transition and its associated benefits have been realized by the majority of countries, which led to the introduction of various strategies and policies. A number of international organizations are in place for the same cause and to boost the pace (Figure 1.1.2). The combined efforts are reflected in the increased investments in clean hydrogen projects on an international level as shown in Figure 1.1.2: which marks the existing clean hydrogen projects/investments around the globe[4,59]. However, the key steps of the hydrogen economy such as production, storage/transport, and utilization require multiple device architectures comprising expensive electrodes, electrolytes and electrocatalysts that in turn add up enormously to the cost of implementation of hydrogen economy apart from posing immense technological challenges.

In summary, 200 years of dependence on the carbonaceous energy economy have already demonstrated its devastating negative impacts on the environment. The continued dependence on the same is expected cause irreversible damages and thereby pose threat to life on Earth. The proposed goals in 2015 as per the Paris agreement and the 17 SDG goals have left us with only around 25 years with respect to the left-out carbon budget. This calls for an immediate shift to an alternative green/clean sustainable energy

economy, and the hydrogen economy is expected to be the cornerstone of a sustainable future. Flexibility in the power grid, environmental and health benefits as well as energy security are the other major attractions.

1.2. Aim and scope of the thesis:

The assumption/consideration that all the national net zero pledges announced are pulled off on time is termed as the Announced Pledges Case (APC). As per APC statistics electric supply from renewable energy will be heightened by 2050 to 70% compared to 30% in 2020[2].

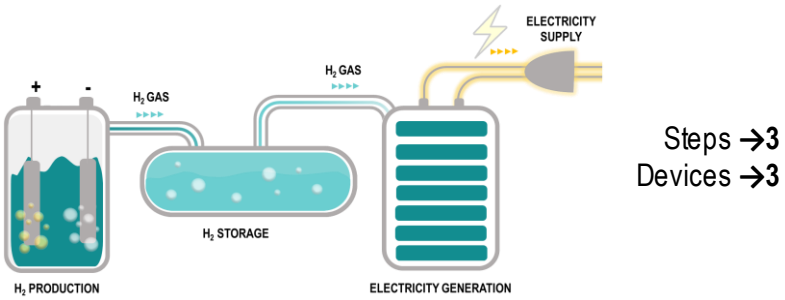

***Figure 1.2.1**: Schematic representation of three step/three device Hydrogen economy.*

This involves green hydrogen generation via water electrolysis utilizing renewable energy. This is followed by storage and transport of this generated hydrogen to the site of electricity generation. The minimum number of devices/setups for implementing hydrogen economy is three, associated with the production of hydrogen, storage and transport of hydrogen, and utilization of hydrogen. The involvement of these multiple devices for implementing hydrogen economy brings along technological and engineering challenges, along with serious cost implications. As per statistics, the production and consumption of hydrogen and hydrogen-based fuels is expected to shoot from nearly 80Mt in 2020 to nearly 530Mt in 2050[2] i.e., a surge nearly by 6.6 times. The inputs for such a huge infrastructure may not be economically sustainable in the long run, which can even cause the destabilization of the most robust financial system. However, given the fact that the quality of life on this planet depends up on the successful shifting from the carbonaceous economy to the hydrogen economy, it is desirable to encompass all the three key steps of hydrogen economy under an umbrella, for its robust implementation.

This thesis titled **'Design and Development of Rechargeable Proton Battery'** majorly involve attempts to amalgamate all the three aspects of hydrogen economy in a single electrochemical energy

device. The heart of this research work involves the screening, discerning, synthesizing, elucidating battery-relevant electrochemical parameters, mechanistic understanding, etc., of electrochemically active hydrogen storage materials and molecules and their integration into electrochemical energy devices, so as to successfully fabricate, a single energy device encompassing all the key steps of hydrogen economy. With this aim, this thesis is divided into four Chapters and the chapter-wise details are provided below:

Chapter 1: Introduction

It is a summarized account of the carbonaceous economy and its negative impacts on global climate change, anthropogenic pollution, impacts on the quality of life etc. Special emphasis is given to Paris Agreement on climate change by United Nations in 2015 that advocates sustainable development goals by providing directions to shift to an alternative carbon neutral energy economy. In these contexts, hydrogen economy with its three major steps is introduced as the silver bullet. Its importance in achieving a carbon zero future goal and energy security is highlighted along with the challenges that derail its implementation.

Chapter 2: Materials and Methods

This chapter is a concise description of the materials, procedures, and equipment used, including the details on the experimental setup, data collection and data analysis of various physio-chemical methods.

Chapter 3: An Electrically Rechargeable Hydrogen Battery

In this Chapter, energy stored in hydrogen molecules were directly utilized to generate electricity via coupling it with a hydrogen storing organic molecule possessing positive redox potential with respect to hydrogen redox. During the battery discharge, oxidation of the hydrogen molecule at the negative electrode is accompanied by the proton storage in the organic quinone-based molecule at the positive electrode. The electrochemical reversibility of the organic molecule with respect to its hydrogenation/dehydrogenation facilitate the battery to be recharged by applying an external potential. This device encompasses two aspects of hydrogen economy such as hydrogen storage as well its utilization in a single energy device.

Chapter 4: An Air Chargeable Hydrogen Battery

This Chapter explores the charging the developed hydrogen battery in the event of an electric power unavailability, which is important in isolated/rural areas and for military operation in challenging geography. In these lines, the possibility of air charging was explored because the electrochemical

hydrogenation/dehydrogenation of the organic molecule lies in between hydrogen redox and oxygen redox, with the organic molecule demonstrating a negative redox potential with respect to oxygen. The presence of oxygen not only activates the dehydrogenation of the organic quinone-based molecules leading to the battery charge, but it also reverses the electron flow, that can indeed power an external load. Therefore, by supplying oxygen, recharging of the battery is actuated along with the generation of electricity. This device again combined two key aspects of the hydrogen economy such as utilization and storage of hydrogen in a single device.

Chapter 5: An all Solid State Proton Battery

A range of safety challenges are involved in the direct utilization of gaseous hydrogen. In order address these, hydrogen storage materials with its electrochemical proton insertion/deinsertion potentials as close as gaseous hydrogen were explored. Tungsten trioxide WO_3 was opted as the metal oxide for this purpose because of its proton assisted redox chemistry occurring at a potential as close as gaseous hydrogen with a high proton intake capacity and remarkable insertion/deinsertion cyclic stability. Coupling WO_3 with a hydrogen storing organic molecule whose proton assisted redox chemistry happening at a relative positive potential allowed the fabrication of an solid-state battery by successfully combining the storage and utilization of hydrogen in a single device.

Chapter 6: A Rechargeable Atmospheric Water Battery

This Chapter major discusses attempts to include all the aspects of hydrogen economy in a single device and to achieve this target an extra handle of hydrogen production is introduced in the hydrogen battery system. To meet the primary requirement of hydrogen generation via water electrolysis, we adopt a unique pathway of utilizing the atmospheric water, thereby negating the necessity of ultrapure water and water transport infrastructure. The uptake of atmospheric water into the battery was facilitated by integrating a hydrophilic Graphene Oxide (GO) membrane that can simultaneously shuttle protons with a water uptake capability that is nearly 4 times higher than a commercial Nafion 117 membrane. The electrodes were chosen such that they are active towards water splitting on battery charge and the reversal on battery discharge. The negative half-cell electrocatalyst was chosen in such a way that it not only produces hydrogen but also stores it. It has also demonstrated the capability to release hydrogen at the time of discharge leading to electric power generation. Therefore, this device by harvesting atmospheric water connected all the key aspects of the hydrogen economy in a single energy device.

Chapter 7: Summary and Future Outlook

This chapter provides a brief summary of the work reported in this thesis, Figure 1.2.2, with an emphasis on the future outlook.

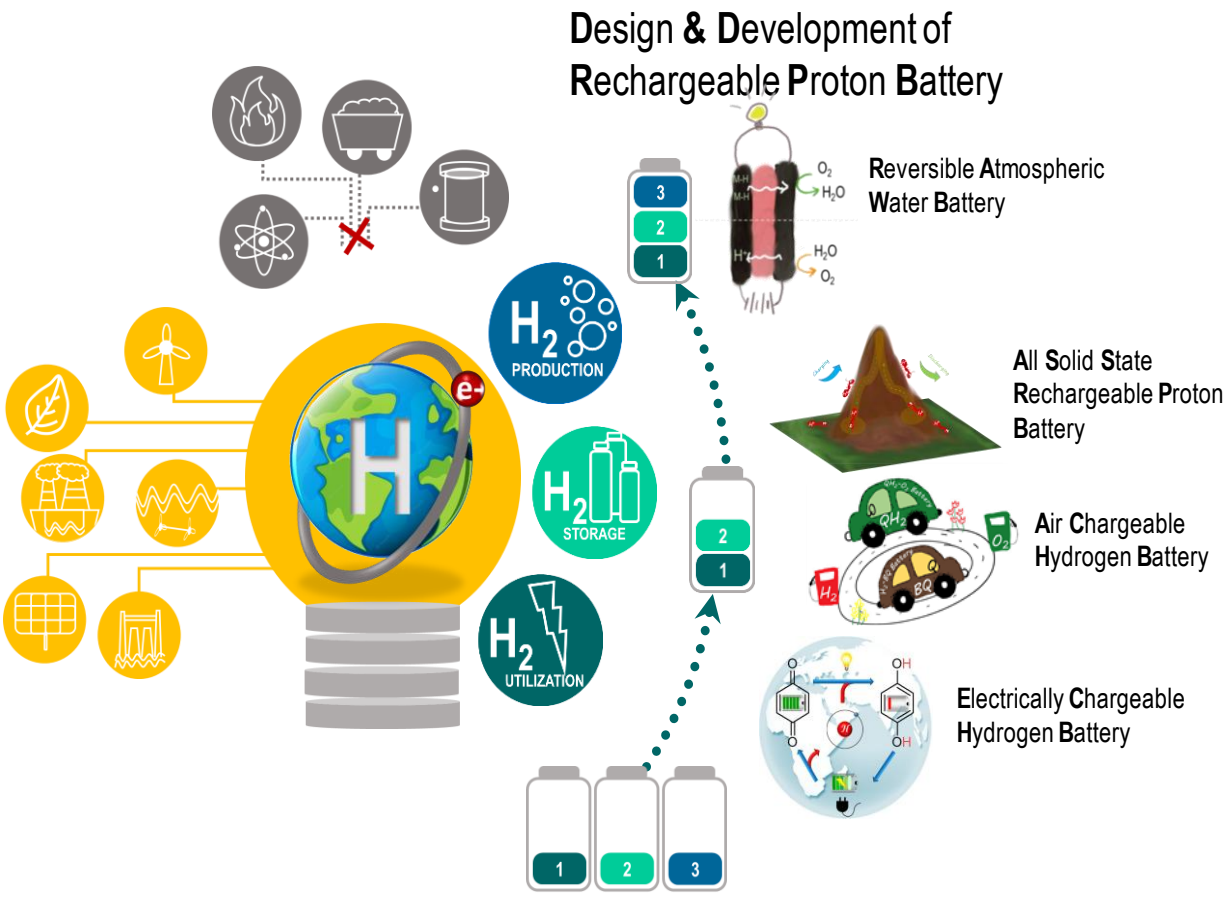

Figure 1.2.2: *Schematics summarizing the work outlined in the thesis.*

References:

1 M. K. Hubbert, *Science (80-.)*., 1949, **109**, 103–109.

2 A. J. Sangster, *Int. J. Sustain. Green Energy*, 2014, **3**, 115.

3 U. D. of Energy, *International Energy Outlook*, 2010, **0484**.

4 International Energy Agency, *Net Zero by 2050: A Roadmap for the Global Energy Sector*, 2021.

5 UNEP, *Climate Change 2023: Synthesis Report | UNEP - UN Environment Programme*, 2023.

6 UNEP, *Emissions Gap Report 2023: Broken Record – Temperatures hit new highs, yet world fails to cut emissions (again)*, United Nations Environment Programme, 2023, vol. 164.

7 UN-Energy, *energy compacts – annual progress report*, .

8 R. Garaffa, in *Dictionary of Ecological Economics: Terms for the New Millennium*, Edward Elgar Publishing, 2023, pp. 185–186.

9 Energy Production and Consumption - Our World in Data, https://ourworldindata.org/energy-production-consumption#total-energy-consumption, (accessed 12 November 2023).

10 *Infographic : The Global Carbon Budget*, 2014.

11 D. Welsby, J. Price, S. Pye and P. Ekins, *Nature*, 2021, **597**, 230–234.

12 UNFCC, *The Paris Agreement*, 2015.

13 J. Rogelj, M. Schaeffer, P. Friedlingstein, N. P. Gillett, D. P. van Vuuren, K. Riahi, M. Allen and R. Knutti, *Nat. Clim. Chang.*, 2016, **6**, 245–252.

14 Sustainable Development Goals launch in 2016, https://www.un.org/sustainabledevelopment/blog/2015/12/sustainable-development-goals-kick-off-with-start-of-new-year/, (accessed 12 November 2023).

15 United Nations, *Transforming our World: The 2030 Agenda for Sustainable Development*, 2015.

16 G. Schmidt-Traub, C. Kroll, K. Teksoz, D. Durand-Delacre and J. D. Sachs, *Nat. Geosci. 2017 108*, 2017, **10**, 547–555.

17 D. of E. and S. A. United Nations, *ENERGY ' S INTERLINKAGES SDGs*, 2022.

18 UNSD & IEA, *Tracking SDG7: The Energy Progress Report 2023*, 2023.

19 J. D. Sachs, G. Schmidt-Traub, M. Mazzucato, D. Messner, N. Nakicenovic and J. Rockström, *Nat. Sustain. 2019 29*, 2019, **2**, 805–814.

20 F. Biermann, T. Hickmann, C. A. Sénit, M. Beisheim, S. Bernstein, P. Chasek, L. Grob, R. E. Kim, L. J. Kotzé, M. Nilsson, A. Ordóñez Llanos, C. Okereke, P. Pradhan, R. Raven, Y. Sun, M. J. Vijge, D.

van Vuuren and B. Wicke, *Nat. Sustain. 2022 59*, 2022, **5**, 795–800.

21 C. Acar and I. Dincer, *Int. J. Hydrogen Energy*, 2022, **47**, 40118–40137.

22 A. Rehman, M. M. Alam, I. Ozturk, R. Alvarado, M. Murshed, C. Işık and H. Ma, *Environ. Sci. Pollut. Res.*, 2023, **30**, 9699–9712.

23 The Hydrogen Economy: Creating the fuel of the future | Trackinsight, https://www.trackinsight.com/fr/etf-news/hydrogen-economy-creating-fuel-future, (accessed 12 November 2023).

24 N. Brandon, F. Armstrong, S. H. Chan, B. David, R. Dittmeyer, J. Durant, A. Guwy, K. Hirose, A. Kucernak, I. Metcalf, M. Muskett, M. Newborough and J. Patterson, *Clim. Chang. Sci. Solut. Hydrog. Ammon.*, 2021, **4**, 1–13.

25 N. Armaroli and V. Balzani, *ChemSusChem*, 2011, **4**, 21–36.

26 F. Dawood, M. Anda and G. M. Shafiullah, *Int. J. Hydrogen Energy*, 2020, **45**, 3847–3869.

27 A. Roy and S. Pramanik, *Int. J. Hydrogen Energy*, 2023, **49**, 792–821.

28 P. Muthukumar, A. Kumar, M. Afzal, S. Bhogilla, P. Sharma, A. Parida, S. Jana, E. A. Kumar, R. K. Pai and I. P. Jain, *Int. J. Hydrogen Energy*, 2023, **48**, 33223–33259.

29 M. Ball and M. Wietschel, *Int. J. Hydrogen Energy*, 2009, **34**, 615–627.

30 S. Bourne, *Fuel Cells Bull.*, 2012, **2012**, 12–15.

31 D. Pashchenko, *Renew. Sustain. Energy Rev.*, 2023, **173**, 113117.

32 CMS Law - Legal Services, *Facing the Future of Hydrogen: An International Guide*, 2021, vol. 1.

33 P. P. Edwards, V. L. Kuznetsov and W. I. F. David, *Philos. Trans. R. Soc. A Math. Phys. Eng. Sci.*, 2007, **365**, 1043–1056.

34 *THE HYDROGEN ECONOMY A non-technical review*, UNEP.

35 U. D. of E. H. P. Energy, *Hydrogen & Our Energy Future*, .

36 Ministry of Foreign Affairs of Denmark, *Green Hydrogen Compact Catalogue*, 2021.

37 R. W. Coughlin and M. Farooque, *Nature*, 1979, **279**, 301–303.

38 *UK hydrogen strategy*, 2021, **85**.

39 Q. Cheng, R. Zhang, Z. Shi and J. Lin, *Int. J. Light. Mater. Manuf.*, , DOI:10.1016/j.ijlmm.2023.08.002.

40 H. Barthélémy, *Int. J. Hydrogen Energy*, 2012, **37**, 17364–17372.

41 Y. Kojima, H. Miyaoka and T. Ichikawa, in *New and Future Developments in Catalysis: Batteries, Hydrogen Storage and Fuel Cells*, Elsevier B.V., 2013, pp. 99–136.

42 N. Klopčič, I. Grimmer, F. Winkler, M. Sartory and A. Trattner, *J. Energy Storage*, 2023, 72.

43 P. Chen, Z. Xiong, J. Luo, J. Lin and K. L. Tan, *Nature*, 2002, **420**, 302–304.

44 T. K. P. Myunghyun Paik Suh, Hye Jeong Park, *Chem. Rev.*, 2012, **112**, 782–835.

45 T. He, P. Pachfule, H. Wu, Q. Xu and P. Chen, *Nat. Rev. Mater.*, 2016, **1**, 16059.

46 P. Chen, X. Wu, J. Lin and K. L. Tan, *Science (80-.).*, 1999, **285**, 91–93.

47 R. Ma, Y. Bando, T. Sato and K. Kurashima, *Chem. Mater.*, 2001, **13**, 2965–2971.

48 In *The IUPAC Compendium of Chemical Terminology*, International Union of Pure and Applied Chemistry (IUPAC), Research Triangle Park, NC, 2014.

49 In *The IUPAC Compendium of Chemical Terminology*, International Union of Pure and Applied Chemistry (IUPAC), Research Triangle Park, NC, 2014.

50 A. Lys, J. O. Fadonougbo, M. Faisal, J.-Y. Suh, Y.-S. Lee, J.-H. Shim, J. Park and Y. W. Cho, *Hydrogen*, 2020, **1**, 38–63.

51 *Mater. Res. Soc. Symp. Proc.*, 2010, 1216.

52 Fuel Cell and Hydrogen Energy Association, 2020, 1–20.

53 Ministry of New and Renewable Energy and Government of India, 2023, 1–70..

54 Z. Kang, Q. Liao, Z. Zhang and Y. Zhang, *Nat. Mater.*, 2022, **21**, 1094–1098.

55 J. Hwang, K. Maharjan and H. Cho, *Int. J. Hydrogen Energy*, 2023, **48**, 28629–28648.

56 H. Kobayashi, M. Yamauchi, R. Ikeda, T. Yamamoto, S. Matsumura and H. Kitagawa, *Chem. Sci.*, 2018, **9**, 5536–5540.

57 Hydrogen Fuel Cell Engines and Related Technologies, *Hydrog. Fuel Cell Engines*, 2001, 41.

58 C. Rivkin, R. Burgess and W. Buttner, *Nrel*, 2015, 67.

59 IRENA, *Geopolitics of the energy transformation: the hydrogen factor.*, 2022.

Chapter 2:

Materials and Methods

2.1: Materials used:

1,4-Benzoquinone $C_6H_4O_2$ (Alfa Aesar), 1,4-Hydroquinone $C_6H_4(OH)_2$ (SDFCL), Quinhydrone $C_{12}H_{10}O_4$ (Alfa Aesar), Citric acid $C_6H_8O_7$ (Alfa Aesar), Trisodium citrate $C_6H_5O_7Na_3$ (SDFCL), Monopotassium phosphate KH_2PO_4 (Alfa Aesar), Dipotassium phosphate K_2HPO_4 (Alfa Aesar), Borax $Na_2B_4O_7$•$10H_2O$ (Rankem), Potassium permanganate ($KMnO_4$) (Rankem), Sodium hydroxide NaOH (SDFCL), Carbon powder (Super P, Vulcan carbon, Graphite powder) (Alfa Aesar), Sulphuric acid (H_2SO_4) (Rankem), Phosphoric acid (H_3PO_4)(SDFCL), Hydrochloric acid (HCl) (Rankem), Isopropyl alcohol(IPA) (C_3H_8O) (Rankem), Hydrogen peroxide (H_2O_2) (Rankem), Nano particles of various transition metal oxides such Cobalt oxide (CoO_x), Manganese oxide (MnO_x), Vanadium oxide (VO_x), Molebdenum oxide (MoO_x), Titanium oxide (TiO_x) and Tungsten trioxide (WO_3), as was procure from American elements, Sigma Aldrich, and Alfa Aesar, India. Platinum (40 wt% on carbon powder) was obtained from Johnson Matthey, India. Palladium Black (99.9%) (Alfa Aesar), Platinum Black (Thermo Fisher), Iridium (IV) Oxide- premion (Alfa Aesar), Ruthenium (IV) oxide anhydrous-premion (Alfa Aesar), Palladium nitrate hydrate ($Pd(NO_2).H_2O$) (Thermo Fisher) were used as received. Nafion® $C_7HF_{13}O_5S$•C_2F_4 (5 wt % in lower aliphatic alcohols and water) (Aldrich), Nafion® membrane 117 and 212 was obtained from fuel cell store, USA.

2.2: Instrumentation:

VMP-300 Electrochemical Work Station (BioLogic), PARSTAT MC (Ametek) for electrochemical investigations. SEC2000-UV/Vis Spectrometer System, Hiden HPR-40 DEMS (Mass spectrometry), Nicolet iS50 Fourier Transform Infrared spectrophotometer with infrared microscope, XploRA™ PLUS Raman Spectrometer - Confocal Raman Microscope, Bruker D8-Advance (XRD), Electrochemical Quartz Crystal Microbalance 922A (E-QCM) (Ametek) were used for In-situ-electrochemical characterization. UV-3600 Plus UV-VIS-NIR spectrophotometer, ATR-FTIR (Bruker Alpha FTIR Spectrometer System), and LAB-RAM HR 800, Bruker D8-Advance (XRD), IGASORP (DVS analyzer) for ex-situ- characterization.

2.3: Experimental details:

2.3.1: Cyclic voltammogram

Cyclic voltammograms were collected in nitrogen atmosphere at different scan rates in three-electrode system with a glassy carbon (GC) as the working electrode, Ag/AgCl (3 M KCl) as the reference electrode, and platinum wire as the counter electrode in 10 mM benzoquinone dissolved in 0.5 M H_2SO_4. pH-

dependent behavior of benzoquinone was studied by cyclic voltammogram of 10 mM of benzoquinone in different pH buffer solutions like citrate buffer (pH = 4, 5), phosphate buffer (pH = 6, 7), and borate buffer (pH = 9, 10) in nitrogen atmosphere. Single electrode potentials were measured in nitrogen atmosphere using a two-electrode system with GC as a working electrode and Ag/AgCl (3 M KCl) as a reference electrode in a solution of 5 mM benzoquinone (or 5 mM hydroquinone) in 0.5 M H_2SO_4.

Cyclic voltammograms of hydrogen redox reaction were collected in the solution of 0.5 M H_2SO_4 at hydrogen atmosphere at a scan rate of 5mVs in a three-electrode system with platinum as working electrode, Ag/AgCl (3 M KCl) as reference electrode, and platinum wire as counter electrode. Similarly, oxygen reduction was probed in oxygen saturated solution of 0.5 M H_2SO_4 at a scan rate of 5mVs in three-electrode system with platinum as the working electrode, Ag/AgCl (3 M KCl) as the reference electrode, and platinum wire as the counter electrode.

Cyclic voltammograms of oxides of various transition metals such as Co, Mn, V, Mo, Ti, W, Pd, Ir, and Ru were carried nitrogen atmosphere at different scan rates in three-electrode system with a (2mg of material dispersed in 200µl of IPA and 5W% Nafion) 5µl of the ink drop casted on to glassy carbon (GC) as working electrode, Ag/AgCl (3 M KCl) as reference electrode, and platinum wire as counter electrode in 0.5 M H_2SO_4.

2.3.2: Diffusion coefficient

Chrono amperometry was collected in nitrogen atmosphere in three electrode system with a glassy carbon (GC) as the working electrode, Ag/AgCl (3 M KCl) as the reference electrode, and platinum wire as the counter electrode with a known amount of material dissolved in 0.5 M H_2SO_4. Further, diffusion coefficient in cm^2/s was calculated using the Cottrell Equation:[1]

$$i(t) = \frac{nFAD^{1/2}\mathrm{C}}{\pi^{1/2}t^{1/2}} \qquad \text{(eq 2.1)}$$

Where i - current, n - no of electrons, F - faradays constant (96485 C mol^{-1}), A - area of electrode (cm^2), D - diffusion coefficient ($cm^2\ s^{-1}$), C - concentration (mol cm^{-3}), t-time (s)

2.3.3: Electrochemical Active Surface Area:

2.3.3.1: Double layer method

The electrochemically active surface area (ECSA) by utilising the equation(ref)[1–4]

$$ECSA = \frac{C_{dl}}{C_s} \quad \text{(eq 2.2)}$$

Where C_s (in F/cm^2) is the specific capacitance of a perfectly flat electrode and C_{dl} (in F) is the electrochemical double layer capacitance of the material obtained in the non-Faradaic region. The electrochemical double layer capacitance of the WO3 obtained in the non-Faradaic region (at nearly 0.73 V vs RHE)

2.3.3.1: Surface-bulk oxidation method

The electrochemically active surface area (ECSA) utilizing monolayer to multilayer oxide formation. The charge corresponding to the inflation point Q_0 (in µC) is further divided by standard Q_s (eg: ~420 µC/cm^2 for palladium) to obtain ECSA (in cm^2).

$$ECSA = \frac{Q_0}{Q_s} \quad \text{(eq 2.3)}$$

2.3.4: The surface capacitive contribution VS. diffusion-controlled insertion process

To decouple the current contributions to its individual components following equation[4,5] is utilised.

$$i(\upsilon) = k_1\upsilon + k_2\,\upsilon^{1/2} \quad \text{(eq 2.4)}$$

Where υ - scan rate (V/s), i- current (A). The surface capacitive contribution has a direct relation to the scan rate (k_1υ) whereas the diffusion-controlled insertion process has a square root relation to the scan rate (k_2 $\upsilon^{1/2}$)

2.3.4: Hydrodynamic studies

Rotating ring disk electrode (RRDE) measurements were done in nitrogen purged solution of 1 mM hydroquinone in 0.5 M H_2SO_4 at a scan rate of 10 mV/s in a three electrode system with a platinum disk and a platinum ring (Pt-Pt) electrode as working electrode, Ag/AgCl (3 M KCl) as reference electrode and platinum wire as counter at different RPM values (100, 400, 900, 1600, 3600). Rotating disk electrode (RDE) studies were done with solutions of hydroquinone and benzoquinone as mentioned above. Analysis of the above data was done with the help of Koutecky-levich equation[1] to find the no of electrons, transfer coefficient, and rate of reaction. [1,6]

$$\frac{1}{i} = \frac{1}{i_k} + \frac{1}{i_L} \quad \text{(eq 2.5)}$$

$$\frac{1}{i} = \frac{1}{i_k} + \frac{\omega^{-1/2}}{(0.620nFAD^{2/3}\upsilon^{-1/6}C)} \quad \text{(eq 2.6)}$$

Where i_L - limiting current, n - no of electrons, F - faradays constant (96485 C mol^{-1}), A - area of electrode (cm^2), D - diffusion coefficient (cm^2 s^{-1}), υ - kinematic viscosity (cm^2 s^{-1}), C - concentration (mol cm^{-3}),ω - rotation rate (rad s^{-1})

2.3.5: In-situ electrochemical techniques

2.3.5.1: In-situ UV-Vis spectroelectrochemistry

In-situ UV-Vis spectroelectrochemistry quinone-hydroquinone was collected with 1 mM hydroquinone in 0.5 M H_2SO_4 in three electrode system containing a platinum mesh electrode as working electrode, Ag/AgCl (3 M KCl) as reference electrode, and platinum wire as counter electrode. Similarly, tungsten trioxide WO_3 coated over FTO-glass as the working electrode, Ag/AgCl (3 M KCl) as the reference electrode, and platinum wire as the counter electrode were dipped in 0.5 M H_2SO_4. The spectrum of starting material was taken as the background. The differential absorption (ΔA) was monitored at every interval of 1 second during oxidation as well as the reduction scan. A negative absorption peak in the differential spectra indicates depletion and a positive indicates accumulation.

$$\Delta A = A_b - A_t \quad \text{(eq 2.7)}$$

Where A_t is the Absorbance at any time in seconds and A_b the Absorbance at OCV

2.3.5.2: In-situ Electrochemical Quartz Crystal Microbalance (E-QCM)

The EQCM studies of tungsten trioxide (WO_3) were carried out with gold coated 8MHz QCM electrode coated with a thin film of WO_3 (8µl from 2mg in 200 µl ink) mounted on a dip cell, which was further dipped in 0.5 M H_2SO_4 simultaneously connected to potentiostat as working electrode and to the microbalance. Experiments were carried out maintaining three-electrode system Ag/AgCl (3 M KCl) as the reference electrode, and platinum wire as the counter electrode, the whole system was kept inside the Faraday cage to minimize the disturbance. The change in frequency was continuously monitored along with cycling at the scan rate of 1 mV/s. Utilizing equation [1]

$$\Delta f = -\frac{n.\Delta m}{C} \quad \text{(eq 2.8)}$$

Where Δf – change in frequency (Hz), Δm- change in mass (g), n – no: of harmonics and the constant, C

which is the so-called the mass sensitivity constant, is related to the properties of quartz.

2.3.5.3: In-situ FTIR spectro-electrochemistry

In-situ FTIR spectro-electrochemistry investigation of tungsten trioxide (WO_3) was carried out in the specialized EL-Cell in a three-electrode configuration where a thin film of WO_3 on carbon as the WE (1 cm dia) was selectively exposed to the IR beam and the reflecting beam from the electrode was recorded. Platinum as the CE, solid-state Ag/AgCl (Sat. KCl) as RE, with a separator soaked in 0.5 M H_2SO_4 as electrolyte (Figure 2.1). The potential was swept at a scan rate of 1mV/s and the FTIR spectrum of the sample was collected at every interval of 100mV. For the analysis, the relative reflectance at each of the potentials was further calculated using the following equation:[7]

$$\frac{\Delta R}{R} = \frac{R_x - R_b}{R_b} \qquad \text{(eq 2.9)}$$

Where R_x= Reflectance at x V and R_b= Reflectance at base line (at 1 V for WO_3)

***Figure 2.1**: Photograph of the in-situ-electrochemical FTIR setup with WO_3 as the working electrode (WE).*

2.3.5.4: In-situ Electrochemical Mass Spectrometry

The electrode chamber to be analyzed is directly connected to the differential mass spectra analyzer. Mostly an inert gas such as nitrogen is flown through it which acts as carrier gas. The outlet of the electrode chamber was directly connected to the instrument, collected stabilized signals at OCV, and then the changes in partial pressures were monitored during the course of battery charge and discharge.

2.3.5.5: In-situ Electrochemical XRD analysis

In-situ Electrochemical XRD analysis of the battery anode Palladium black on carbon sheet (1 cm dia) was carried out in a homemade specialized cell in two electrode configuration where the anode was selectively exposed to the X-rays through a Kapton window. XRD patterns of the anode were obtained in the order: at OCV, 100% charged and then 100% discharged state via application of potential bias.

2.3.5.6: In-situ RAMAN spectro-electrochemistry

In-situ RAMAN spectro-electrochemistry of the battery anode (tungsten trioxide (WO_3)) was carried out in the specialized EL-Cell in two electrode configuration where the anode was exposed to the Laser beam (Figure 2.2). Tungsten trioxide (WO_3) on Torey carbon as anode (WE) (1 cm dia), quinone/ carbon composite on Torey as cathode (CE) (1 cm dia) separated by pre-treated Nafion 212 membrane. A continuous scan was employed at regular intervals while the battery was charged and discharged. The absolute spectra obtained were analyzed.

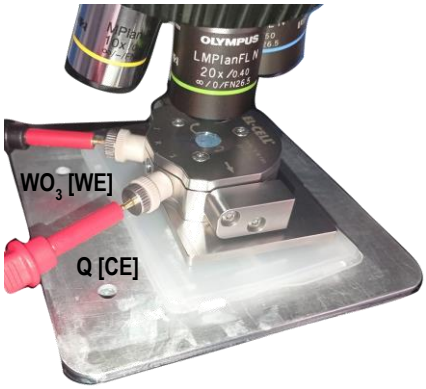

Figure 2.2*: Photograph of the in-situ-electrochemical Raman setup of the battery with WO_3 as the working electrode (WE), quinone as counter electrode (CE) with WE exposed to the lazer beam.*

2.3.6: Galvanostatic intermittent titration technique (GITT)

Galvanostatic intermittent titration technique (GITT) analysis with quinone electrode was performed as follows. Electrodes were made by coating the ink containing quinone powder, super P powder, and 10 wt % Nafion in isopropyl alcohol (IPA) on a Toray carbon sheet (2x2 cm^2 dimension). Pt@C electrode was used for hydrogen fuel oxidation/hydrogen evolution reaction and quinone composite electrode was used as the cathode electrode. Pt loading was ~0.5 mg/cm^2 and quinone loading was ~7 mg/cm^2. The anode and cathode were separated by a pre-treated Nafion 212 membrane. The cathode was always kept under nitrogen (N_2) atmosphere to avoid contact with any other gas. The anodic compartment was filled with H_2 and discharge was done for 5 minutes at 250 µA current followed by one hour of relaxation time and the process was repeated for several hours. The diffusion coefficient of H^+-ion in the quinone composite electrode was found using the equation[8],

$$D = \frac{4}{\pi\tau}\left(\frac{n_m V_m}{S}\right)^2 \left(\frac{\Delta E_s}{\Delta E_t}\right)^2 \quad \text{(eq 2.10)}$$

Where τ- duration of current pulse(s), n_m - number of moles (mol), S - electrode/electrolyte contact area (cm^2), V_m - molar volume of the electrode ($cm^3\ mol^{-1}$), ΔE_s - steady-state voltage change, due to the current pulse, ΔE_t - voltage change during the constant current pulse, eliminating the iR drop.

2.3.7: Battery Fabrication:

2.3.7.1: An Electrically Rechargeable Hydrogen Battery & An Air Chargeable Hydrogen Battery

For polarization and charge-discharge data collection, Pt@C and quinone electrodes were made as follows. Pt@C electrode was made by sonicating a mixture of 40 wt% Pt@C powder and 10 wt% Nafion (in IPA) for 30 minutes. The slurry was coated over 2x2 cm^2 Toray carbon paper. A carbon-coated Toray carbon paper (2x2 cm^2) was used as the cathodic current collector. Pre-treated Nafion 212 membrane was sandwiched between Pt@C and carbon electrodes to prepare membrane electrode assembly (MEA) (consisting of gas diffusion layer (GDL), Pt@C layer, Nafion membrane, quinone layer, and gas diffusion layer). MEA was then sandwiched between graphite plates with parallel flow fields. This was further sandwiched between current collector plates (Figure 2.3). The volume of H_2 in the anode chamber was 40 mL. quinone molecules were dissolved in N_2-saturated 0.5 M H_2SO_4 (125 mg/20 ml) and it was circulated continuously through the cathode chamber using a peristaltic pump. For characterization of the cathode during extended cyclability, it was made as described for GITT.

Figure 2.3*: Photograph of the cell setup utilized for fabrication of the electrically rechargeable hydrogen battery and the air chargeable hydrogen battery*

2.3.7.2: An all solid state proton battery

For all solid-state proton battery, electrodes were made by coating the ink containing tungsten trioxide, super P powder, and 10 wt % Nafion in isopropyl alcohol (IPA) on a Toray carbon sheet ((1 cm dia) for anode and quinone as mentioned in section 2.3.6. (1 cm dia). Pre-treated Nafion 212 membrane was sandwiched between electrodes to prepare membrane electrode assembly (MEA) (consisting of gas diffusion layer (GDL), WO_3 layer, Nafion membrane, quinone layer, and gas diffusion layer). MEA was pressed, sealed and assembled in a split cell (Figure 2.4).

Figure 2.4*: Photograph of the split cell setup utilized for the all solid state proton battery fabrication*

2.3.7.3: A Rechargeable Atmospheric Water Battery

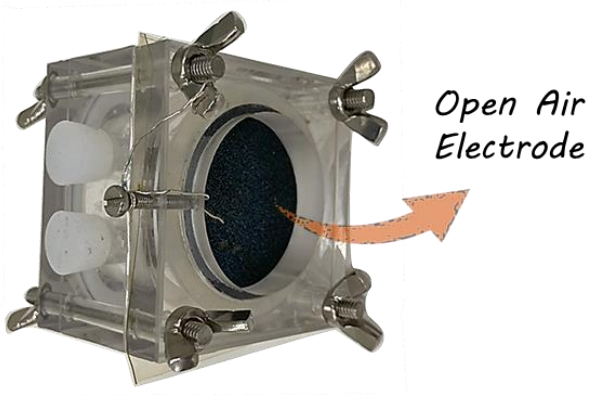

Figure 2.5*: Photograph of the cell setup utilized for the rechargeable atmospheric water battery fabrication with electrode 1 as air breathing electrode.*

Electrodes were prepared via spray coating the ink made in IPA on a 4*4 sheet electrode material of choice. For electrode 1, Palladium black and 20% palladium@Carbon along with 20% wt% Nafion (in IPA)

were sonicated for 30 minutes, then coated over a carbon electrode. The electrode 2 was prepared from ink containing Iridium oxide, Ruthenium oxide, and platinum black in a particular ratio along with 20% wt% Nafion (in IPA) where sonicated for 30 minutes, then coated over titanium mesh to provide porosity for the atmospheric air to pass through. Once spray coated the electrodes were made with a diameter of 1 cm and further applied 1 newton pressure for 10 minutes. Further MEA was prepared by sandwiching the membrane of choice (GO/ Nafion) with the prepared electrodes (Figure 2.5).

2.3.8: Cross over studies

Cross-over studies were done in a 2 compartment diffusion cell. Compartment 1 was filled with 0.5 M H_2SO_4 and compartment 2 was filled with 0.5 M H_2SO_4 solution containing 6.25 mg/ml of benzoquinone. Cross-over of quinone to compartment 1 from compartment 2 was investigated by a time-dependent cyclic voltammogram with a Pt electrode as the working electrode, Pt foil as the counter electrode, and Ag/AgCl (3.5 M KCl) as the reference electrode.

2.3.9: Impedance spectroscopy:

Impedance spectroscopy of WO_3 was carried out three-electrode setup, with 5µl WO_3 of the ink drop casted (as mentioned above) on to glassy carbon (GC) as working electrode, Ag/AgCl (3 M KCl) as reference electrode, and platinum wire as counter electrode in 0.5 M H_2SO_4, by applying a potential of -160 mV vs. Ag/AgCl (3 M KCl). Impedance spectroscopy analysis of the electrolytic resistance GO membrane as well as Nafion membrane was carried in two electrode battery fabricated with respective membranes and analyzed at operation voltage ranging from 1.6 V to 2 V.

2.3.10: Dynamic vapor sorption (DVS):

This is a gravimetric analysis technique that measures how quickly and how much of a solvent is absorbed by a sample such as a dry powder absorbing water. The relative humidity% (RH%) ranging from 1(dry) to 95% (wet) can be varied in the sample chamber with simultaneous measurement of mass change. Mostly two parameters are utilized to monitor the performance metrics, such as water uptake percentage (WU%) which is the amount of water uptake with respect to the mass of the membrane (eq.2.11) and hydration number (λ) (eq 2.12.) which is the number of water molecules a functionality can hold [8–10].

1: Water Uptake (WU) percentage : $\frac{W_{\text{equllibrium}} - W_{dry}}{W_{dry}} * 100\%$ (eq.2.11)

2: Hydration Number (λ): $\frac{W_{H_2O}/_{18.015}}{IEC*W_{dry}}$ (eq.2.12)

Where W_{dry} : Dry mass of membrane/ sample in g, W_{H2O}: Measured weight of water in g (water uptake: $W_{\text{equllibrium}} - W_{dry}$), IEC: ion exchange capacity (mequiv/g)

2.4: Material synthesis

2.4.1: Synthesis of graphene oxide

Graphene oxide (GO) was synthesized by improved Hummer's method[11,12]. 3.0 g of graphite flakes were taken in a round bottomed flask containing acid mixture of 320 mL of H_2SO_4 and 80 mL of H_3PO_4 (4:1). This was stirred well to obtain homogenous reaction mixture. To this mixture 18.0 g of potassium permanganate was added slowly with constant stirring. The stirring was continued for 3 days for the completion of the reaction. 15 mL of H_2O_2 was added drop wise to this mixture until the colour changed from pink to golden yellow colour and the reaction mixture was stirred for another 1 h. Finally, the product was collected by centrifugation and washed with 1 M HCl solution to remove the inorganic impurities which was followed by water wash. The dispersed graphene oxide in water was drop casted and dried on glass slides to obtain thin films of GO

References:

1 Allen J. Bard and Larry R. Faulkner, *Electrochemical methods : fundamentals and applications*, John Wiley & Sons, Inc., Hoboken, NJ, 2001, Second edition., 2001.

2 C. C. L. McCrory, S. Jung, J. C. Peters and T. F. Jaramillo, *J. Am. Chem. Soc.*, 2013, **135**, 16977–16987.

3 T. Priamushko, R. Guillet-Nicolas, M. Yu, M. Doyle, C. Weidenthaler, H. Tuÿsüz and F. Kleitz, *ACS Appl. Energy Mater.*, 2020, **3**, 5597–5609.

4 J. Liu, J. Wang, C. Xu, H. Jiang, C. Li, L. Zhang, J. Lin and Z. X. Shen, *Adv. Sci.*, 2018, **5**, 1700322

5 K. Sambath Kumar, ab Nitin Choudhary, D. Pandey, ab Yi Ding, ab Luis Hurtado, H.-S. Chung, L. Tetard, bd Yeonwoong Jung abe and J. Thomas, , *J. Mater. Chem. A*, 2020, **8**, 12699

6 R. Zhou, Y. Zheng, M. Jaroniec and S.-Z. Qiao, *ACS Catal.*, 2016, **6**, 4720–4728.

7 C. Kratz, A. Furchner, G. Sun, J. Rappich and K. Hinrichs, *J. Phys. Condens. Matter*, 2020, **32**,

393002

8 Y. Zheng, U. Ash, R. P. Pandey, A. G. Ozioko, J. Ponce-González, M. Handl, T. Weissbach, J. R. Varcoe, S. Holdcroft, M. W. Liberatore, R. Hiesgen and D. R. Dekel, *Macromolecules*, 2018, **51**, 3264–3278.

9 R. Lin, J. Liu, Y. Nan, D. W. Depaoli and L. L. Tavlarides, *Ind. Eng. Chem. Res.*, 2014, **53**, 16015–16024.

10 T. Maneerung, J. Liew, Y. Dai, S. Kawi, C. Chong and C. H. Wang, *Bioresour. Technol.*, 2016, **200**, 350–359.

11 D. C. Marcano, D. V. Kosynkin, J. M. Berlin, A. Sinitskii, Z. Sun, A. Slesarev, L. B. Alemany, W. Lu and J. M. Tour, *ACS Nano*, 2010, **4**, 4806–4814.

12 P. Xavier, K. Sharma, K. Elayaraja, K. S. Vasu, A. K. Sood and S. Bose, *RSC Adv.*, 2014, **4**, 12376.

Chapter 3:

An Electrically Rechargeable Hydrogen Battery

Abstract: This chapter articulates an electrically rechargeable hydrogen battery via combining the two key steps of hydrogen economy in a single device. It utilizes proton-coupled electron transfer in hydrogen storage molecules to unlock a rechargeable battery chemistry based on the cleanest chemical energy carrier molecule, hydrogen. Electrochemical, spectroscopic, and spectroelectrochemical analyses evidence the participation of protons during charge–discharge chemistry and extended cycling. In an era of anthropogenic global climate change and paramount pollution, a battery concept based on a virtually nonpolluting energy carrier molecule demonstrates distinct progress in the sustainable energy landscape.

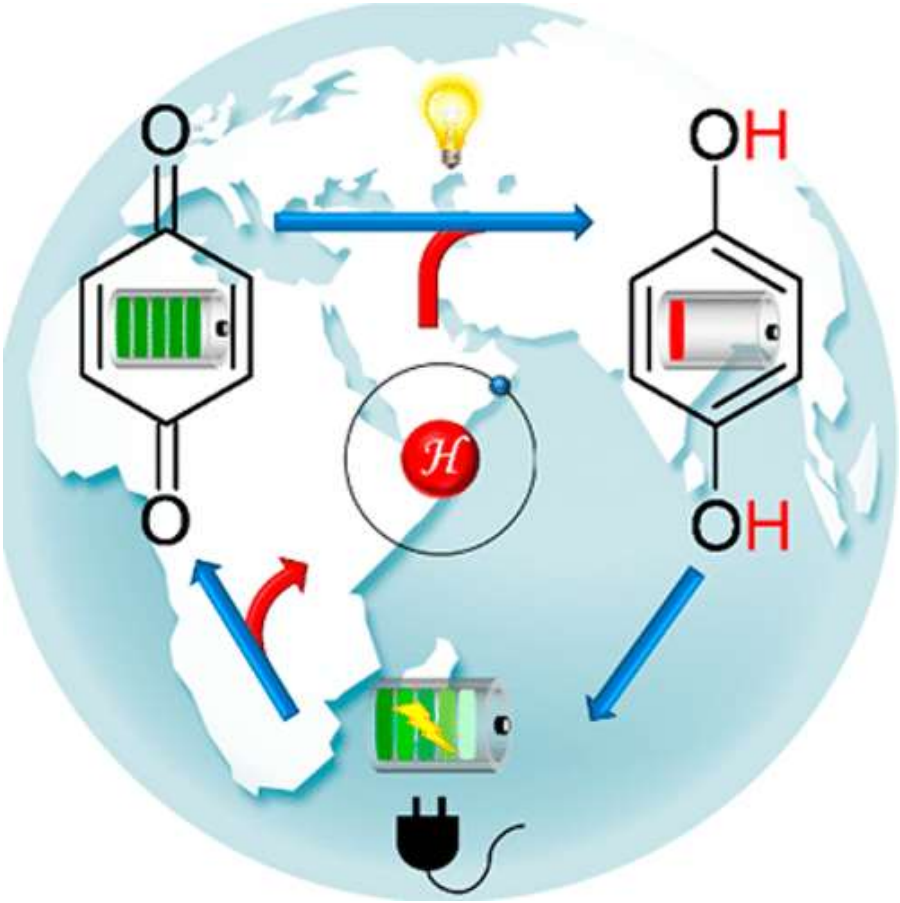

The chapter contains the data taken from my original published work: Neethu C. D. etal ***J. Phys. Chem. Lett.*** 2018, ***9***, 10, 2492–2497 Copyright American Chemical Society

Introduction:

Even though electricity production costs from renewable energy resources have significantly come down, large scale storage is limited by efficient energy storage modules [1–17]. Energy storage is largely dominated by metal ion batteries, and it is well-known that the state-of-the-art energy storage technologies have issues related to safety, cost, and environmental compatibility[1,9,11,14–21]. New inventions in flow batteries, organic electrodes, supercapacitors, and air batteries are right steps in making the electricity output much cleaner [2–5,7–10,14,15,21–25].

This device utilizes the hydrogen, one of the most abundant elements in the universe and the cleanest chemical energy carrier molecule [26–28], and electrochemically reversible hydrogenation/dehydrogenation of hydrogen storage organic molecules (Scheme 3.1). Various physicochemical techniques reveal the involvement of protons at both interfaces during the charge–discharge chemistry and extended cyclability.

Results and Discussion:

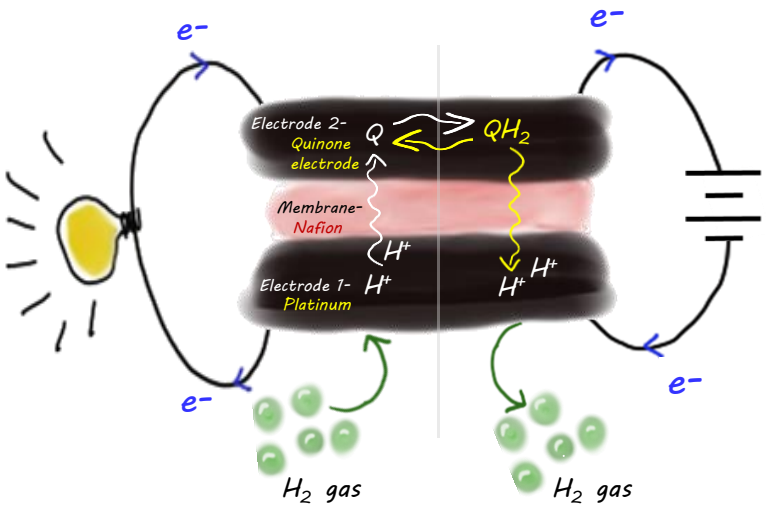

***Scheme 3.1**: Schematic Representation of a Rechargeable Hydrogen Battery Based on a Hydrogen-Storing Quinone/Hydroquinone Redox System.*

The proposed battery consists of Pt supported on carbon (Pt@C) at a loading of 0.5 mg/cm^2 as the anodic electrocatalyst for the ionization of H_2 molecules and bond formation between H^+ ions during discharge and charge chemistry, respectively. The positive electrode is based on the well-known hydrogen

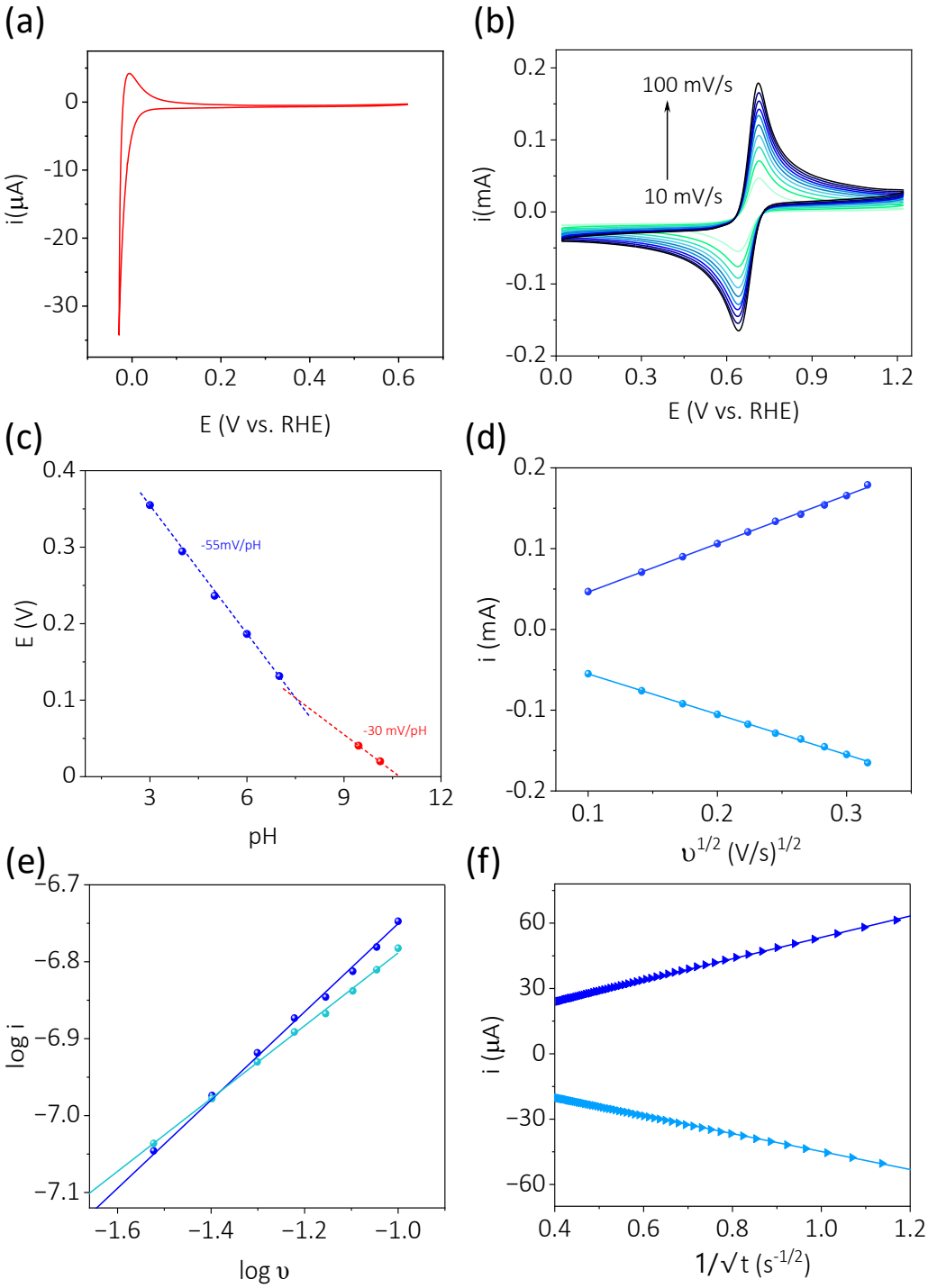

Figure 3.1 *(a) Cyclic voltammogram on a Pt electrode during hydrogen evolution reaction (HER) and hydrogen oxidation reaction (HOR) at 5 mV/s, (b) cyclic voltammograms of 10 mM benzoquinone in 0.5 M H_2SO_4 on a glassy carbon electrode at different scan rates. (c) pH vs. potential (Pourbiax diagram) plot for benzoquinone, (d) plot of peak current vs. square root of scan rate during the oxidation scan (navy blue trace) and reduction (light blue trace). (e) plot of log (i) vs. log (υ) during the oxidation scan (navy blue trace) and reduction (light blue trace). (f) Cottrel plots (current vs. reciprocal of square root of time) for hydroquinone (navy blue trace) and quinone (light blue trace) of 5 mM in 0.5 M H_2SO_4.*

storage molecule quinone based organic molecule (Q), and the two electrodes are separated by a H^+-ion conducting Nafion 212 membrane (Scheme 3.1).

We chose a Pt electrode as the negative electrode due to its well-known electrocatalytic ability in the hydrogen evolution reaction (HER) and hydrogen oxidation reaction (HOR) [29,30] (Figure 3.1a) and Q as the positive electrode because of its well-known proton-coupled electron transfer with electrochemically assisted formation and decomposition of hydroquinone (QH_2) from a cyclic voltammogram, (Figure 3.1b). For a fundamental electrochemistry investigation of the quinone redox reaction by cyclic voltammetry, a Pourbaix diagram, and chrono-amperometry, a solution of Q (1–10 mM) in 0.5 M H_2SO_4 was employed. The Pourbaix diagram for the redox transition of Q (Figure 3.1c) demonstrates shift in potential with increase of pH with a slope of ~55 mV/pH (pH~1-7), ~30 mV/pH (pH~8-11), confirming that electron transfer is accompanied by proton transfer [31–33]. The square root dependence of the peak current on the scan rate (Figure 3.1d) further indicates a diffusion-controlled process, which is further clear from the near 1/2 slope of the log (*i*) vs log (scan rate) plot (Figure 3.1e). The diffusion coefficients are estimated from chronoamperometry and the corresponding Cottrell plots (equation 2.1) (Figure 3.1f). For Q and QH_2 molecules, the diffusion coefficients are 5.58×10^{-6} cm^2/s and 6.89×10^{-6} cm^2/s, respectively, in line with the values reported in the literature[34–36].

To understand the electron transfer kinetics of the quinone redox reaction, rotating disk electrode (RDE) and rotating ring disk electrode (RRDE) studies are carried out with 1 mM QH_2 (or 1 mM Q) in 0.5 M H_2SO_4, Figure 3.2 and Figure 3.3a. The evident presence of positive current confirms the QH_2 oxidation with increase of limiting current with the RPM as expected, Figure 3.2a. The Koutecky–Levich plot (K–L plot) (equations 2.4, 2.5) extracted from corresponding linear sweep voltammograms (LSVs), Figure 3.2b, on a Pt disk electrode indicate that the number of electrons transferred is close to 2, and the electron transfer rate constant is in the range of 10^{-4} cm/s, demonstrating a reasonably fast redox reaction, Figure 3.2d and Table 3.1.

The RRDE profile with the evident presence of ring currents when the Pt ring is biased at the Q reduction potential and the Pt disk is swept toward the QH_2 oxidation potential, Figure 3.3a, suggests that its hydrogenation/dehydrogenation can be electrochemically reversed within the available potential window. In essence, the redox reactions of quinone are proton-coupled, and they undergo reasonably fast electron transfer, and both redox states exhibit decent stability under chosen experimental conditions[33,37,38].

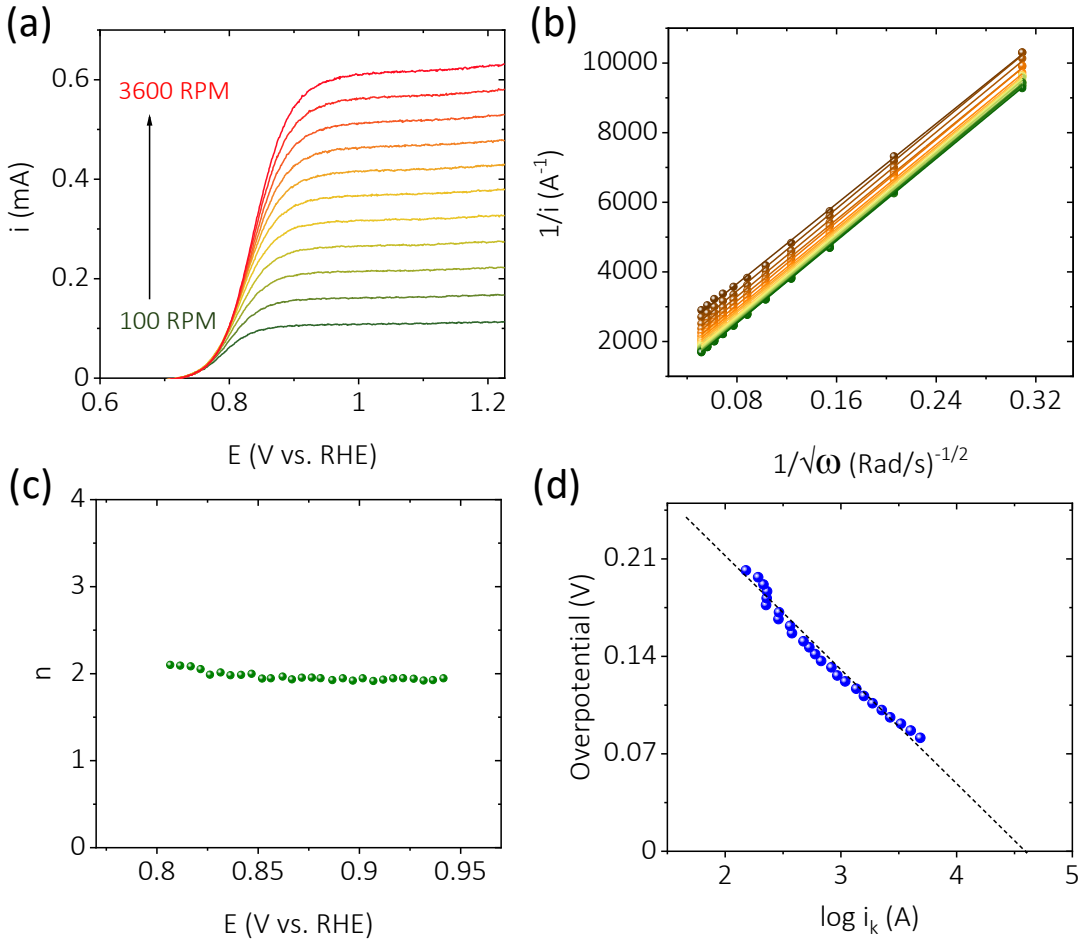

***Figure 3.2**: RDE studies for (a) QH_2 oxidation (1 mM QH_2 in 0.5 M H_2SO_4), and (b) K–L plots extracted from for QH_2 oxidation. (c) the number electrons involved and (d) log I_k vs overpotential.*

***Table 3.1**: Electrochemical parameters obtained from hydrodynamic voltammetry analysis*

Species	No: of electrons (n)	Symmetry factor (β)	Rate constant (cm/s)
Hydroquinone	*2*	*0.46*	*$1.3^{*}10^{-4}$*

To further understand the stability and the nature of the species generated at the electrode/electrolyte interface during the redox reactions of quinone, we carried out in situ UV–vis spectroelectrochemical studies (equation 2.6) (Figure 3.3 b–d) with a solution of 1 mM QH_2 in 0.5 M H_2SO_4. During the oxidation scan, the differential spectra suggest that features corresponding to QH_2 disappeared (negative going bands) with concomitant appearance of Q features (positive bands). On reversing the scan, QH_2 bands were restored with gradual disappearance of Q features. These indicate reversibility of the reaction and stability of the corresponding species at the electrode/electrolyte interfaces[39,40].

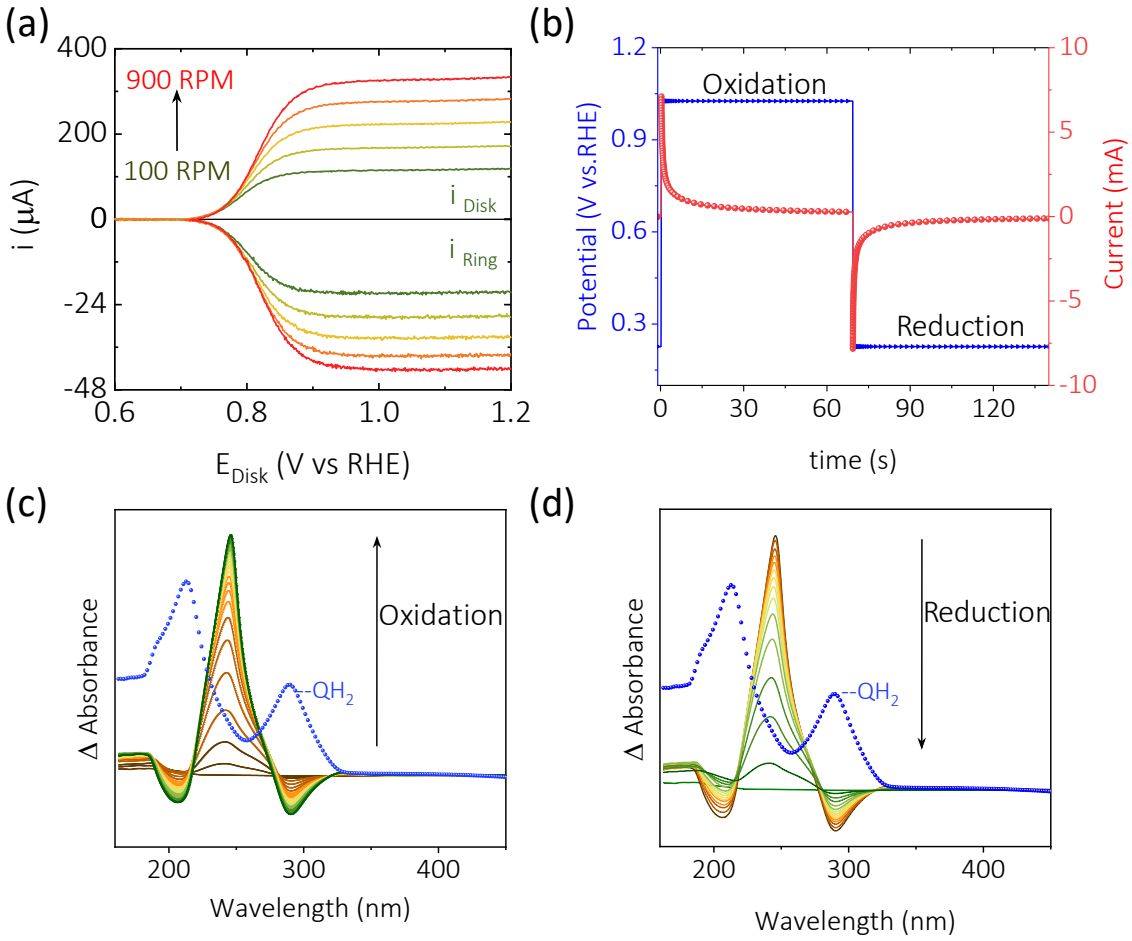

***Figure 3.3**: (a) RRDE studies for the quinone redox reaction (1 mM QH_2 dissolved in 0.5 M H_2SO_4) on a Pt disk and a Pt ring electrode at a scan rate of 10 mV/s at different rotations per minute. Oxidation is carried out potentiodynamically on the disk and potentiostatically on the ring by applying a reduction potential of 200 mV. In-situ UV-Vis spectroelectrochemistry data for the redox reaction of quinone. (b) Potential applied (V vs RHE) and Current obtained during the experiment in 1 mM hydroquinone in 0.5 M H_2SO_4 (c) The potential dependent spectra acquired during the oxidation scan and (d) during the reduction scan*

The proposed hydrogen battery is constructed as shown in (Scheme 3.1) with a Nafion 212 separator between anodic and cathodic compartments. When H_2 is filled into the negative electrode compartment constituting a Pt catalyst, the OCV with respect to the quinone composite electrode is found to be ~0.73 V, which corresponds to the difference between single electrode potentials measured with a common reference electrode (Figure 3.4a). In this configuration, because Pt is a well-known electrocatalyst for H_2 oxidation [29,30] (Figure 3.1a), generated electrons will move through the external circuit to the cathode and the H^+ ions will migrate through the proton exchange membrane to the hydrogen storage material, prompting its conversion to QH_2 (Scheme 3.1). A H_2-quinone battery can be made electrically rechargeable as QH_2 can

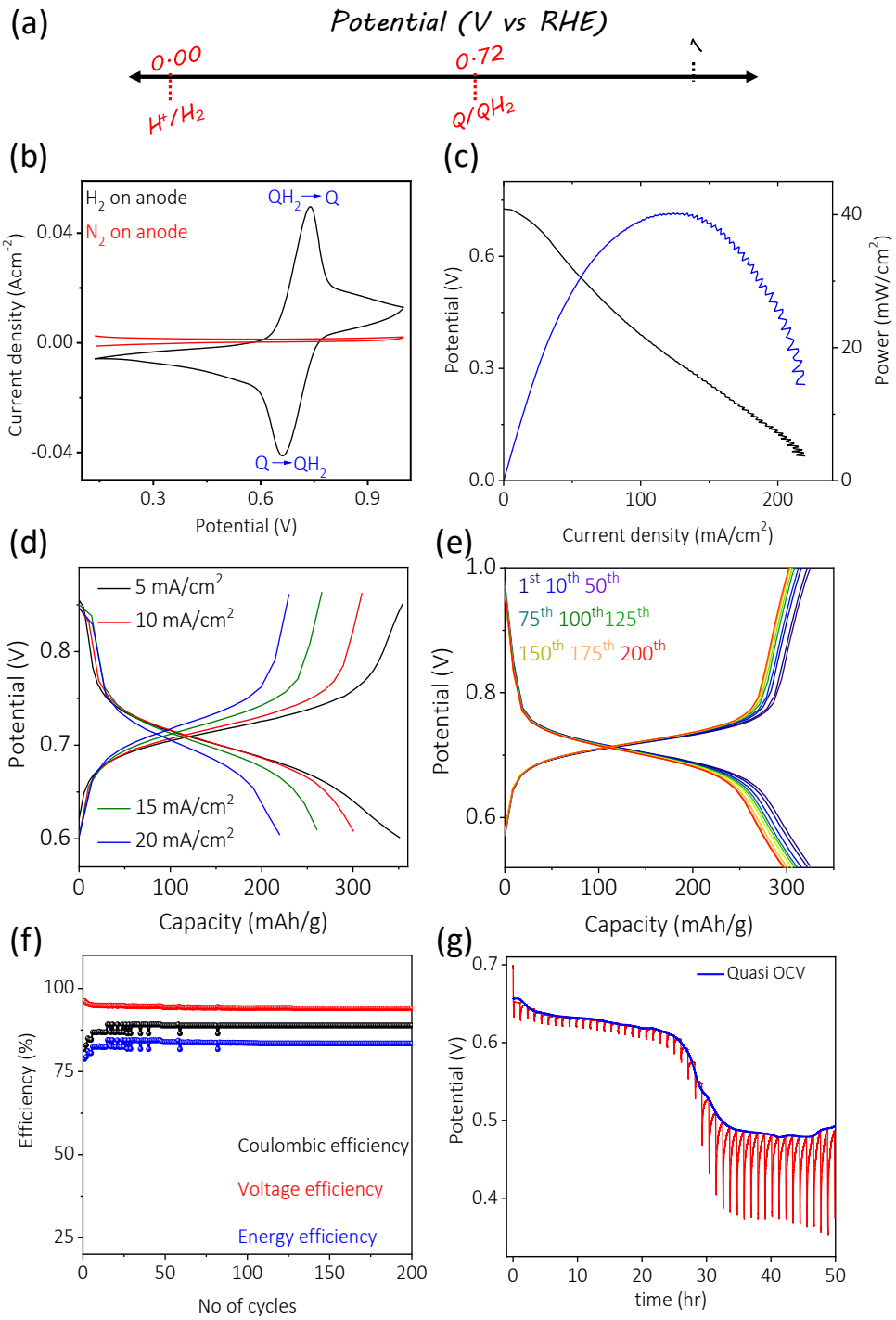

***Figure 3. 4**: (a) Single electrode potentials of Q/QH$_2$ electrode with respect to H$_2$/H$^+$ half-cell reactions. (b) Cyclic voltammogram of a hydrogen battery at a 10 mV/s scan rate with the cathode as the working electrode when the anode is continuously fed with H$_2$ (black trace) and N$_2$ (red trace) at 100 mL/min. (c) Polarization curves, (d) Galvanostatic charge–discharge curves at different rates, and (e) extended cyclability at 10 mA/cm^2 for the hydrogen battery. (f) Coulombic, voltage and energy efficiency of hydrogen battery for 200 cycles. (g) Galvanostatic intermittent titration technique (GITT) data collected for the hydrogen battery. A discharge current of 250 μA is applied for 5 minutes and then the system is relaxed at zero current to the open circuit voltage (OCV) for an hour*

be electrochemically oxidized, Figures 3.1-3.3. Further, H_2 evolution can be catalyzed by a Pt electrode on the anode side during the charge reaction (Figure 3.1a).

The cyclic voltammogram of the H_2-quinone battery with the cathode (0.1 M Q in 0.5 M H_2SO_4 at 100 mL/min) as the working electrode demonstrates very clearly electrochemical hydrogenation/dehydrogenation of the quinone electrode when the anodic compartment is continuously supplied with hydrogen (at a flow rate of 100 mL/min, Figure 3.4b, black trace). When the anodic compartment was supplied with N_2, the corresponding cyclic voltammogram did not furnish any faradaic behavior, Figure 3.4b red trace, signaling a counter reaction that is inevitably proton-assisted. The polarization curve for rechargeable hydrogen battery with a stagnant H_2 anode where the amount of H_2 is ~2 times in excess of the cathode and a flow-through Q cathode (0.1 M Q solution in 0.5 M H_2SO_4 at a flow rate of 100 mL per minute) is shown in Figure 3.4c, demonstrating a power density of ~40 mW/cm^2 at a peak current of ~125 mA/cm^2. At a rate of 5 mA/cm^2, the battery delivered a discharge capacity of ~350 mAh/g with respect to the weight of Q, Figure 3.4d, which is ~70% of its theoretical discharge capacity (495.8 mAh/g with respect to Q). This corresponds to an energy density of ~234 Wh/kg, which is ~67% of its theoretical specific energy (347.06 Wh/kg). The lower experimental capacity and specific energy compared to theoretical values could be due to higher electronic resistance of Q/QH_2 molecules [4,41]. Galvanostatic cycling at 10 mA/cm^2 demonstrated extended cyclability, and at the end of 200 cycles, it retained ~92% of its discharge capacity with respect to the first discharge, Figure 3.4e. Further, the battery possessed decent coulombic and energy efficiency for over 200 cycles, Figure 3.4f. The discharge and charge chemistries are probed by analyzing the cathodes after charge–discharge chemistry by various physicochemical techniques. The galvanostatic intermittent titration technique (GITT) is utilized for the H_2-quinone battery to decipher thermodynamic and kinetic parameters. GITT is performed by applying a discharge current of 250 μA to a stagnant Q cathode (~7 mg/cm^2) for 5 min and then relaxing the system at zero current to the open-circuit voltage (OCV) for 1 h. A stagnant H_2 electrode with hydrogen content ~2 times in excess of the cathode is employed as the anode. The processes of discharging and relaxing are repeated for several hours to understand the phase change and chemical diffusion coefficients. As shown by the blue line in Figure 3.4g the quasi-OCV demonstrated a decline from ~600 to ~480 mV at ~25 h, suggesting a clear phase change at the Q electrode. The chemical diffusion coefficient of the H^+-ion in the Q composite electrode is found to be 0.25×10^{-7} cm^2/s.

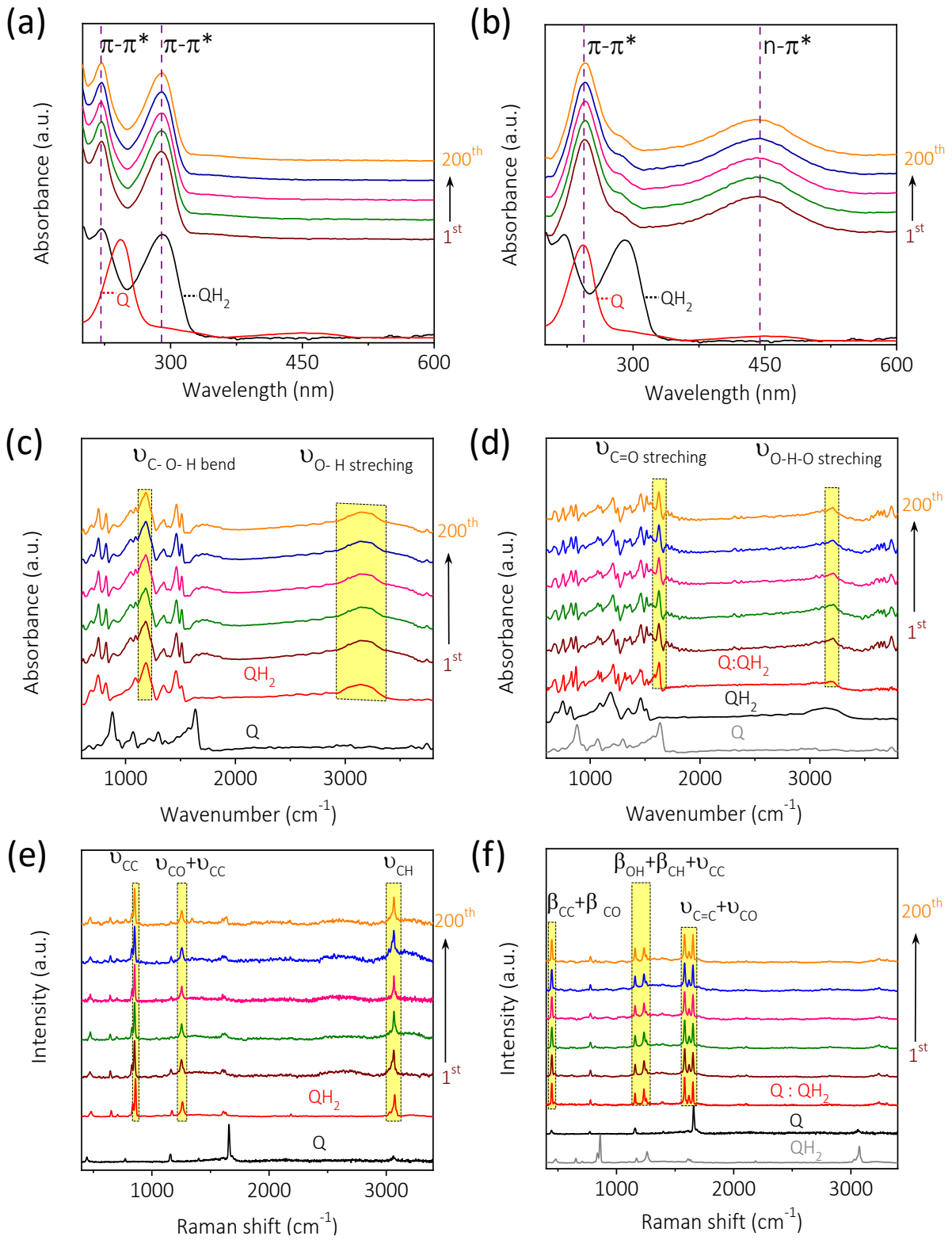

Figure 3.5: *UV–vis spectra of the H_2-quinone battery cathode (a) during the discharge and (b) during the charge cycles. FTIR spectra of the H_2-quinone battery cathode (c) during the discharge and (d) during the charge cycles. RAMAN spectra of the H_2-quinone battery cathode (e) during the discharge and (f) during the charge cycles.*

UV–vis spectroscopy demonstrates the attenuation between Q and QH_2 during discharge chemistry and its reversal during charge chemistry, Figure 3.5a,b. The sustainability of the process can be seen over 200 cycles during discharge and charge chemistry. The appearance of a broad ν_{OH} vibration at ~3160 cm^{-1} and the disappearance of ν_{CO} at ~1630 cm^{-1} in the Fourier transform infrared (FTIR) spectra of the Q cathode (Figure 3.5c) signal the formation of QH_2 during the discharge chemistry [42–44]. In line with this, Raman spectra (Figure 3.5e) demonstrate the appearance of QH_2 bands, [43,44] which further reinforce the hydrogenation of Q during the discharge chemistry of the H_2-quinone battery. However, during the charge chemistry, the presence of a sharp ν_{OHO} vibration at ~3200 cm^{-1} together with ν_{CO} at ~1630 cm^{-1} in the FTIR spectra (Figure 3.5d) is evidence for the formation of quinhydrone, the charge transfer complex between Q and QH_2. Raman spectra of the charged cathode (Figure 3.5f) further indicate the formation of quinhydrone.

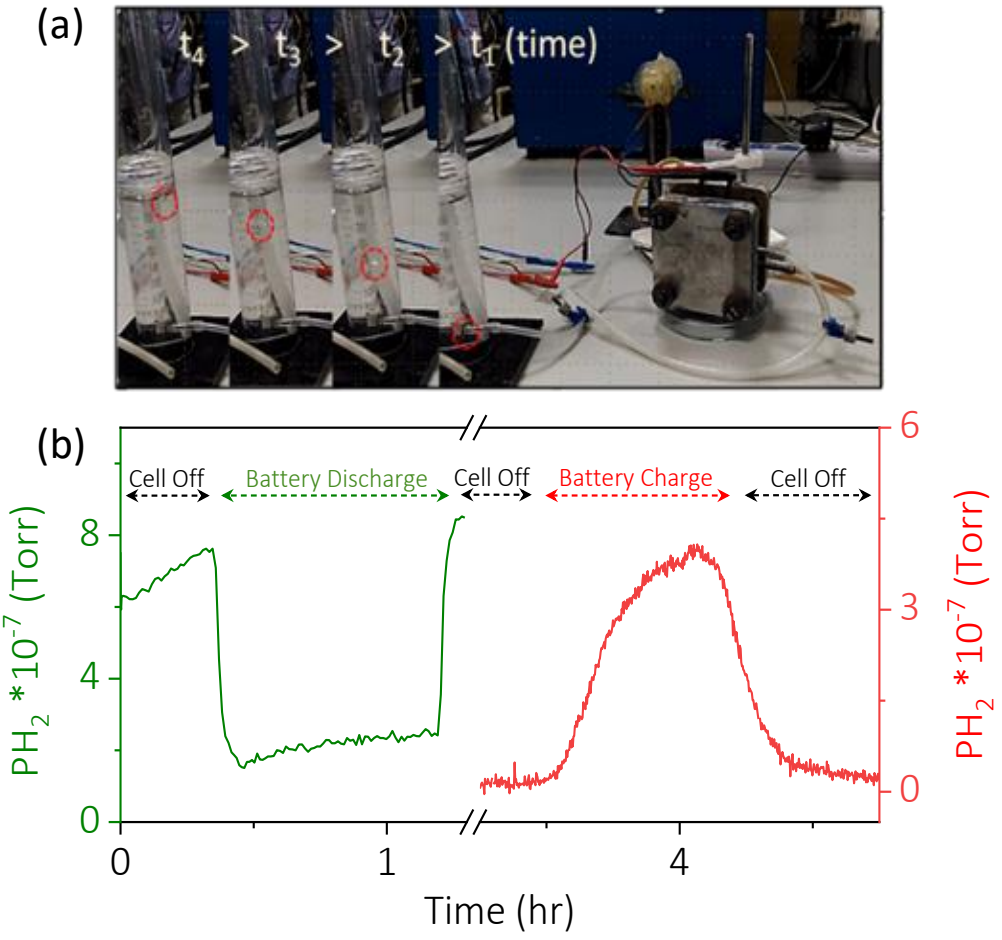

***Figure 3.6**: (a) Time-lapse photograph of the battery on charging with an electrical bias shows gas evolution where time (sec) $t_1 < t_2 < t_3 < t_4$. (b) In-situ electrochemical mass spectrometric analysis of the gaseous species evolved from the negative half-cell of the battery during discharge (green trace) and charge (red trace).*

The formation of charge transfer complexes will be a matter of future investigations, and we believe it could be due to exposure of the cathode to air during characterizations because it was not detected during in-situ spectroelectrochemistry studies conducted under a N_2 blanket (Figure 3.3b-d). The gas evolution from the negative electrode on battery charge was observed on battery charge Figure 3.6a, the Time-lapse photograph of the battery on charging. The in-situ electrochemical mass spectrometric analysis of the same compartment Figure 3.6b confirms the consumption of hydrogen on battery discharge (green trace) as well as hydrogen is exhaled on battery charge (red trace). Nevertheless, these demonstrate a rechargeable H_2-quinone battery where the cathodic reaction is electrochemical hydrogenation/dehydrogenation with corresponding hydrogen oxidation/hydrogen evolution at the anode.

On the basis of these, equations 3.1, 3.2 and Scheme 3.2 are proposed for discharge and charge chemistries, and they involve oxidation of H_2 at the anode and migration of H^+ through the proton exchange membrane to the hydrogen storage material (Q), prompting its hydrogenation to hydroquinone (QH_2) equation 3.3. Upon electrochemical charging, the processes are reversed: Scheme 3.2b with dehydrogenation of QH_2 at the cathode with simultaneous H_2 evolution on the anode.

Negative electrode	H_2	$\rightarrow 2H^+ + 2e^-$	(eq. 3.1)
Positive electrode	$Q + 2H^+ + 2e^-$	$\rightarrow QH_2$	(eq. 3.2)
Net cell reaction	$H_2 + Q$	$\rightarrow QH_2$	(eq. 3.3)

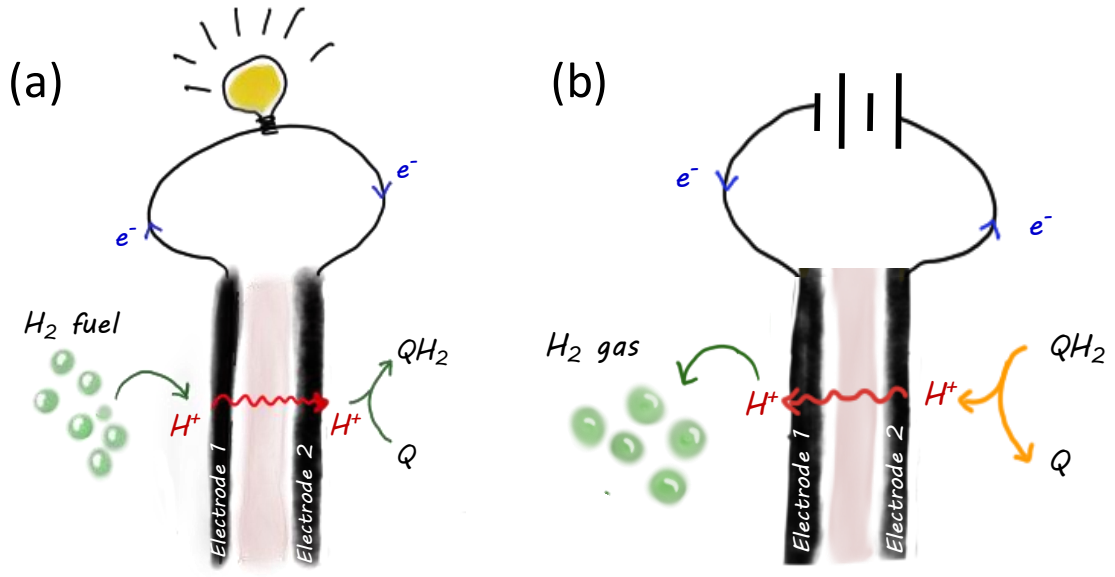

***Scheme 3.2**: Schematic representation of H_2-Q battery (a) discharge and (b) charge on electrical bias application*

To understand quinone crossover from the cathode to anode and associated poisoning of the anodic Pt electrocatalyst, we have carried out time-dependent cyclic voltammetry in a diffusion cell. Stagnant solutions of 0.5 M H_2SO_4 and 0.1 M Q in 0.5 M H_2SO_4 are taken in anodic and cathodic half-cells, respectively, and the crossover of Q from the cathode to anode is investigated by a time-dependent cyclic voltammogram with a Pt electrode as the working electrode, Pt foil as the counter electrode, and Ag/AgCl (3 M KCl) as the reference electrode. The voltammograms recorded at the Pt working electrode, Figure 3.7, indicate growing signals due to quinone redox behavior with an increase in time (inset of Figure 3.7). This suggests crossover of Q through the Nafion membrane. Poisoning of the Pt electrode by quinone molecules is investigated by monitoring the intensity of HER and HOR currents on the same Pt electrode as a function of time during the quinone crossover. HER/HOR currents on Pt (at potentials close to 0 V vs RHE) remained unaffected over a period of 7 h even though the quinone redox behavior increased with respect to time (Figure 3.7). This suggests that poisoning of the Pt electrode is negligible within the time limit of the experiment.

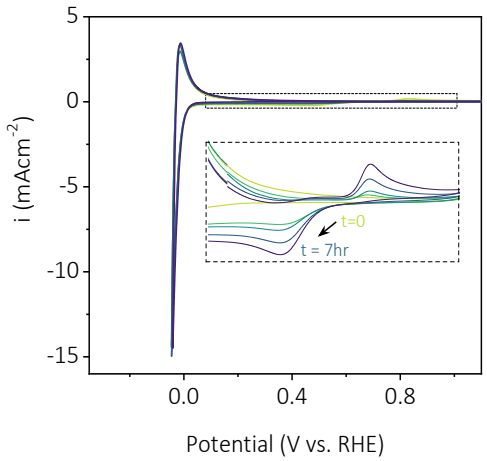

***Figure 3.7**: Time dependent cyclic voltammograms recorded on a Pt electrode (at 20 mV/s) kept in the anodic compartment of a diffusion cell constituting 0.5 M H_2SO_4 and 0.1 M Q in 0.5 M H_2SO_4 respectively in anodic and cathodic half-cells. The counter electrode is a Pt foil and the reference electrode is Ag/AgCl (3 M KCl). Inset shows the growing signals for the Q/QH_2 redox couple with increase in time.*

Conclusion

An electrically rechargeable hydrogen battery is demonstrated by coupling proton-coupled electron transfer in a Q/QH_2 redox couple and the H_2 redox reaction. UV–vis, RRDE, GITT, FTIR, and Raman

spectroscopy techniques evidence the involvement of protons during the charge–discharge chemistry and extended cycling. In an era of paramount pollution and global climate change, a battery concept based on a virtually nonpolluting chemical energy carrier molecule is a distinct step toward building green energy storage modules.

References:

1. Schafzahl, L.; Mahne, N.; Schafzahl, B.; Wilkening, M.; Slugovc,C.; Borisov, S. M.; Freunberger, S,.*Angew. Chem., Int. Ed.*2017,**56**, 15728−15732.
2. Mourad, E.; Coustan, L.; Lannelongue, P.; Zigah, D.; Mehdi, A.;Vioux, A.; Freunberger, S. A.; Favier, F.; Fontaine, O. *Nat. Mater.*2017,**16(4)**, 446−453.
3. Chinnam, P. R.; Fall, B.; Dikin, D. A.; Jalil, A. A.; Hamilton, C. R.;Wunder, S. L.; Zdilla, M. J. *Angew. Chem.* 2016,**128**, 15480−15483.
4. Miroshnikov, M.; Divya, K. P.; Babu, G.; Meiyazhagan, A.; ReddyArava, L. M.; Ajayan, P. M.; John, G. *J. Mater. Chem. A*, 2016, **4(32)**, 12370−12386.
5. Maiyalagan, T.; Alaje, T. O.; Scott, K. *J. Phys. Chem. C*. 2012,**116(3)**, 2630−2638.
6. Osmieri, L.; Escudero-Cid, R.; Monteverde Videla, A. H. A.;Ocón, P.; Specchia, S. *Appl. Catal., B*. 2017,**201**, 253−265.
7. Goodwin, S.; Walsh, D. A. *ACS Appl. Mater. Interfaces*. 2017,**9(28)**, 23654−23661.
8. Cavaliere, S.; Subianto, S.; Savych, I.; Jones, D. J.; Rozière, J. *Energy Environ. Sci.* 2011,**4(12)**, 4761−4785.
9. Larcher, D.; Tarascon, J.-M. *Nat. Chem.*2015,**7(1)**, 19−29.
10. Forsyth, M.; Yoon, H.; Chen, F.; Zhu, H.; MacFarlane, D. R.;Armand, M.; Howlett, P. C. *J. Phys. Chem. C*. 2016,**120(8)**, 4276−4286.
11. Anju, V. G.; Manjunatha, R.; Austeria, P. M.; Sampath, S.*J. Mater. Chem. A*. 2016,**4(14)**, 5258−5264.
12. Fakharuddin, A.; Jose, R.; Brown, T. M.; Fabregat-Santiago, F.;Bisquert, J. *Energy Environ. Sci.* 2014, **7(12)**, 3952−3981.
13. Kucernak, A. R. J.; Naranammalpuram Sundaram, V. N. *J.Mater. Chem. A* 2014, **2(41)**, 17435−17445.
14. Choi, N. S.; Chen, Z.; Freunberger, S. A.; Ji, X.; Sun, Y. K.;Amine, K.; Yushin, G.; Nazar, L. F.; Cho, J.; Bruce, P. G. *Angew. Chem., Int. Ed.* 2012, **51(40)**, 9994−10024.

15. Vlad, A.; Singh, N.; Galande, C.; Ajayan, P. M. *Adv. Energy Mater.* 2015, **5(19)**, 1402115.
16. Suresh, S.; Wu, Z. P.; Bartolucci, S. F.; Basu, S.; Mukherjee, R.;Gupta, T.; Hundekar, P.; Shi, Y.; Lu, T. M.; Koratkar, N. *ACS Nano* 2017,**11(5)**, 5051−5061.
17. Hassoun, J.; Panero, S.; Reale, P.; Scrosati, B. *Adv. Mater.*2009, **21(47)**, 4807−4810.
18. Hong, S. M.; Etacheri, V.; Hong, C. N.; Choi, S. W.; Lee, K. B.;Pol, V. G *ACS Appl. Mater. Interfaces*. 2017, **9(22)**, 18790−18798.
19. Abraham, K. M. *J. Phys. Chem. Lett.* 2015,**6(5)**, 830−844.
20. Reddy, M. V.; Subba Rao, G. V.; Chowdari, B. V. R. *Chem.Rev.*2013,**113(7)**, 5364−5457.
21. Kreuer, K. D.*Chem. Mater.*2014, **26(1)**, 361−380.
22. Kannan, R.; Kakade, B. A.; Pillai, V. K. *Angew. Chem., Int. Ed.* 2008,**47(14)**, 2653−2656.
23. Gao, P. C.; Tsai, W. Y.; Daffos, B.; Taberna, P. L.; Pérez, C. R.;Gogotsi, Y.; Simon, P.; Favier, F. *Nano Energy*.2015,**12**, 197−206.
24. Chalk, S. G.; Miller, J. F.*J. Power Sources*. 2006,**159**,73−80.
25. Grätzel, M.*Nature* 2001,**414**, 338−344.
26. Schlapbach, L.; Züttel, A. *Nature*. 2001,**414**, 353−358.
27. Lubitz, W.; Tumas, W. *Chem. Rev.*2007,**107(10)**, 3900−3903.
28. Momirlan, M.; Veziroglu, T. N. *Int.J. Hydrogen Energy*. 2005,**30**, 795−802.
29. Huan, T. N.; Jane, R. T.; Benayad, A.; Guetaz, L.; Tran, P. D.;Artero, V. *Energy Environ.Sci.*2016,**9(3)**, 940−947.
30. Kucernak, A. R.; Zalitis, C. *J. Phys. Chem. C*. 2016,**120(20)**, 10721−10745.
31. Quan, M.; Sanchez, D.; Wasylkiw, M. F.; Smith, D. K. *J. Am. Chem. Soc.* 2007,**129(8)**, 12847−12856.
32. Wedege, K.; Dražević, E.; Konya, D.; Bentien, A. *Sci. Rep.* 2016, **6**, 39101.
33. Huskinson, B.; Marshak, M. P.; Suh, C.; Er, S.; Gerhardt, M. R.;Galvin, C. J.; Chen, X.; Aspuru-Guzik, A.; Gordon, R. G.; Aziz, M. J. *Nature*. 2014, **505**, 195.
34. Nowinski, S. A.; Anjo, D. M.*J. Chem. Eng. Data*1989,**34(3)**, 265−268.
35. Yap, W. T.; Doane, L. M. *Anal. Chem.*1982,**54(8)**, 1437−1439.
36. Flarsheim, W. M.; Tsou, Y.; Trachtenberg, I.; Johnston, K. P.;Bard, A. J. *J. Phys.Chem.*1986, **90(10)**, 3857−3862.
37. Mirkhalaf, F.; Tammeveski, K.; Schiffrin, D. J. *Phys. Chem. Chem. Phys.*2004, **6(6)**, 1321−1327.
38. Wang, F.; Hu, S. *Electrochim. Acta*. 2006,**51(20)**, 4228−4235.
39. Armendáriz-Vidales, G.; Frontana, C. *Phys. Chem. Chem. Phys.*2015,**17(43)**, 29299−29304.

40. Mirzakulova, E.; Khatmullin, R.; Walpita, J.; Corrigan, T.;Vargas-Barbosa, N. M.; Vyas, S.; Oottikkal, S.; Manzer, S. F.; Hadad,C. M.; Glusac, K. D. *Nat. Chem.*2012,**4(10)**, 794−801.
41. Song, Z.; Zhou, H. *EnergyEnviron. Sci.*2013,**6(8)**, 2280−2301.
42. Trivedi, P.; Patel, R. G.; Patel, A.; Patel, V.; Oza, A. T. *Indian Journal of Pure and Applied Physics* 2005,**43**, 335−340.
43. Kubinyi, M. J.; Keresztury, G. *Mikrochim. Acta*1997,**14**,525−528.
44. Kubinyi, M. J.; Keresztury, G. *Spectrochim.Acta*1989,**45**, 421−429

Chapter 4:

An Air Chargeable Hydrogen Battery

Abstract*:* The chapter discusses an air chargeable hydrogen battery chemistry wherein the two major aspects of hydrogen economy such as hydrogen storage and its utilization are combined in a single device. During the discharge chemistry, the battery electrochemically traps the protons in a hydrogen carrying quinone moiety while delivering electric power. The redox energy positioning of molecular oxygen above that of the reversible proton-coupled electron transfer in the quinone moiety, uniquely allow the charging of the battery with ambient air during concomitant electrical power production. The prospects of charging the battery with ambient air without the necessity of an external voltage will be immensely useful for isolated/rural areas and military operations at challenging geography.

The chapter contains the data taken from my original published work: Neethu C. D. etal ***Green Chem.***, 2022,**24**, 8820-8826.

Introduction

The industrial revolution caused the rapid hike in the use of fossil fuels for energy conversion which has kept on increasing even in the 21st century.[1] Moreover, pollution, global warming, and climate change have outnumbered its advantages.[2-7] In 2019, the annual global carbon dioxide (CO_2) emissions reached 38 gigatons (Gt) due to extensive and unrestricted use of fossil fuels.[8,9] The current energy consumption which is ~585 exajoules (EJ)/year is expected to increase by at least 50% in the coming 20 years.[8,9] Though Li-ion batteries have revolutionised the portable electronic market for more than a decade, there are concerns related to the availability of raw materials and their cost.[4,7,10-13] To overcome the growing energy demands, and the challenges associated with carbon-based energy economy and conventional energy storage technologies, a transition to carbon neutral energy economy is inevitable which demand the development of environmentally friendly and affordable energy storage devices.[2-7,10-17] All of these mandates the focus on hydrogen economy, which refers to the use of dihydrogen as a fuel whose combustion in principle should be carbon neutral.[5,18,19] Though this hydrogen-based energy economy by utilizing renewable and abundant energy sources is a promising energy vector, the temporal and geographic variations of renewable energy resources, introduce a mismatch between the peak of its availability and the peak of its demand.[5-7,15,19]

This chapter demonstrate the possibility of charging of a hydrogen battery with air, whose supply in principle is constant and infinite. This hydrogen battery electrochemically traps the protons in a quinone based molecule during the discharge chemistry. During the air charge process, the protons are released from the quinone molecule; however, quite interestingly with electric power production (Scheme 4.1). The basic working principle involves reversible shuttling of protons trapped in the quinone moiety during charging and discharging between the anode and the cathode, making it a reversible hydrogen battery. As the battery can be charged with air, with concomitant power generation, this strategy will be immensely useful for rural areas/isolated areas and military operations. The proposed air chargeable battery encompasses two aspects of hydrogen economy such as storage and utilization of hydrogen in the same device which distinguishes it from a conventional H_2-O_2 fuel cell. The main aspect of this system is that it releases electricity even during the air charge process. Since this single device incorporates two major facets of the hydrogen economy, is believed to be a major leap in hydrogen economy.

Results and discussion

The proposed air chargeable hydrogen battery consists of a negative electrode encompassing an electrocatalyst which can catalyze both hydrogen oxidation (HOR) and oxygen reduction reactions (ORR), Scheme 4.1. To demonstrate the concept, platinum loaded carbon (Pt/C with 0.5 mg/ cm^2 loading) was chosen as the electrocatalyst as it is a benchmark catalyst for both HOR and ORR.[20-23] Quinone/hydroquinone (Q/QH_2) redox couple was chosen as the positive electrode as it can store hydrogen,[24-28] and Q/QH_2 redox potential lie in between that of HOR and ORR, single electrode potentials Figure 4.1a. The battery is fabricated by sandwiching a Nafion 212 membrane between the Pt electrode and quinone electrode (Scheme 4.1). The battery discharge takes place between H_2 and Q electrode whereas the air charging takes place between QH_2 and O_2 electrodes as depicted in Scheme 4.1. The proposed battery discharge chemistry/charge chemistry is predicted based upon the single electrode potentials (Figure 4.1a) where the redox potentials of Q/QH_2 lies between that of H^+/H_2 and O_2/H_2O redox species. This is supported by the cyclic voltammograms, Figure 4.1b, suggesting that H^+/H_2 is more negative with respect to Q/QH_2 making the discharge feasible. On the other hand, the Q/QH_2 is more negative with respect to O_2/H_2O making the charge chemistry again a thermodynamically downhill process.

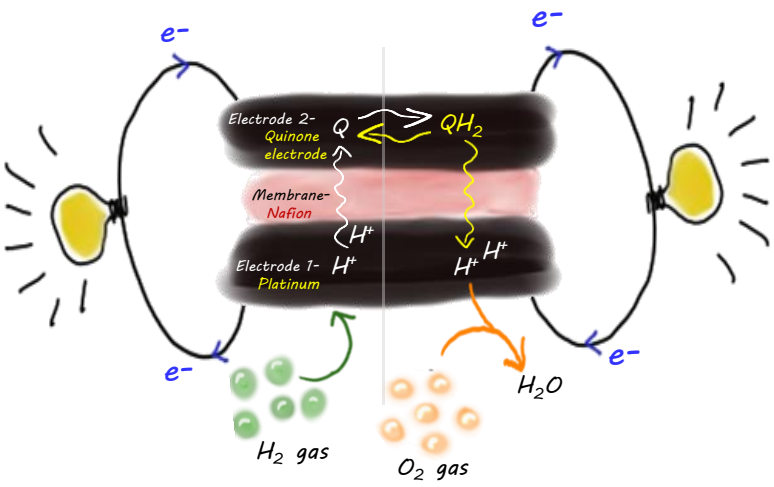

Scheme 4.1: *Schematic representation of the air chargeable hydrogen battery.*

The Q/QH_2 half-cell which is common for the discharge and charge cycles should possess reversible electrochemical hydrogenation/dehydrogenation. The Q/QH_2 redox couple involves protons along with electrons, with a commendable electrochemical stability, reversibility with a symmetry factor of β= 0.5 as well

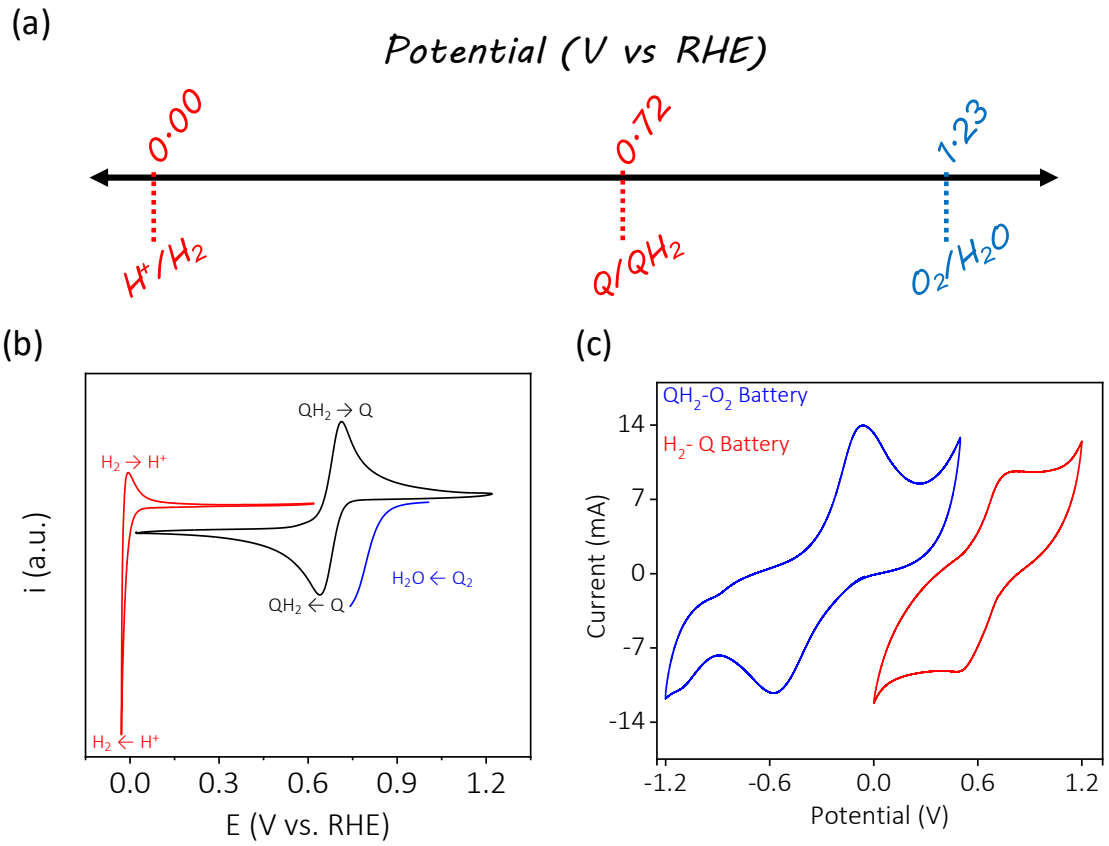

Figure 4.1: *(a) Single electrode potentials of Q/QH_2 electrode with respect to H_2/H^+ and O_2/H_2O half-cell reactions. (b) Voltammograms of quinone (Q) redox reaction (on a glassy carbon electrode), hydrogen oxidation reaction and oxygen reduction reaction (on a platinum working electrode) in 0.5 M H_2SO_4. (c) Voltammograms of H_2-Q battery (red line) and QH_2-O_2 battery (blue line) in the battery architecture at 5 mV/s scan rate.*

as with decent rate constant a ~10^{-4}cm/s at the electrode electrolyte interface. (Chapter 3: Figure 3.1- 3.3, Table 3.1). All these conditions favor the utility of the Q/QH_2 redox couple for the proposed air chargeable battery. The feasible formal potential of Q/QH_2 between HOR and ORR provide (Figure 4.1a,b) a battery chemistry resulting in electric power generation during the discharge as well as air charge processes. To gain more insight, cyclic voltammograms of the assembled battery was collected, with Pt/C purged with H_2 as the negative electrode and Q electrode kept under a nitrogen blanket (Figure 4.1c) as the positive electrode (working electrode). When Q was the working electrode and on passing H_2 to Pt/C compartment, the redox energy of Q/QH_2 conversion (red line, Figure 4.1c) happened on the positive potential side suggesting it functions as an electron acceptor. On the other hand, with QH_2 as working electrode, and on feeding the Pt/C compartment with O_2, the redox energy of Q/QH_2 occurred on the negative potential scale (blue line, Figure 4.1c) suggesting it serves as an electron donor. These suggest that Q/QH_2 redox couple performs dual

functions; being the cathode for H_2-Q battery and anode for QH_2-O_2 battery. Thus, the proposed reactions are:

with Hydrogen

Pt/C electrode (anode)	$H_2 \rightarrow 2H^+ + 2e^-$	$E^0 = 0$ V vs SHE	(eq. 4.1)
Quinone electrode (cathode)	$Q + 2H^+ + 2e^- \rightarrow QH_2$	$E^0 = 0.699$ V vs SHE	(eq. 4.2)

with Oxygen

Quinone electrode (anode)	$QH_2 \rightarrow Q + 2H^+ + 2e^-$	$E^0 = 0.699$V vs SHE	(eq. 4.3)
Pt/C electrode (cathode)	$\frac{1}{2}O_2 + 2H^+ + 2e^- \rightarrow H_2O$	$E^0 = 1.23$ V vs SHE	(eq. 4.4)

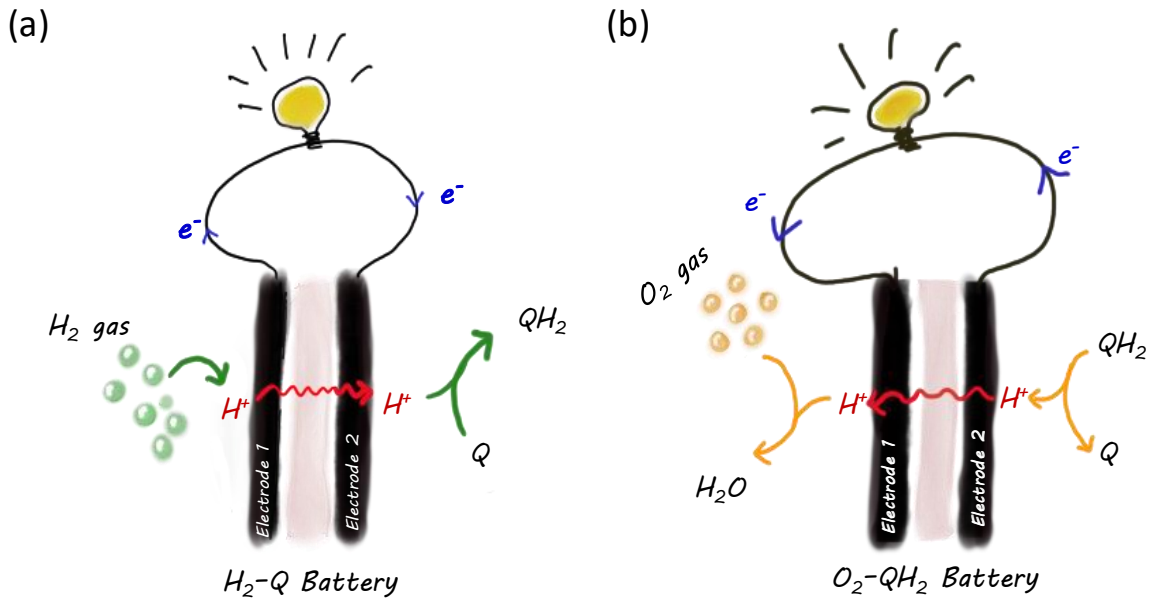

Scheme 4.2*: Schematic representation of reactions occurring at the (a) H_2-Q battery and (b) QH_2-O_2 battery.*

When H_2 is purged into Pt/C electrode compartment, the open circuit voltage was found to be ~0.7 V, which is commensurate with the electrode reactions shown in equations 4.1 and 4.2. Since Pt/C is the benchmark electro-catalyst for hydrogen oxidation reaction (HOR),[17,18] the electrons produced will perform work on the surroundings by their organized motion, and the H^+-ions migrate through the Nafion 212 membrane to the hydrogen acceptor Q molecule, thereby getting converted to QH_2, Scheme 4.1, 4.2a. At this stage if Pt/C compartment is fed with O_2, a better electron acceptor than Q (Scheme 4.1, 4.2b) the electron flow will be reversed, and it will be from quinone electrode to Pt/C electrode powering the load again with concomitant H^+-ions migration in the opposite direction, equations 4.3 and 4.4. This is possible mainly

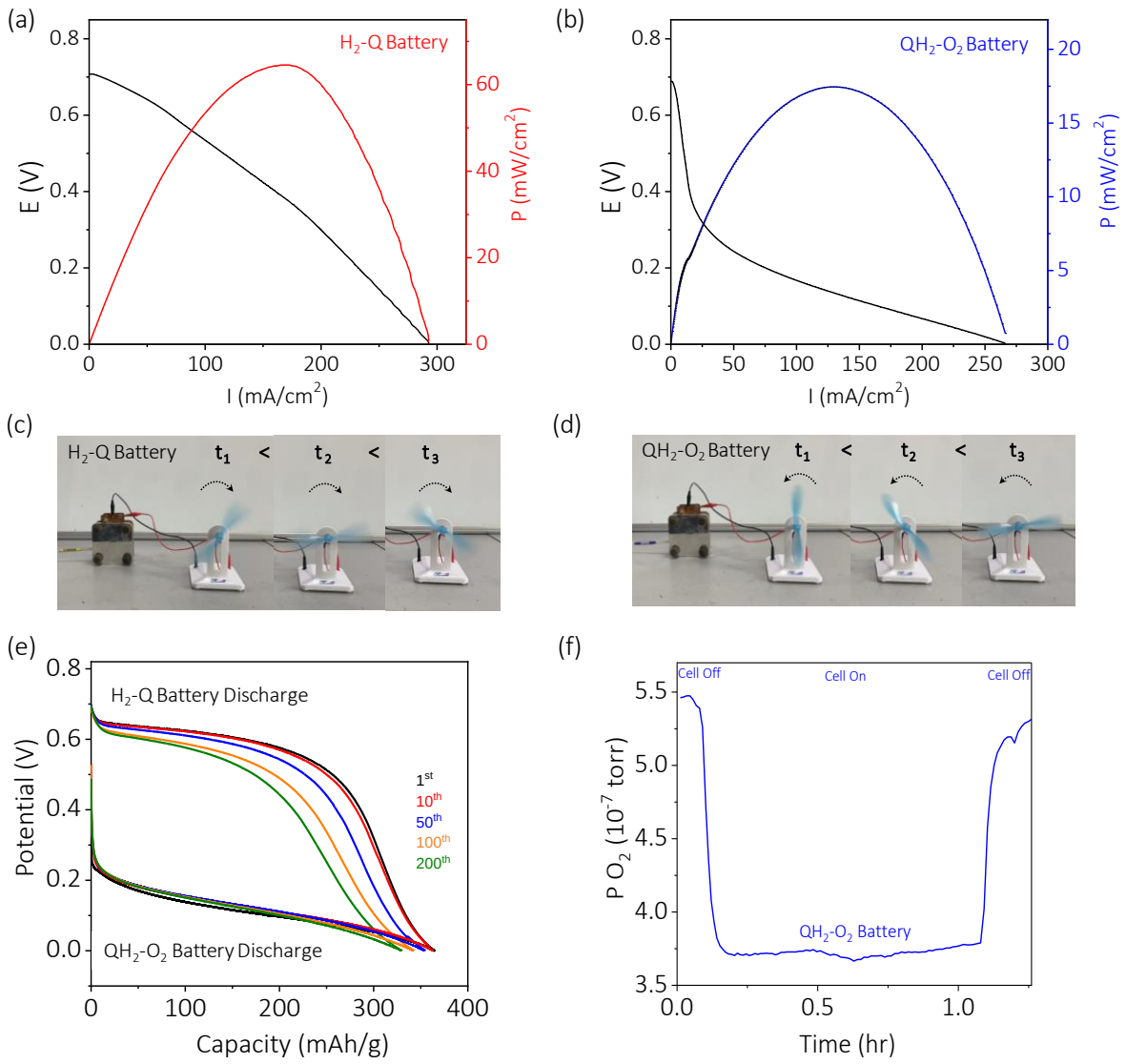

Figure 4.2: *Polarization curves for (a) H_2-Q battery and (b) QH_2-O_2 battery. Time-lapse photograph of the (c) H_2-Q battery discharge (clock-wise rotation of fan) and (d) QH_2-O_2 battery discharge (anti-clock-wise rotation of fan) where time (sec) $t_1 < t_2 < t_3$. (e) Galvanostatic cycling curves for H_2-Q (10 mA/cm²) and QH_2-O_2 (10 mA/cm²) batteries by alternatively filling the Pt/C compartment with H_2 and O_2. (f) In-situ electrochemical mass spectrometric analysis showing the consumption of O_2 (at the cathode) during the discharge of QH_2-O_2 battery.*

because Pt/C is also the benchmark electro-catalyst for oxygen reduction reaction (ORR).[19,20] The QH_2-O_2 battery will not only produce power but it will also make the battery ready for next burst of power as it will regenerate the Q from QH_2, equations 4.3 and 4.4. Therefore H_2 can be fed again to Pt/C compartment, making the H_2-Q battery ready for the subsequent discharge. The above-mentioned processes by alternatively filling the Pt/C electrode compartment with H_2 and O_2 can be repeated several times leading to a device which can be charged with air with simultaneous power generation. The polarization curve of H_2-Q

battery along with the corresponding polarization of QH_2-O_2 battery, Figure 4.2a,b suggest the former can be charged with air. The H_2-Q demonstrate a power density of 65 mW/cm^2 at a peak current of 170 mA/cm^2 and the maximum current obtained from QH_2-O_2 battery was almost like that of H_2-Q battery, Figure 4.2a, b. It should be noted that no external bias is applied to charge the H_2-Q battery after the discharge and therefore the QH_2-O_2 charge the H_2-Q battery with concomitant power generation, by reversing direction of electron flow, evident from Figure 4.2c, d. On H_2-Q battery discharge, the fan operates with clockwise rotation (evident from the time lapse photograph Figure 4.2c) however on QH_2-O_2 battery discharge, it reverses the direction to anti clockwise (evident from the time lapse photograph Figure 4.2d), which proves that the current flow is reversed on QH_2-O_2 battery discharge compared to H_2-Q battery discharge. Galvanostatic polarization of H_2-Q battery at a rate of 10 mA/cm^2 delivered a discharge capacity of 350 mAh/g (Figure 4.2e) which is 70 % of its theoretical discharge capacity. The decrease in discharge capacity from the theoretical value could be due to difficulty of proton diffusion through the ionomer into the composite electrode and the electronic resistance of the organic molecules. Without electrically charging the H_2-Q battery, when the Pt/C compartment is fed with O_2, the corresponding discharge delivered approximately the same capacity however with a lower plateau, Figure 4.2e. The lower discharge plateau could be due to the complexity of 4 electron transfer associated with the scission of O_2 molecules.[29,30] After the QH_2-O_2 discharge, when the Pt/C cathode is again filled with H_2, the corresponding H_2-Q battery delivered almost a similar capacity as in the first cycle, Figure 4.2e. This demonstrates that H_2-Q battery can be charged by QH_2-O_2 battery and latter does it with power generation. The discharge of H_2-Q battery further charged the QH_2-O_2 battery and subsequent discharge of QH_2-O_2 furnished almost similar capacity as in the first cycle, Figure 4.2e. Extended cyclability of the process is given in Figure 4.2e for almost 200 cycles, by alternatively filling the Pt/C compartment with H_2 and O_2. At the end of 200 cycles, since the battery can be charged by air, the cumulative capacity (for all the cycles) delivered was found to be ~138,106 mAh/g. It should be noted that there is capacity decay during cycling and it could be due to sluggish kinetics ORR on Pt/C resulting in incomplete charging. This can be improved by modifying the membrane electrode assembly and it will be a matter of future investigations.

The half-cell chemistry at anode H_2-Q battery on discharge consuming hydrogen have been previously confirmed with by in situ electrochemical mass spectrometry (Chapter 3, Figure 3.6), which is in support with the equation 4.1 and Scheme 4.2a. The cathode half-cell analysis of the QH_2-O_2 battery discharge (air charge) by in situ electrochemical mass spectrometry demonstrates positive signal for oxygen consumption (Figure 4.2f) which in turn attests the half-cell chemistry on the air charge processes via equations 4.4 and Scheme 4.2b.

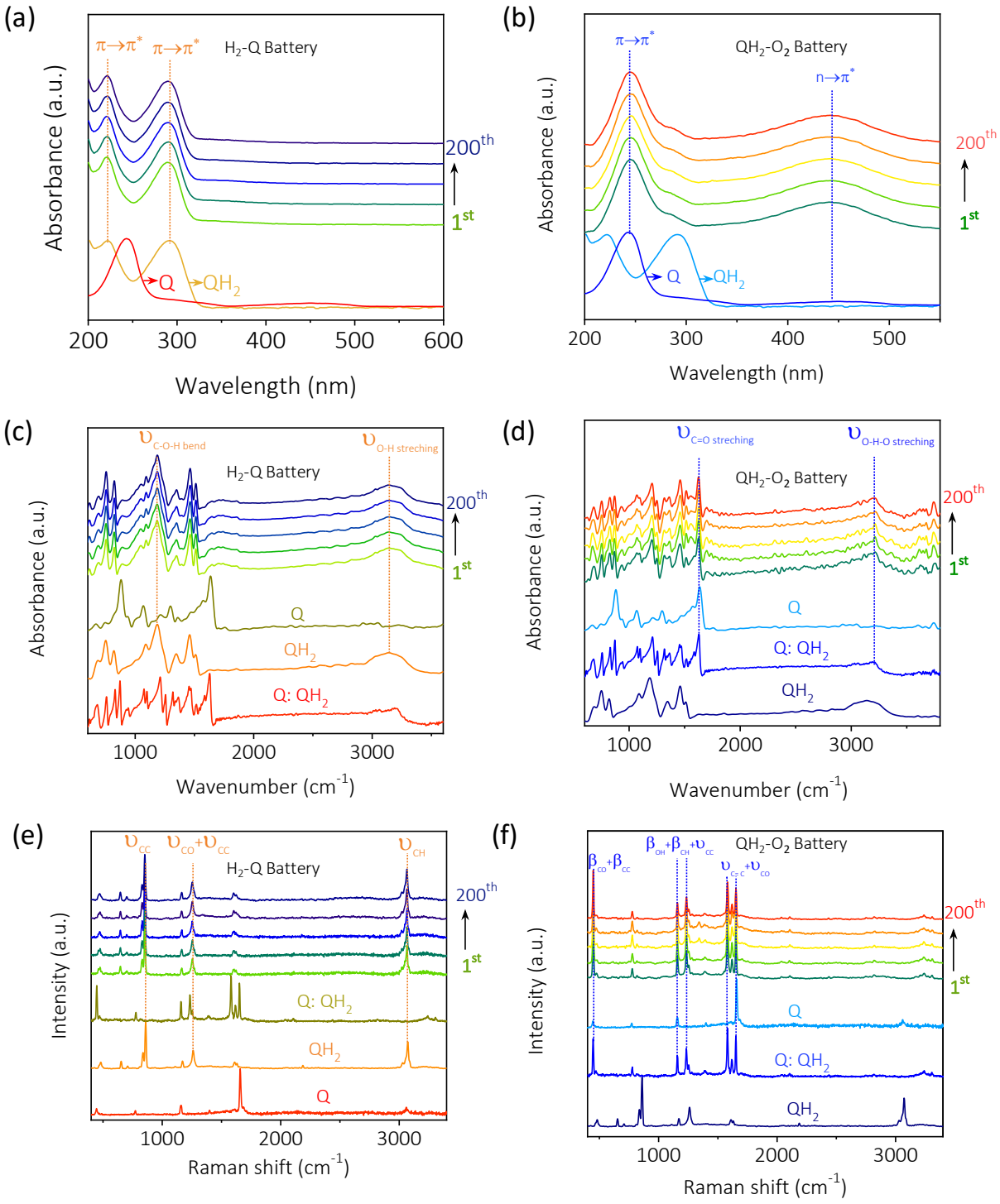

Figure 4.3: *UV–Vis spectra of (a) H_2-Q battery cathode and (b) QH_2-O_2 battery anode during different discharge cycles. FTIR spectra of (c) H_2-Q battery cathode and (d) QH_2-O_2 battery anode during different discharge cycles. Raman spectra of (e) H_2-Q battery cathode and (f) QH_2-O_2 battery anode during different discharge cycles*

To understand the discharge chemistry of the H_2-Q and QH_2-O_2 batteries, the cathode was analyzed by a range of spectroscopic techniques. The transformation of Q to QH_2 is evident from UV-Vis spectra analysis of the discharged of H_2-Q battery cathode (Figure 4.3a) and a reversal of the process was observed during the QH_2-O_2 discharge (Figure 4.3b). This indicates the discharge of H_2-Q battery charge QH_2-O_2 battery and vice versa. Extended cyclability of the discharge processes are shown in Figure 4.3a, b indicating cyclability over 200 cycles. The discharged H_2-Q battery cathode on Fourier transform infrared (FTIR) analysis exhibits a band at ~3160 cm^{-1} (Figure 4.3c) corresponding to ν_{O-H} vibration of QH_2 with the absence of $\nu_{C=O}$ at ~1630 cm^{-1} which corresponds to Q molecule. Similar results were drawn from the Raman analysis of the discharged H_2-Q battery cathode (Figure 4.3e), with the presence of QH_2 which confirms quinone hydrogenation. However, discharged QH_2-O_2 battery anode on FTIR analysis (Figure 4.3d) indicated the presence quinhydrone, the charge transfer complex between Q and QH_2 with the appearance a sharp ν_{O-H-O} vibration at ~3200 cm^{-1} together with $\nu_{C=O}$ at ~1630 cm^{-1}. Raman analysis of the discharged QH_2-O_2 battery cathode, as well confirms this observation (Figure 4.3f). This transformation was visible in the UV-Vis spectra of O_2 charged QH_2 (Figure 4.3b) by the appearance of a longer wavelength absorption band, which can be attributed to the exposure of the electrode to ambient air during the analysis. Extended cyclability of the processes is seen in Figure 4.3a-f, indicating the sustainability of the process. Taken together, the proposed hydrogen battery can be air charged and the charging process is also accompanied by electric power production.

The question that may arise is that the system is like a H_2-O_2 fuel cell. It is to be noted that our system is an energy storage device whose capacity is limited by the quantity of quinone moiety. Secondly, our system stores and utilizes hydrogen, and therefore is a step ahead of an H_2-O_2 fuel cell which is primarily a hydrogen utilization device. The special fabrication of the battery promotes hydrogen oxidation reaction during H_2-Q battery discharge and oxygen reduction reaction during QH_2-O_2 battery discharge on the same Pt electrode which avoids the requirement of heavy loading of expensive platinum electrodes as in a conventional H_2-O_2 fuel cell. In the H_2-Q battery, for the complete utilization of 1.081 gm of Q (equals to 0.01moles), the battery requires 0.01 moles of hydrogen fuel. Therefore, the subsequent discharge of H_2-Q battery should release 0.02 Farad of electric charge. The QH_2-O_2 battery discharge will account for a further release 0.02 Farad of electric charge from 0.01 moles of QH_2 when it is clubbed with 0.005 moles of oxygen. In essence, from 0.01 moles of hydrogen fuel and 0.005 moles of oxygen, cumulatively 0.04 Farad of charge could be generated (Calculation 4.1). On the contrary, in a conventional H_2-O_2 fuel cell, the direct usage of 0.01 moles of hydrogen fuel and 0.005 moles of oxygen should release only 0.02 Farad of electric charge. Therefore, our

system traps the possibility of releasing 0.04 Farad of electric charge in total, in comparison to 0.02 Farad in a conventional H_2-O_2 fuel cell. The system is completely different from a mediator fuel cell or a mediator redox flow battery,[31] where they regenerate the mediator in various ways, but none were successful in trapping that into electricity. Secondly, the overall device exhibited a cumulative capacity of 138,106 mAh (69172 mAh/g for the H_2-Q battery and 68933 for the QH_2-O_2 battery, (Calculation 4.2) with 1 g of quinone. However, to fabricate a primary H_2-Q battery with the same capacity without the possibility of air charging, one would require a huge cathode comprising ~378 gm of quinone (Calculation 4.2). Taken together, we have successfully fabricated an air chargeable hydrogen battery which utilizes the hydrogen redox and the reversibility of electrochemical hydrogenation/dehydrogenation in quinone based molecules for electric power production. The advantage of this battery chemistry is such that protons and electrons can be shuttled back and forth between the anode and the cathode during discharging and air charge processes and both the forward and reverse processes lead to the generation of electric power. The accompanying time-lapse photograph attests the prospects of air charging of the hydrogen battery with air (Figure 4.2c, d).

Calculation 4.1:

Amount(g) of Q used in 100 ml of 0.1 M solution : $\frac{108.1*0.1*100}{1000} = 1.081\ g$

No: of moles of Q : $\frac{1.081}{108.1} = 0.01\ moles$

Electric charge: 0.01* 2 = 0.02 F

Amount of hydrogen required: 0.01 moles

Amount of oxygen required: 0.005 moles

Calculation 4.2:

First discharge capacity of H_2-Q battery: 364.69 mAh/g

Cumulative capacity of H_2-Q battery after 200 cycles: 69172.91 mAh/g

Cumulative capacity of QH_2-O_2 battery after 200 cycles: 68933.5 mAh/g

Cumulative capacity of the battery in total: 138106.41 mAh/g

Amount (g) of Q required to achieve a capacity of 69172.91 mAh (Table S3) in primary battery configuration: 69172.91 / 364.69 = 189.67 g

Similarly, amount (g) of QH_2 required to achieve a capacity of 68933.5 in primary battery configuration: 68933.50 / 364.54 = 189.09 g

Therefore, cumulative capacity during discharge and air charge processes = 378.76 g

Conclusions:

In this chapter, an air chargeable hydrogen battery is successfully fabricated by exploiting the electrochemically reversible hydrogen carrying property of quinone based molecules. The proposed hydrogen battery can be charged with air during concomitant electric power generation and the overall battery chemistry involves the production of only water making the energy conversion pathways sustainable as well as green. This battery concept aided by proton trapping and shuttling with the capability for air charging will be immensely useful in rural areas/isolated areas, military operations at challenging geography or even for rescue operation.

References:

1. S. Chu and A. Majumdar, *Nature*, 2012, **488**, 294–303.
2. R. del Olmo, T. C. Mendes, M. Forsyth and N. Casado, *J. Mater. Chem. A,* 2022,**10**, 19777-19786
3. P. R. Chinnam, B. Fall, D. A. Dikin, A. A. Jalil, C. R. Hamilton, S. L. Wunder and M. J. Zdilla, *Angew. Chemie - Int. Ed.*, 2016, **55**, 15254–15257.
4. M. Miroshnikov, K. Mahankali, N. K. Thangavel, S. Satapathy, L. M. R. Arava, P. M. Ajayan and G. John, *ChemSusChem*, 2020, **13**, 2186–2204.
5. D. M. Fabian, S. Hu, N. Singh, F. A. Houle, T. Hisatomi, K. Domen, F. E. Osterloh and S. Ardo, *Energy Environ. Sci.*, 2015, **8**, 2825–2850.
6. D. Tripathy, V. H. M, H. Makri Nimbegondi Kotresh, P. V. Babu and S. Sampath, *ACS Appl. Mater. Interfaces*, 2022, **14**, 26671−26681.
7. D. Perry and M. Mamlouk, *J. Power Sources*, 2021, **514**, 230577.
8. K. M. K. Yu, I. Curcic, J. Gabriel and S. C. E. Tsang, *ChemSusChem*, 2008, **1**, 893–899.
9. R. Cauwenbergh and S. Das, *Green Chem.*, 2021, **23**, 2553–2574

10. D. N. Rainer, A. V. Desai, A. R. Armstrong and R. E. Morris, *J. Mater. Chem. A*, 2021, **9**, 27361–27369.
11. Z. Liang and Y. C. Lu, *Batter. Supercaps*, 2021, **4**, 1588–1598.
12. F. Lorandi, T. Liu, M. Fantin, J. Manser, A. Al-Obeidi, M. Zimmerman, K. Matyjaszewski and J. F. Whitacre, *iScience*, 2021, **24**, 102578.
13. S. Li, F. Lorandi, H. Wang, T. Liu, J. F. Whitacre and K. Matyjaszewski, Prog. *Polym. Sci.*, 2021, **122**, 101453.
14. L. Schafzahl, N. Mahne, B. Schafzahl, M. Wilkening, C. Slugovc, S. M. Borisov and S. A. Freunberger, *Angew. Chemie - Int. Ed.*, 2017, **56**, 15728–15732.
15. E. Mourad, L. Coustan, P. Lannelongue, D. Zigah, A. Mehdi, A. Vioux, S. A. Freunberger, F. Favier and O. Fontaine, *Nat. Mater.*, 2017, **16**, 446–454.
16. P. Cai, J. Huang, J. Chen and Z. Wen, *Angew. Chemie - Int. Ed.*, 2017, **56**, 4858–4861.
17. T. Pacześniak, K. Rydel-Ciszek, P. Chmielarz, M. Charczuk and A. Sobkowiak, *J. Chem. Educ.*, 2018, **95**, 1794–1800.
18. J. Masa, P. Weide, D. Peeters, I. Sinev, W. Xia, Z. Sun, C. Somsen, M. Muhler and W. Schuhmann, *Adv. Energy Mater.*, 2016, **6**, 1–10.
19. R. Ding, T. Yan, Y. Wang, Y. Long and G. Fan, *Green Chem.,* 2021, **23**, 4551–4559
20. J. Durst, C. Simon, F. Hasché and H. A. Gasteiger, *J. Electrochem. Soc.*, 2015, **162**, F190–F203.
21. T. N. Huan, R. T. Jane, A. Benayad, L. Guetaz, P. D. Tran and V. Artero, *Energy Environ. Sci.*, 2016, **9**, 940–947.
22. M. Nesselberger, M. Roefzaad, R. Fayçal Hamou, P. Ulrich Biedermann, F. F. Schweinberger, S. Kunz, K. Schloegl, G. K. H. Wiberg, S. Ashton, U. Heiz, K. J. J. Mayrhofer and M. Arenz, *Nat. Mater.*, 2013, **12**, 919–924.
23. K. Shinozaki, J. W. Zack, S. Pylypenko, R. M. Richards, B. S. Pivovar and S. S. Kocha, *Int. J. Hydrogen Energy*, 2015, **40**, 16820–16830.
24. M. Quan, D. Sanchez, M. F. Wasylkiw and D. K. Smith, *J. Am. Chem. Soc.*, 2007, **129**, 12847–12856.
25. Y. Liang, Y. Jing, S. Gheytani, K. Y. Lee, P. Liu, A. Facchetti and Y. Yao, *Nat. Mater.*, 2017, **16**, 841–848.

26. N. Christudas Dargily, R. Thimmappa, Z. Manzoor Bhat, M. C. Devendrachari, A. R. Kottaichamy, M. Gautam, S. P. Shafi and M. O. Thotiyl, *J. Phys. Chem. Lett.*, 2018, **9**, 2492–2497.
27. K. Lin, Q. Chen, M. R. Gerhardt, L. Tong, S. B. Kim, L. Eisenach, A. W. Valle, D. Hardee, R. G. Gordon, M. J. Aziz and M. P. Marshak, *Science*, 2015, **349**, 1529–1532.
28. M. Sevilla and R. Mokaya, *Energy Environ. Sci.*, 2014, **7**, 1250–1280.
29. M. Liu, Z. Zhao, X. Duan and Y. Huang, *Adv. Mater.*, 2019, **31**, 1–8.
30. Y. J. Wang, W. Long, L. Wang, R. Yuan, A. Ignaszak, B. Fang and D. P. Wilkinson, *Energy Environ. Sci.*, 2018, **11**, 258–275.
31. C. W. Anson and S. S. Stahl, *Chem. Rev.*, 2020, **120**, 3749–3786.

Chapter 5:

An all Solid State Proton Battery

Abstract: The lighter molar mass and smaller size of protons can be harnessed for developing higher rate batteries by negating the threat of volume expansion during the discharge and charge chemistry. These advantages can be exploited only if the entire battery chemistry is based on protons. This chapter deals with a rechargeable and an all solid state proton battery by harnessing the redox energy difference associated with the proton insertion in transition metal oxides and hydrogen storing organic molecules. Battery chemistry involves a crystal symmetry alteration commensurate with proton insertion via a phase transformation to a higher crystalline symmetry cubic structure in the negative electrode. This battery concept based on protons allows the coupling of hydrogen storage and utilization in single device thereby facilitating a sustainable energy landscape.

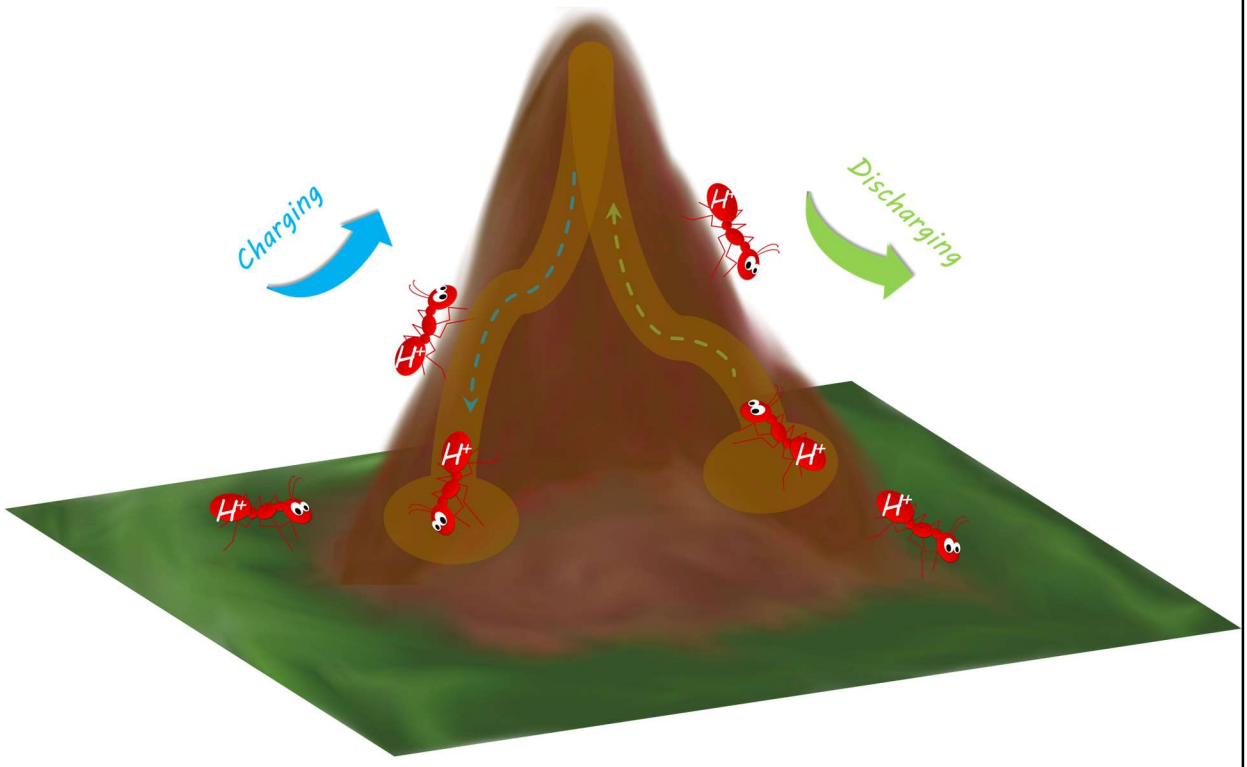

Introduction

The existence of life on earth is challenged due to the excessive deterioration of the environment due to paramount pollution and global warming which are majorly associated with the indiscriminate usage of fossil fuels[1]. As per the sixth intergovernmental panel on climate change (IPCC) reports of 2021, the carbon budget to limit the rise of global temperature by 2 degrees will be moribund by 2045 [2]. This mandates the shift to an alternate but sustainable energy economy hinging on renewable energy resources. Out of the possible options, hydrogen economy which refers to the use of hydrogen as a low-carbon energy source; becomes the cornerstone that can be relied upon[3,4]. However, the implementation of a robust hydrogen economy is derailed by the inefficacy of implementing its key steps such as hydrogen production, hydrogen storage and hydrogen utilization [3,4].

This chapter demonstrate a battery concept where hydrogen storage and its utilization is coupled in the same device by reversible electrochemical proton insertion in transition metal oxides and small organic molecules (Scheme 5.1). This is enabled by the positive potential difference between the proton insertion in tungsten based metal oxides and quinone based small organic molecules. The high theoretical capacity of hydrogen (120 MJ/kg), and its smaller ionic size make it an excellent species for charge storage/transfer[5]. Being a constituent element of water, the ability of protons for hydrogen bonding makes its transport unique as it can hop between water molecules alike Newton's cradle[6], which in turn eventually makes the proton a potential candidate for energy storage/conversion applications[7]. For aforementioned reasons, the rechargeable proton battery we have developed demonstrated a capacity of ~300 mAh/g with an extended cyclability of over 200 cycles.

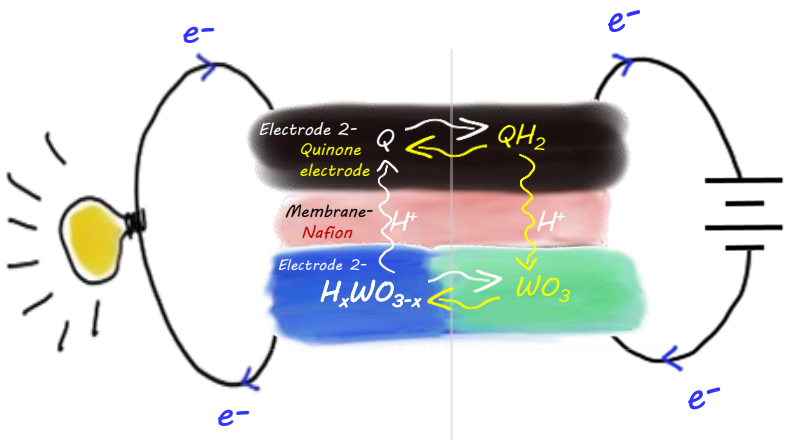

***Scheme 5.1**: Schematic representation of an all solid state proton battery*

Results and discussion:

Electrochemical investigation of reversible proton insertion/deinsertion in oxides of various transition metals such as Co, Mn, V, Mo, Ti and W was conducted by cyclic voltammetric investigation (Figure 5.1a-h) to identify the suitable anode material which can undergo reversible proton insertion/deinsertion at potentials close to hydrogen redox reactions. Out of the screened materials, WO_3 showed reversible electrochemical proton intercalation/de-intercalation behavior at a potential close to hydrogen redox reaction (Figure 5.1h). All other materials were either not sufficiently active towards proton intercalation/de-intercalation, or catalyzed hydrogen evolution reactions. Thus, WO_3 is chosen for further electrochemical and physico chemical analyses.

FESEM images (Figure 5.2a,b) of WO_3 revealed a uniform circular disc-shaped morphology with a diameter of ~100 nm. HRTEM image confirms the disc-shaped morphology of WO_3 (Figure 5.1c), and the associated SAED pattern (Figure 5.2d) reveals the material to be monocrystalline, with a d spacing of ~2.5 A° (Figure 5.2e). Further, the elemental mapping (Figure 5.2f) proves W (green) and O (red) as the constituent elements. UV-Vis spectrum (Figure 5.2g) of the WO_3 exhibits an absorption peak at ~300 nm and the associated Tauc plot (Figure 5.2g, inset) shows a band gap close to 2.5 eV. The mott-schottky (Figure 5.2h) analysis reveals the material to be an n-type semiconductor with its positive slope along with a flat band potential close to 0.4 V vs. RHE. The powder X-ray diffraction (XRD) pattern (Figure 5.2i) readily indexed to the monoclinic WO_3 phase with lattice parameters of a = 7.3 Å, b = 7.53 Å, c = 7.68 Å and β= 90.90° that correspond to JCPDS-01-72-1465, indicating a crystalline and a phase-pure WO_3.

Cyclic voltammograms (CV) of WO_3 exhibit a negative potential relative to quinone redox reactions. The two reduction peaks displayed in WO_3 correspond to the conversion $W^{6+} \rightarrow W^{5+}$/$W^{5+} \rightarrow W^{4+}$ and the processes are reversed upon the oxidation (Figure 5.3a). (as per in-situ electrochemical FTIR studies, see the detailed discussion below). The electrochemically active surface area (ECSA) was estimated to be 4.5 m^2/g, by utilizing the equation 2.2 (Figure 5.3b. The log i vs. log u plot (Figure 5.3c) analysis of cyclic voltammograms (Figure 5.3a) of WO_3 demonstrated a slope of ~0.7, indicating the involvement of mixed surface capacitive/diffusion-controlled insertion processes during the electrochemical redox reactions. The impedance spectroscopic analysis of WO_3 also confirms a diffusion-controlled process with its long Warburg tail (Figure 5.3d) persistent even at lower frequencies. The total current was decoupled to its components the surface capacitive and the diffusion-controlled insertion processes with equation 2.4. The analysis

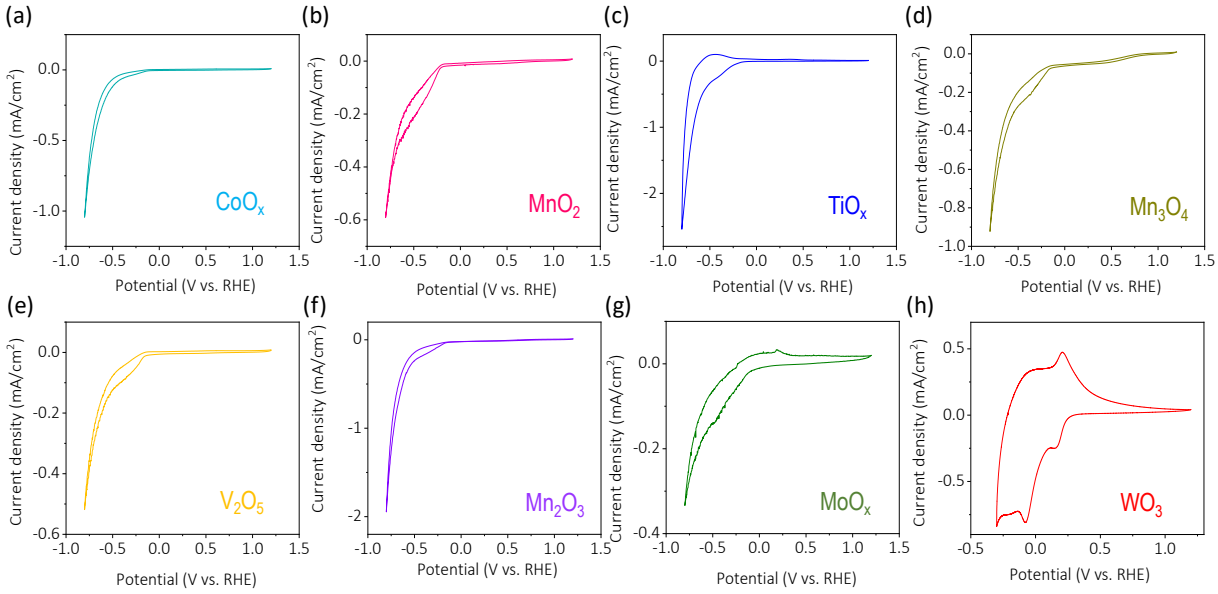

***Figure 5.1**: Cyclic voltammogram of various transition metal oxides in 0.5M H_2SO_4 at scan rate of 10mV/s*

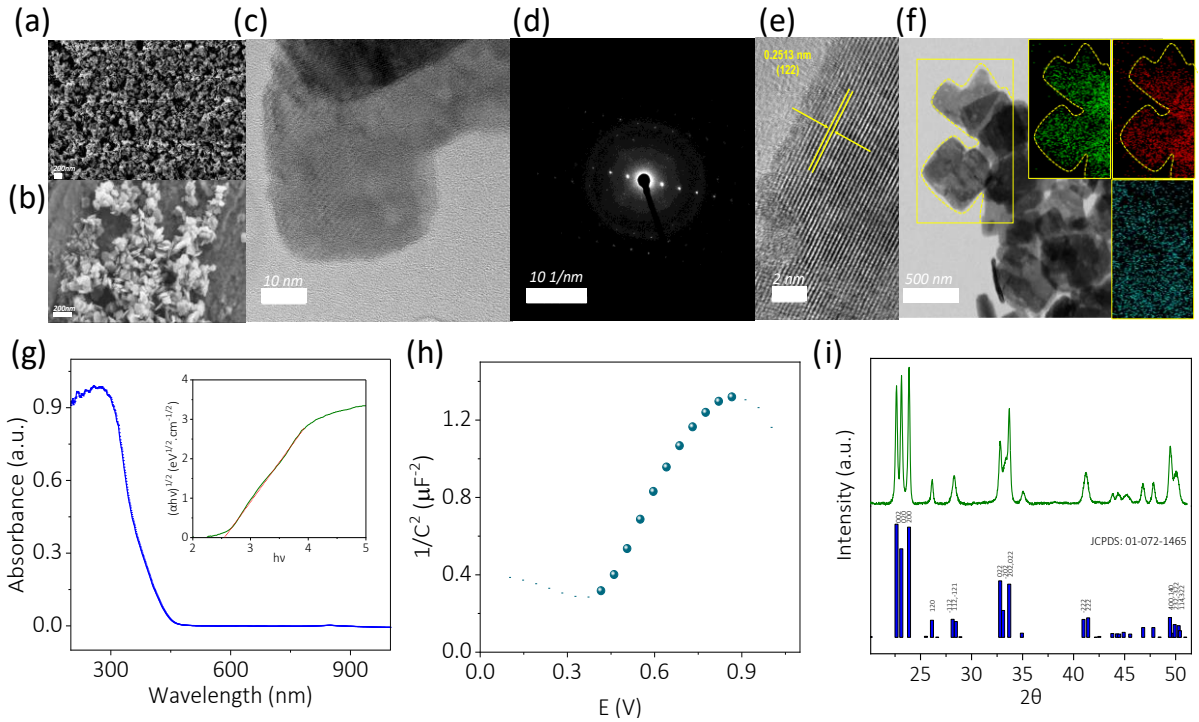

***Figure 5.2**: FESEM images of WO_3 (a,b). (c-f) HRTEM analysis WO_3. (c) High resolution TEM image of WO_3, (d) associated selected area electron diffraction (SAED) data, (e) HRTEM image with the d-spacing and (f) corresponding elemental mapping for tungsten (green), oxygen (red) and carbon (blue). (g) UV-vis spectra (inset: associated tauc plot),(h) mott-shotky analysis plot (i) XRD of WO_3.*

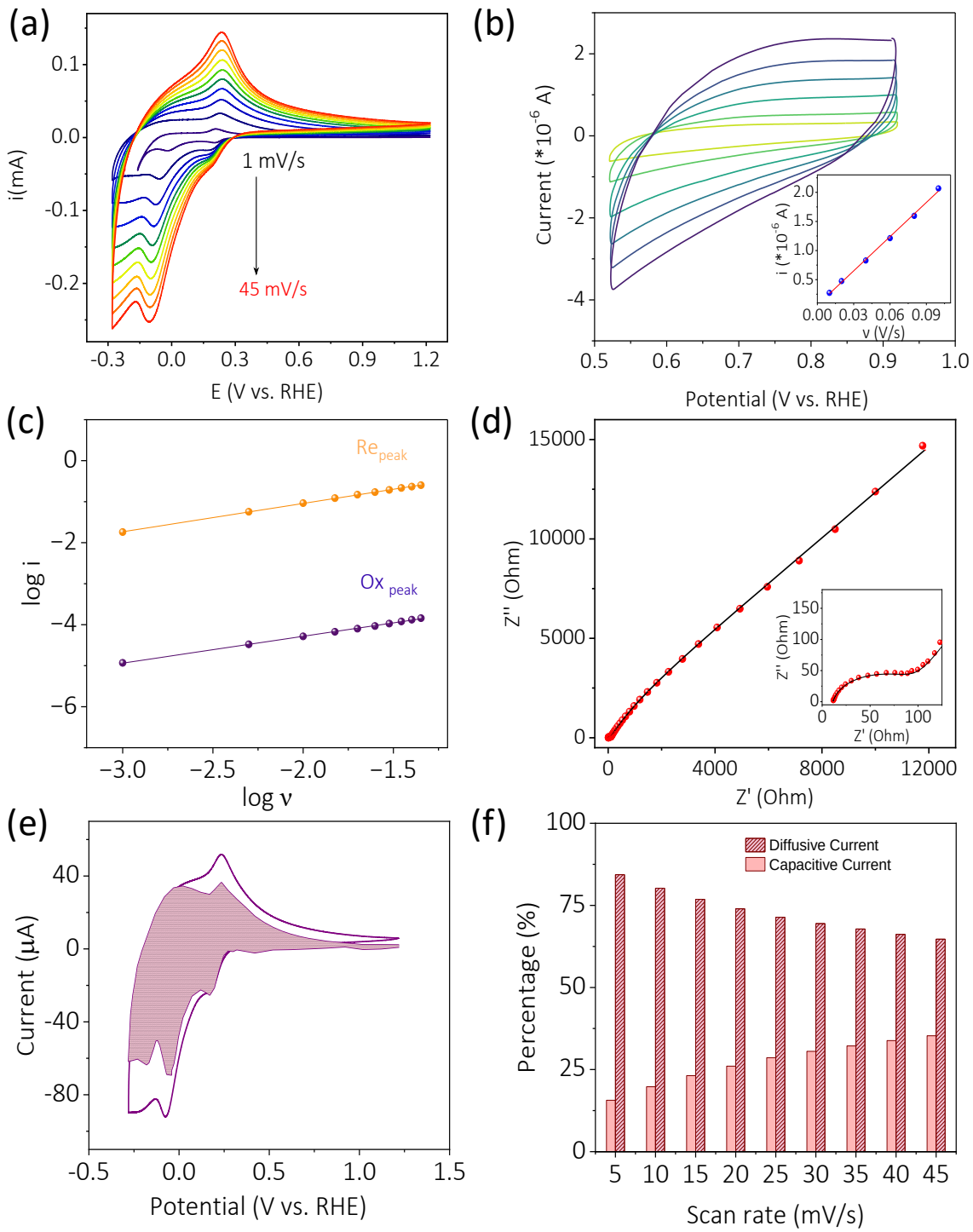

Figure 5.3: *a) Cyclic voltammogram of WO_3 in 0.5M H_2SO_4 at varying scan rates. Electrochemical active surface area from double layer (b) Cyclic voltammogram of WO_3 at different scan rate (inset: Current vs. scanrate plot.) (c) log i vs log u plot of oxidation (violet trace) and reduction (orange trace) respectively. (d) Impedance spectra of WO_3 at 60mV vs RHE. (e) Cyclic voltammograms of WO_3 in 0.5 M H_2SO_4 at a scan rate of 10 mV/s and the corresponding current contribution due to capacitive (non-shaded region) and diffusional (shaded region) components. (f) Percentage contribution of surface capacitive and diffusion-controlled insertion process to the total current of WO_3 electrode at varying scan rates.*

discloses the dominant contribution of diffusion-controlled insertion processes at all studied scan rates (Figure 5.3e,f). At a scan rate of 5 mV/s, the contribution from the diffusion-controlled insertion process is as high as ~85 %. Given the fact that ESCA is 4.5 m^2/g which is fairly high, WO_3 still promotes its redox reaction via a dominant diffusion-controlled insertion process, indicating the efficient utilization of the bulk of the material. This testifies that the WO_3 possesses potential features to be used as a promising H^+ storing negative electrodes.

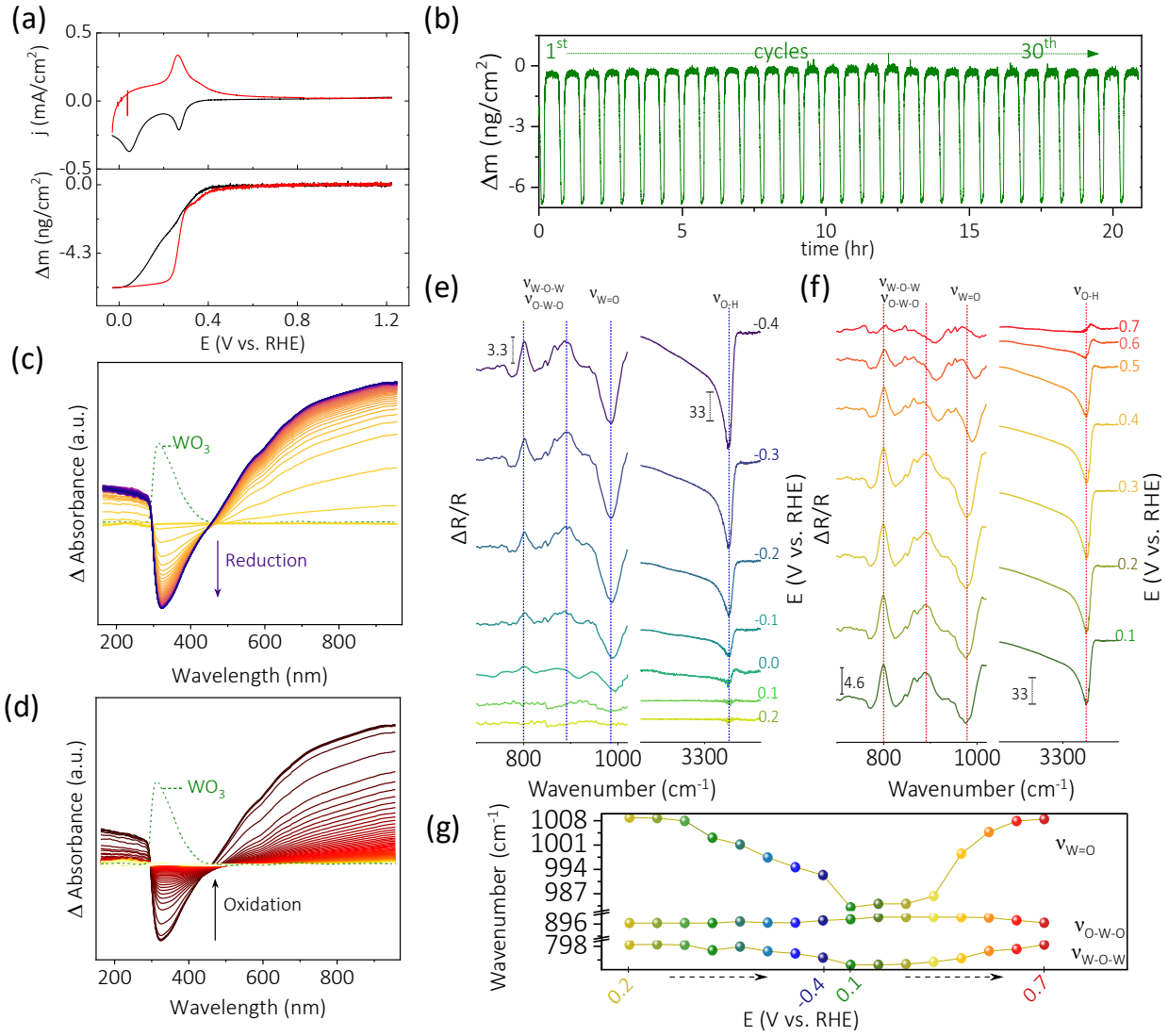

Figure 5.4: *In-situ electrochemical QCM studies of WO_3 electrode. (a) Cyclic voltammogram (top panel) of WO_3 electrode in 0.5 M H_2SO_4 at a scan rate of 1 mV/s with the corresponding mass change (bottom panel). (b) Mass change during extended cycling. Insitu-UV-Vis spectroelectrochemistry during reduction (c) and oxidation (d) respectively. Potential dependent relative reflectance in-situ electrochemical FTIR response of WO_3 electrode in 0.5 M H_2SO_4 during (e) reduction and (f) oxidation. (g) Potential dependent wavenumber shift (cm^{-1}) corresponding to P_1($\upsilon_{W\text{-}O\text{-}W}$, $\upsilon_{O\text{-}W\text{-}O}$), P_2 ($\upsilon_{W\text{-}O\text{-}W}$, $\upsilon_{O\text{-}W\text{-}O}$) and P_3 ($\upsilon_{W=O}$).*

Electrochemical Quartz Crystal Microbalance (EQCM) was further employed to understand the proton insertion/de-insertion during electrochemical cycling. The change in frequency (Δf, Hz) during the electrochemical cycling was monitored, and the change in mass (Δm, ng) was calculated by utilizing the Saurbey equation (equation 2.8) [8]. EQCM studies of the thin film of WO_3 on a gold crystal (f_0 =8.000 MHz) were carried out at 1 mV/s in 0.5 M H_2SO_4 (Figure 5.4a). On reduction (black trace, (Figure 5.4a) WO_3 did exhibit a decrease in mass, and a reversal upon oxidation (red trace, Figure 5.4a). The negative mass change observed on electrochemical reduction is due to the diffusive intercalation of protons with the expulsion of water molecules which is regained upon oxidative scan[9]. The long-term cycling for 30 cycles of WO_3 did not demonstrate signs of irreversibility in terms of reactivity/material loss, (Figure 5.4b). Therefore, EQCM studies of WO_3 deciphered the efficient intercalation/de-intercalation of protons in WO_3, its stability, and reversibility.

Electrochemical reversibility and stability at the electrode-electrolyte interface of WO_3 were then studied by in-situ-UV-Vis spectroelectrochemistry. In its UV-Vis spectrum, WO_3 displayed a pale green color corresponding to a single peak at ~313 nm. During the reduction scan (0.4 V vs RHE), in-situ-UV-Vis spectroelectrochemistry of WO_3 utilizing equation 2.7 (Figure 5.4c) revealed, the depletion of the signature peak at ~313 nm with the simultaneous appearance of a broad band in the near-IR regime. The near-IR broadband is responsible for its strong blue coloration which is attributed to the polaron, that occurred with the existence of multivalent reduced oxidation states such as W^{5+} and W^{4+} in the crystal lattice [10–12]. On applying the oxidation potential (1 V vs. RHE), the absolute reversal of the features as well as the recovery of its pale green colour, validates the complete transformation to a single oxidation state of W^{6+}, (Figure 5.4d). Hence, in-situ-UV-Vis spectroelectrochemistry of WO_3 confirms the conversion of $W^{6+} \rightarrow W^{5+} \rightarrow W^{4+}$, back and forth during reductive and oxidative scans.

The factors responsible for proton insertion/de-insertion in WO_3 during electrochemical reduction/oxidation were then monitored using in-situ electrochemical FTIR spectroscopy (Figure 2.1, Chapter 2) The differential spectrum (relative reflectance: equation 2.9 obtained during the course of the experiment, witnessed modifications in intensity and peak positions. The relative reflectance (ΔR/R) provides sensitivity as low as 1%, and a positive peak indicates the diminishing nature of the species and vice versa[13]. The region below 1200 cm^{-1} in the FTIR spectra of metallic oxides, belongs to signatures features for M=O, M-O-M, O-M-O [12,14,15]. The three peaks observed at ~798 cm^{-1} ($\upsilon_{W\text{-}O\text{-}W}$, $\upsilon_{O\text{-}W\text{-}O}$), ~896 cm^{-1} ($\upsilon_{W\text{-}O\text{-}W}$, $\upsilon_{O\text{-}W\text{-}O}$), and ~1008 cm^{-1} ($\upsilon_{W=O}$) belong to metal oxide, and one peak at nearly 3608 cm^{-1} corresponds to $\upsilon_{O\text{-}H}$ and these peaks are respectively labeled as P_1, P_2, P_3 and P_4 (Figure 5.4e-g). During the electrochemical

reduction at potentials ranging from 0.2 to -0.4 V vs RHE (Figure 5.4e) P_1 and P_2 were consumed with a concomitant growth in peaks P_3 and P_4. Commensurately, P_3 exhibited a red shift by ~25 cm^{-1} (Figure 5.4g). These features were reversed upon oxidative scan (0.1 to 0.7 V vs RHE) (Figure 5.4f,g) This validates, that on electrochemical reduction of WO_3, the conversion of $W^{6+} \rightarrow W^{5+}/W^{5+} \rightarrow W^{4+}$ promotes the breakage of bridged W-O-W, and O-W-O bonds to form W=O and O-H. The bond weakening is indicated by the redshift of the W=O bond by ~25 cm^{-1} which can be attributed to the interaction/bond formation between the inserted protons and the double bonded oxygen. This argument is further supported by the increase in O-H intensity near 3608 cm^{-1} during the reductive scan. Therefore, during the electrochemical reduction of WO_3, the inserted proton is stabilized by the interaction with double-bonded oxygen of the W=O formed from the breakage W-O-W/O-W-O bonds. All these modifications were revoked to their initial state on electrochemical oxidation, indicating the reversibility/stability of the material during electrochemical cycling.

Having established the suitability of WO_3 as the anode material, the prospects of quinone as the positive electrode for the rechargeable proton battery, via reversible electrochemical hydrogenation/dehydrogenation is discussed in detail in Chapter 3: Figure 3.1- 3.3, Table 3.1. All these conditions favor the utility of the Q/QH_2 redox couple for the proposed all solid state proton battery.

A two-electrode split cell device was constructed by coupling WO_3 with a quinone electrode through a proton-conducting Nafion 117 membrane, Figure 5.5a (Figure 2.4, Chapter 2). The battery cyclic voltammograms (Figure 5.5b) with quinone as the working electrode demonstrated electrochemically reversible hydrogenation/dehydrogenation behaviour at a positive potential with respect to WO_3. This confirms that the former functions as a positive electrode and later as a negative electrode. Charge discharge chemistry as a function of rate, Figure 5.5b demonstrates decent performance while retaining 60% of its theoretical capacity. Battery demonstrated an extended cyclability of 200 cycles at 0.5 mA, with a capacity retention of 94% compared to the first cycle Figure 5.5c. The calculated efficiencies further attest the performance metrics of the battery with columbic, voltage, and energy efficiency of 90 %, 86 %, and 77 % respectively Figure 5.5d.

In order to prove the back-and-forth proton movement during charge-discharge chemistry in the assembled device, we carried out in-situ Raman spectroelectrochemistry in the battery mode with WO_3 as the working electrode and quinone electrode as the counter and reference electrode. The cell setup is shown in Figure 2.2 (Chapter 2). In-situ electrochemical Raman spectroscopy was carried out by exposing the WO_3 electrode to the laser via transiting it through a quartz window, and the spectra were obtained at regular

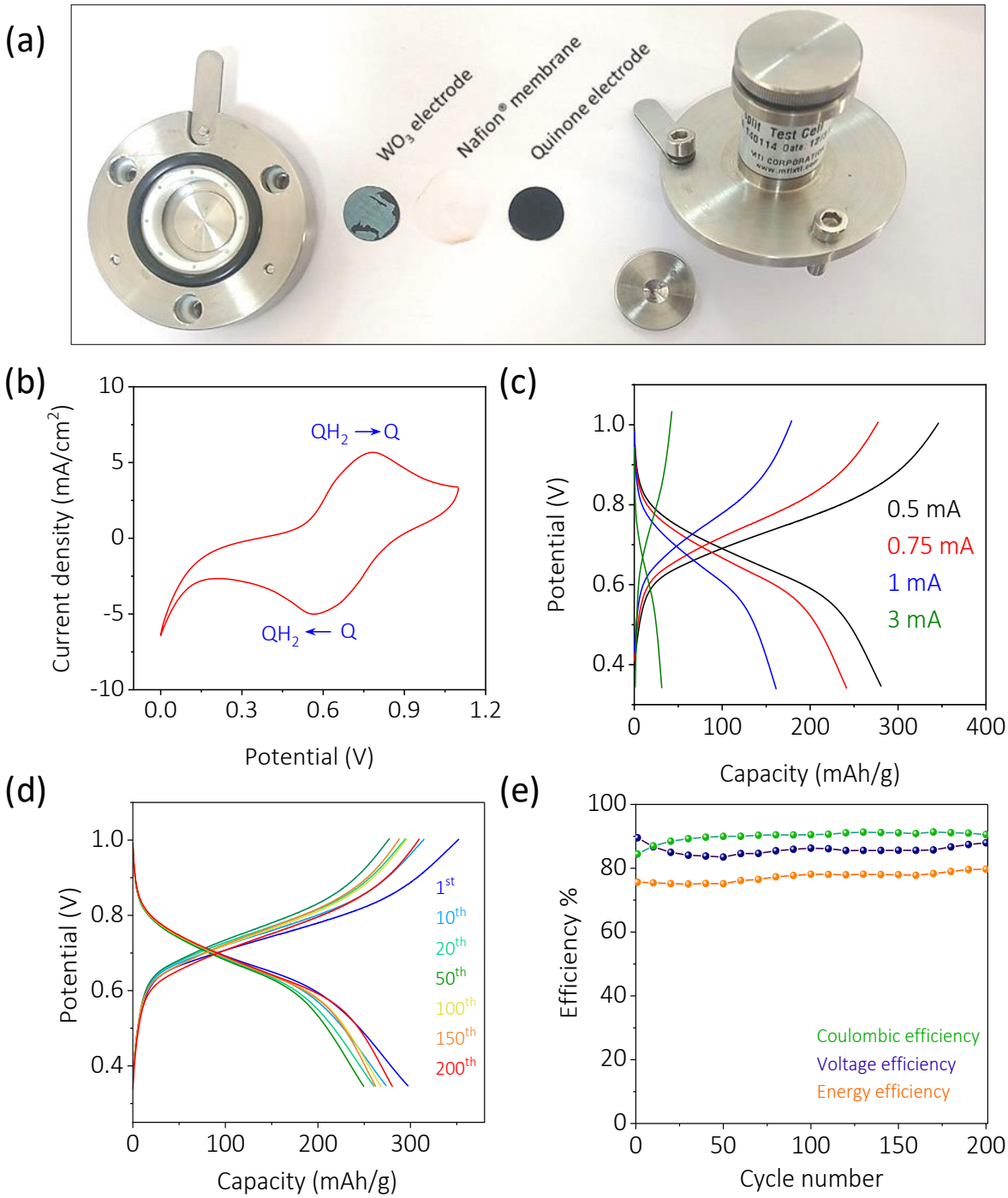

***Figure 5.5**: (a) Photograph of the components utilized for battery fabrication in a split cell assembly. (b) Cyclic voltammetric response of battery cathode in a two-electrode split cell assembly. (c) The rate capability of the battery. (d) Long-term cycling of the battery at a current of 0.5 mA for 200 cycles. (e) Columbic, voltage, and energy efficiency of battery for 200 cycles.*

intervals during the charging and discharging of the battery (Figure 5.6a). WO_3 as such demonstrates three major peaks at ~800.7, ~708.7, and ~266.2 cm^{-1} corresponding to stretching of short O-W-O, long O-W-O,

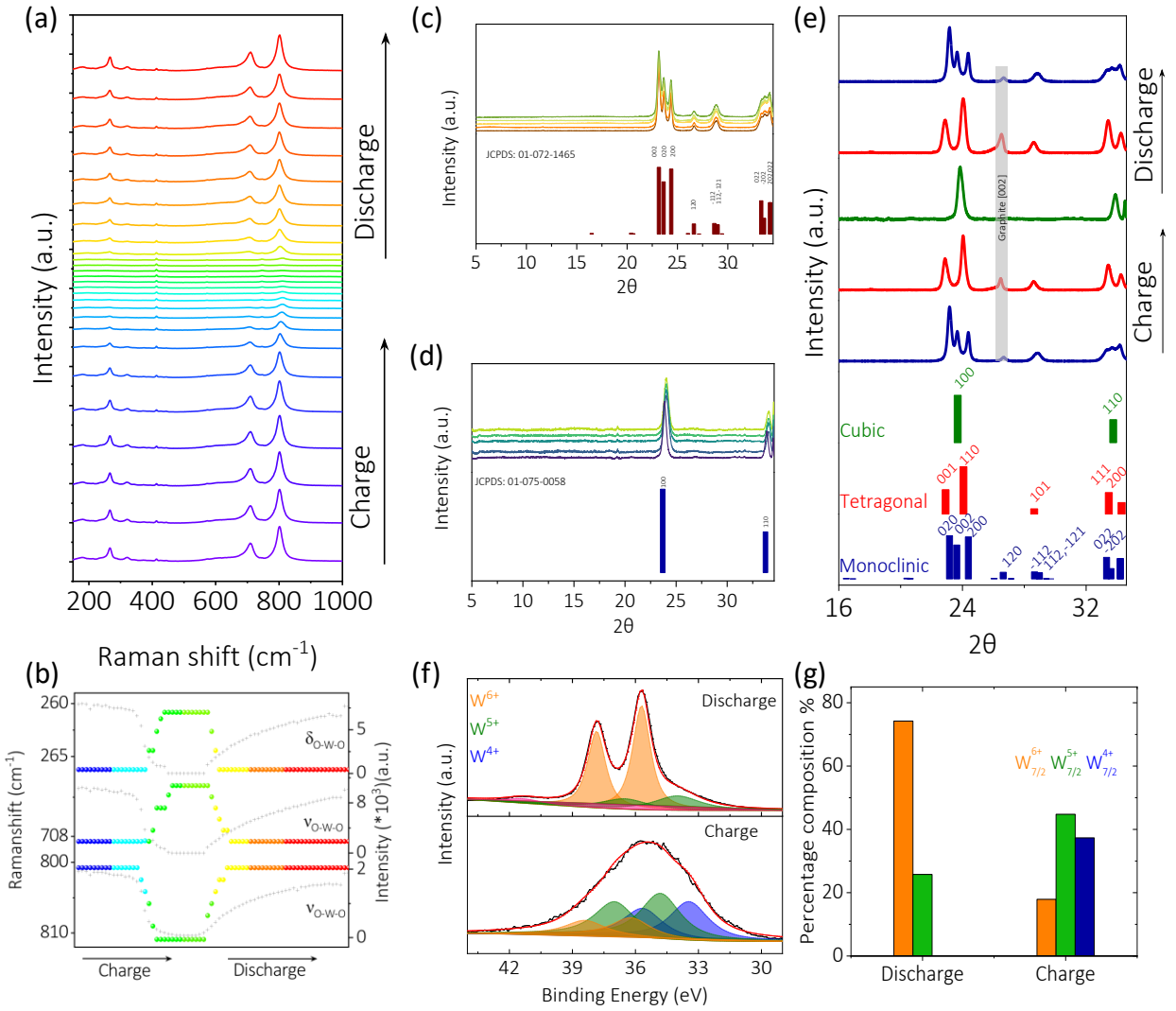

Figure 5.6: *In-situ Raman electrochemical spectroscopy of WO_3 electrode in the battery configuration. (a) Potential dependent spectra and (b) alterations in the peak positions (left axis) and intensity (grey trace, right axis) during charging and discharging. XRD analysis of WO_3 anode on complete (c) discharge (d) charge during multiple battery cycles. XRD analysis of WO_3 anode at (e) different states of charge (SOC) during charging and discharging, 0 % SOC (blue trace), 100% SOC (green trace), and intermediate SOC (red trace). (f) XPS spectra and (g) percentage composition of different oxidation states of tungsten during charging and discharging.*

and bending of O-W-O respectively[14,16]. Firstly, no new peaks/bands appear that do not belong to WO_3 during the charge/discharge process, indicating the absence of any newly generated inter-phases or species. Secondly, the aforementioned three major peaks shifted to ~810, ~700, and ~260 cm^{-1} respectively (Figure 5.6a,b, coloured trace) during the charge chemistry. As the peak value is the measure of bond strength, the peak shift can be attributed to the variation in the bond strength, brought by changes in bond lengths during the reaction. The blue shift of ~708.7, and ~266.2 cm^{-1} bands along with the red shift of the band at ~800.7

cm^{-1} indicate modification of W−O bond length and thereby bond strength. It is to be noted that all these features regained their initial state during the discharge chemistry. Thirdly, the intensity of all the major peaks diminished on charging and regained upon discharging (Figure 5.6a,b, black trace). Since the intensity of the Raman scattered radiation $I_r \alpha \nu^4.I_o.N.[d\alpha/dQ]$ (where ν is the frequency of the exciting laser, I_o is the incident laser intensity, N is the number of scattering molecules in a given state, α is the polarizability of the molecules, and Q is the vibrational amplitude),[9] and a change in intensity is expected only for a change in $[d\alpha/dQ]$ once the in-situ cell is setup; the difference in the intensity is attributed to the change in polarizability, that in turn can be triggered by the evolution of symmetry elements. This states that the increased electron density in the lattice of WO_3 during the charge chemistry would alter the W−O bond, distorting WO_6 octahedra, and thereby phase transformation to a higher - symmetry structure [17]. Therefore, the battery charge/discharge is assisted by the alteration of bridged W-O-W/O-W-Obonds via a change in bond length and bond strength which concomitantly affect the crystal symmetry. This transformation of the crystalline phase in the WO_3 electrode during battery charge/discharge is clear from ex-situ-XRD analysis (Figure 5.6c-e). The WO_3 electrode in its discharged state demonstrates a monoclinic phase (similar to its material nature, Figure 5.6c), however, the charged battery electrodes exhibited a cubic phase (Figure 5.6d). The XRD analysis of battery electrodes at various states of charge (SOC) evidenced the alteration to a higher crystalline symmetry, proceeding with the transformation of WO_3 in the monoclinic phase (JCPDS: 01-072-1465) to cubic phase (JCPDS: 01-075-0058) through a tetragonal phase (JCPDS: 01-085-0967), (Figure 5.6e). This is accompanied by the formation of hydrogen tungsten bronze (H_xWO_{3-x}) with the proportionate increase of stoichiometric protons in H_xWO_3 with x ranging from 0 → 0.23 → 0.5 respectively in the case of monoclinic, tetragonal and cubic phases. The crystalline phase was reversed from cubic → tetragonal → monoclinic with the proton de-insertion on battery discharge (Figure 5.6e) and hence the anode transforms to a variable crystalline phase depending on the SOC. In summary, the completely discharged state is in the monoclinic phase (0% SOC) and the completely charged state is in the cubic phase (100% SOC) with an intermediately charged state exhibiting a tetragonal phase. The XRD analysis of the anode not only affirms the protonation/deprotonation but also an evolution in the crystal symmetry during the protonation/deprotonation. This analysis affirms that, for maximum proton insertion/deinsertion, a higher symmetry cubic phase is vital. Individual composition of different oxidation states of tungsten in the battery electrodes during battery charge/discharge was further monitored by X-ray photoelectron spectroscopy (XPS). The raw spectrum of the discharged electrode resembled pristine WO_3 with 2 peaks, however, charged electrodes demonstrated an overlapping spectrum. On deconvolution, the W_{4f} regime of the charged battery electrode revealed an

increase in electron density in the lattice of WO_3 with a higher composition of the reduced W species (W^{5+}, W^{4+}) relative to that of the oxidized W species (W^{6+}) and its reversal during the battery discharge (Figure 5.6f,g). In summary, in-situ Raman spectroelectrochemistry, XRD, and XPS analyses in the battery mode suggest, altering the electron density in the lattice of WO_3, crystalline phase/symmetry transformation, and modification of O−W−O bond commensurate with reversible proton insertion/deinsertion.

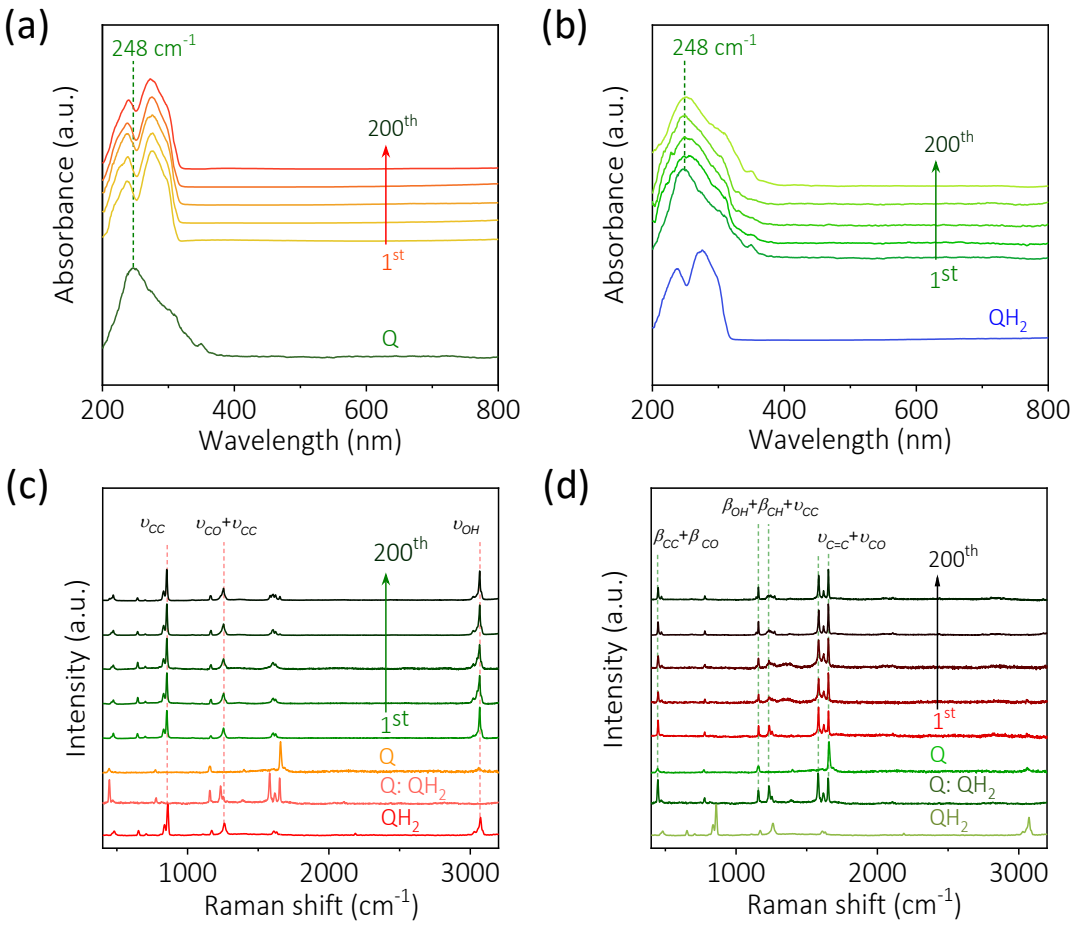

***Figure 5.7**: UV-Vis spectroscopy of (a) discharged and (b) charged battery cathodes. Raman spectra of (c) discharged and (d) charged battery cathodes.*

The cathode chemistry in the battery mode was investigated by ex-situ UV-Vis spectroscopy and Raman spectroscopy. The discharged battery electrodes revealed the presence of hydroquinone with two peaks centered at nearly 237 nm and 275 nm in the UV–Vis spectrum, (Figure 5.7a). The charged electrodes demonstrated the features of quinone with a single peak at nearly 248 nm in the UV–Vis spectrum (Figure 5.7b). This supports the hydrogenation/dehydrogenation of quinone while discharging and charging respectively. The Raman spectra (Figure 5.7c) during the discharge also reveal the presence of υ_{O-H} band at ~3066 cm^{-1} that corresponds to the formation of hydroquinone. However, the Raman spectrum showed the

presence of quinhydrone (1:1= quinone: hydroquinone) complex during the charge chemistry which may be due to the reactivity of quinone during the exposure to light and oxygen (Figure 5.7d). Based on all these investigations, the following reactions are proposed for the all-solid-state rechargeable proton battery. On battery discharge, proton inserted tungsten trioxide/tungsten bronze (H_xWO_3) releases the protons and gets oxidized (equation 5.1) resulting in the electrochemical hydrogenation of quinones (equation 5.2). On battery charge, these reactions are reversed.

Anode: $2H_xWO_3 \leftrightarrow 2WO_3 + 2xH^+ + 2xe^-$ (eq. 5.1)

Cathode: $Q + 2xH^+ + 2xe^- \leftrightarrow xQH_2$ (eq. 5.2)

Net cell reaction: $2H_xWO_3 + Q \leftrightarrow 2WO_3 + xQH_2$ (eq. 5.3)

Conclusion:

An all-solid-state proton battery is demonstrated by coupling inorganic and organic hydrogen storage platforms via a proton conducting membrane. The series of investigations including in-situ electrochemical quartz crystal microbalance and FTIR and Raman spectroelectrochemical studies revealed the proton insertion/deinsertion as the dominant mode of charge storage in the inorganic transition metal oxide at a redox potential as close as hydrogen redox. The organic quinone-based molecules demonstrated an electrochemically reversible hydrogenation/dehydrogenation at a relatively positive potential. This rechargeable proton battery configuration combines hydrogen storage and its utilization in a single device and the reversible shuttling of protons leads to a higher rate battery owing to its smaller size and fast diffusion kinetics

References:

1. A. K. Jorgenson, S. Fiske, K. Hubacek, J. Li, T. McGovern, T. Rick, J. B. Schor, W. Solecki, R. York and A. Zycherman, *Wiley Interdiscip. Rev. Clim. Change*, 2019, **10**, 1–17.
2. UNEP, *Climate Change 2023: Synthesis Report | UNEP - UN Environment Programme*, 2023.
3. UNSD & IEA, *Tracking SDG7: The Energy Progress Report 2023*, 2023.
4. P. P. Edwards, V. L. Kuznetsov and W. I. F. David, *Philos. Trans. R. Soc. A Math. Phys. Eng. Sci.*,

2007, **365**, 1043–1056.

5. F. Dawood, M. Anda and G. M. Shafiullah, *Int. J. Hydrogen Energy*, 2020, **45**, 3847–3869.
6. C. Knight and G. A. Voth, *Acc. Chem. Res.*, 2012, **45**, 101–109.
7. T. Xu, D. Wang, Z. Li, Z. Chen, J. Zhang, T. Hu, X. Zhang and L. Shen, *Nano-Micro Lett.*, 2022, **14**, 126.
8. Allen J. Bard and Larry R. Faulkner, *Electrochemical methods : fundamentals and applications*, John Wiley & Sons, Inc., Hoboken, NJ, 2001, Second edition., 2001.
9. M. Yao, P. Wu, S. Cheng, L. Yang, Y. Zhu, M. Wang, H. Luo, B. Wang, D. Ye and M. Liu, *Phys. Chem. Chem. Phys.*, 2017, **19**, 24689–24695.
10. S. Darmawi, S. Burkhardt, T. Leichtweiss, D. A. Weber, S. Wenzel, J. Janek, M. T. Elm and P. J. Klar, *Phys. Chem. Chem. Phys.*, 2015, **17**, 15903–15911.
11. M. F. Saenger, T. Höing, B. W. Robertson, R. B. Billa, T. Hofmann, E. Schubert and M. Schubert, *Physical Review B, 2008,* **78**, 245205
12. T. J. DeJournett and J. B. Spicer, *Sol. Energy Mater. Sol. Cells*, 2014, **120**, 102–108.
13. B. Hofko, M. Z. Alavi, H. Grothe, D. Jones and J. Harvey, *Mater. Struct.*, 2017, **50**, 187.
14. M. F. Daniel, B. Desbat, J. C. Lassegues, B. Gerand and M. Figlarz, *J. Solid State Chem.*, 1987, **67**, 235–247.
15. G. Gao, Z. Zhang, G. Wu and X. Jin, *RSC Adv.*, 2014, **4**, 30300–30307.
16. R. F. Garcia-Sanchez, T. Ahmido, D. Casimir, S. Baliga and P. Misra, *J. Phys. Chem. A*, 2013, **117**, 13825–13831.
17. V. Lokhande, A. Lokhande, G. Namkoong, J. H. Kim and T. Ji, *Results Phys.*, 2019, **12**, 2012–2020.

Chapter 6:

A Rechargeable Atmospheric Water Battery

Abstract: This chapter describes a groundbreaking battery that integrates all three key aspects of the hydrogen economy – hydrogen generation, storage, and utilization – within a single device. To address the primary requirement of hydrogen generation through water electrolysis, a novel approach that eliminates the need for conventional ultrapure water and the requirement transport infrastructure, via harnessing atmospheric water as the water source is adopted. The process of atmospheric water uptake is facilitated by incorporating a hydrophilic Graphene Oxide (GO) membrane into the battery. This membrane exhibits a water uptake capability approximately four times higher than the widely used commercial Nafion membrane. The choice of this membrane as a battery component allows for efficient extraction of water from the surrounding atmosphere. The selected electrodes play a crucial role in the device's functionality. During the battery charging phase, these electrodes exhibit activity in water splitting, generating hydrogen. Conversely, during discharge, the negative electrode not only produces hydrogen but also serves as a storage medium for it. The stored hydrogen is subsequently released during discharge, leading to the generation of electric power. This innovative battery successfully connects the key elements of the hydrogen economy in a single device. It achieves the trifecta of hydrogen economy functionalities: production of hydrogen through atmospheric water splitting, storage of the generated hydrogen, and utilization of hydrogen to generate electric power.

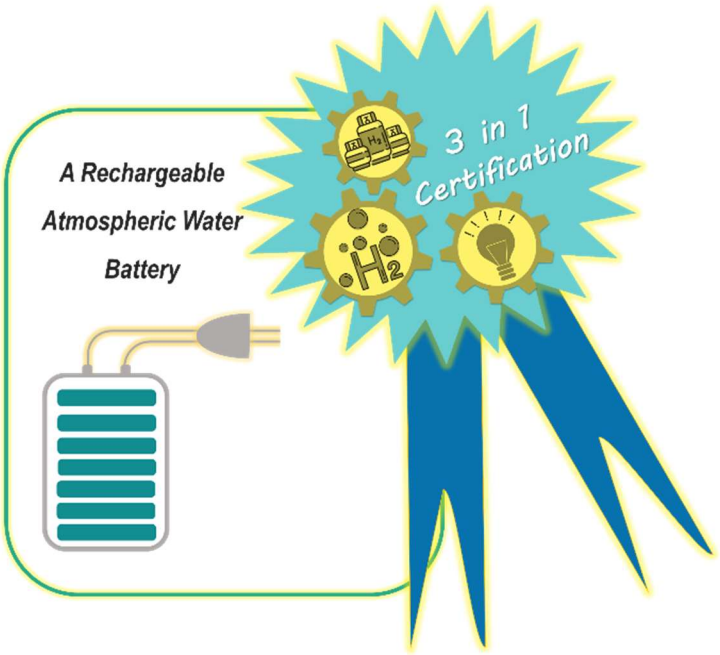

Introduction:

The 200 years of plundered consumption of fossil fuels till date have out-numbered it pros with its serious cons such as pollution, global warming, climate change etc, which in-turn leads to catastrophic environmental imbalance [1–3]. Addressing these, various environment organizations propose a single window exit via switching to an alternative sustainable energy economy focused on net zero emissions [2,4–7]. Due to the prospects of hydrogen economy, which refers to the use of hydrogen as a low carbon energy resource, it is proposed as the corner stone for the proposed sustainable future [8,9]. However, the un-coupled three key steps of hydrogen economy such as production, storage and transport and utilization have been a bottle neck for its implementation[10,11]. The coupling of multisteps in a single device should facilitate this transition. A single device incorporation of all the three facets of hydrogen economy has the potential to overcome the existing technological and engineering challenges associated with hydrogen economy[9,10,12–14].

The rechargeable atmospheric water battery encompasses all the three key steps of hydrogen economy in a single device. It utilizes hygroscopic capability of graphene oxide membranes to uptake atmospheric water and electrocatalytic ability of Pd based electrocatalysts to then split it along with the simultaneous storage of hydrogen. During the discharge chemistry, the stored hydrogen at the negative half-cell is utilized for electricity production with the aid of an air electrode at the positive half-cell. The involvement of protons during charge discharge chemistry at both negative and positive battery interfaces were confirmed by various physicochemical techniques.

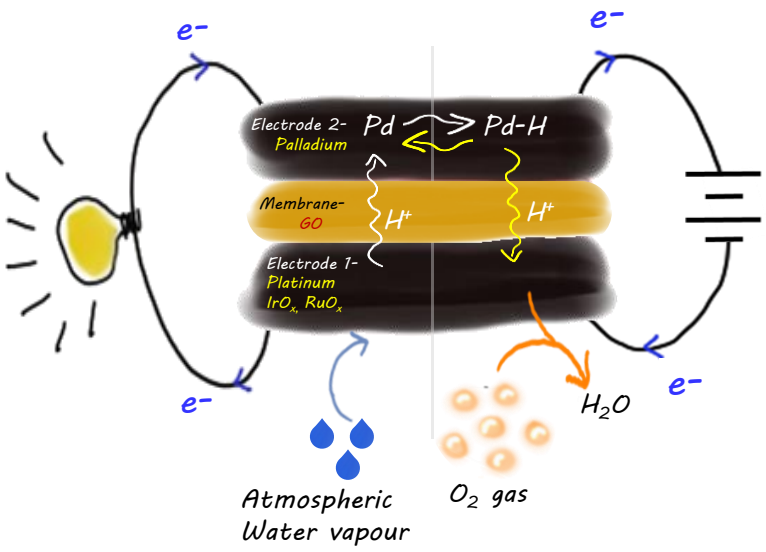

Scheme 6.1*: Schematic representation of battery.*

Results and discussion:

The proposed battery consists of palladium black as the anodic electrocatalyst to facilitate simultaneous water splitting along with hydrogen storage. Its capability for hydrogen oxidation is exploited for the reversible release of stored hydrogen by coupling it with a positive air electrode during the discharge chemistry. The positive electrode was kept open to air with the well-known combination of electrocataysts Pt/IrO_x /RuO_x to maximize the electrocatalytic water splitting during the charge chemistry and reverse during discharge chemistry. The two electrodes are separated by a hygroscopic H^+-ion conducting graphene oxide (GO) membrane to boost the atmospheric water uptake (Scheme 6.1).

Graphene Oxide (GO) was synthesized via modified Hummers method and the as synthesized GO formed sheets which measured a uniform thickness of ~1.6 nm in AFM analysis, indicating multiple layers, Figure 6.1a, b. Further, GO membranes were fabricated having a diameter of 100 mm and a thickness of 0.05 mm via drop-casting the GO suspension on a petridish, Figure 6.1c. The fabricated membranes were characterized with various physio-chemical analysis such as Raman, FTIR, contact angle, XPS, XRD and water dynamic studies. The extent of oxidation of the sp^2 hybridized C=C/graphene with the incorporation of various oxygenated functionality was assessed with the Raman spectra demonstrating an I_D/ I_G value of 2.15 for the synthesized GO material (Figure 6.1d), confirming the successful oxidation of the starting material/ graphite. The FTIR analysis of the membranes attests the embodiment of hydroxyl [O-H], carbonyl [C=O], and epoxide [C-O-C] functionalities at nearly 3200, 1720, 1170 cm^{-1} respectively along with the standard sp^2 hybridized carbon [C=C] at nearly 1615 cm^{-1} (Figure 6.1e). The amount of transformation of the hydrophobic sp^2 hybridized C=C on the graphite to the hydrophilic functional groups during oxidation directly correlates to its hydrophilicity. The contact angle measuring an angle of nearly 58° on the GO validates the hydrophilicity of the membrane (Figure 6.1f, g).

The C1s in the XPS spectra of GO, on deconvolution account for the extent of the modification of the sp^2 hybridized carbon by various functionalities in the ratios of C=C : C−C : C−OH : C−O−C : C=O : O−C=O ≈ 9:10:3:12:1:1 (Figure 6.2a,b). The C−O−C, −OH, and −COOH functional groups are known as proton hopping sites in GO by attracting protons [15,16] and the higher contribution of the same is expected to boost the proton conductivity across the membrane. The XRD analysis of the membrane exhibits the graphitic peak around 2θ of around 10. Further on treating the membrane with varying Relative Humidity (RH%) ranging from 0% (dry) to 95% (wet), the peak was found to downshifted by ≈ 2.6 units (2θ) corresponding to a lattice

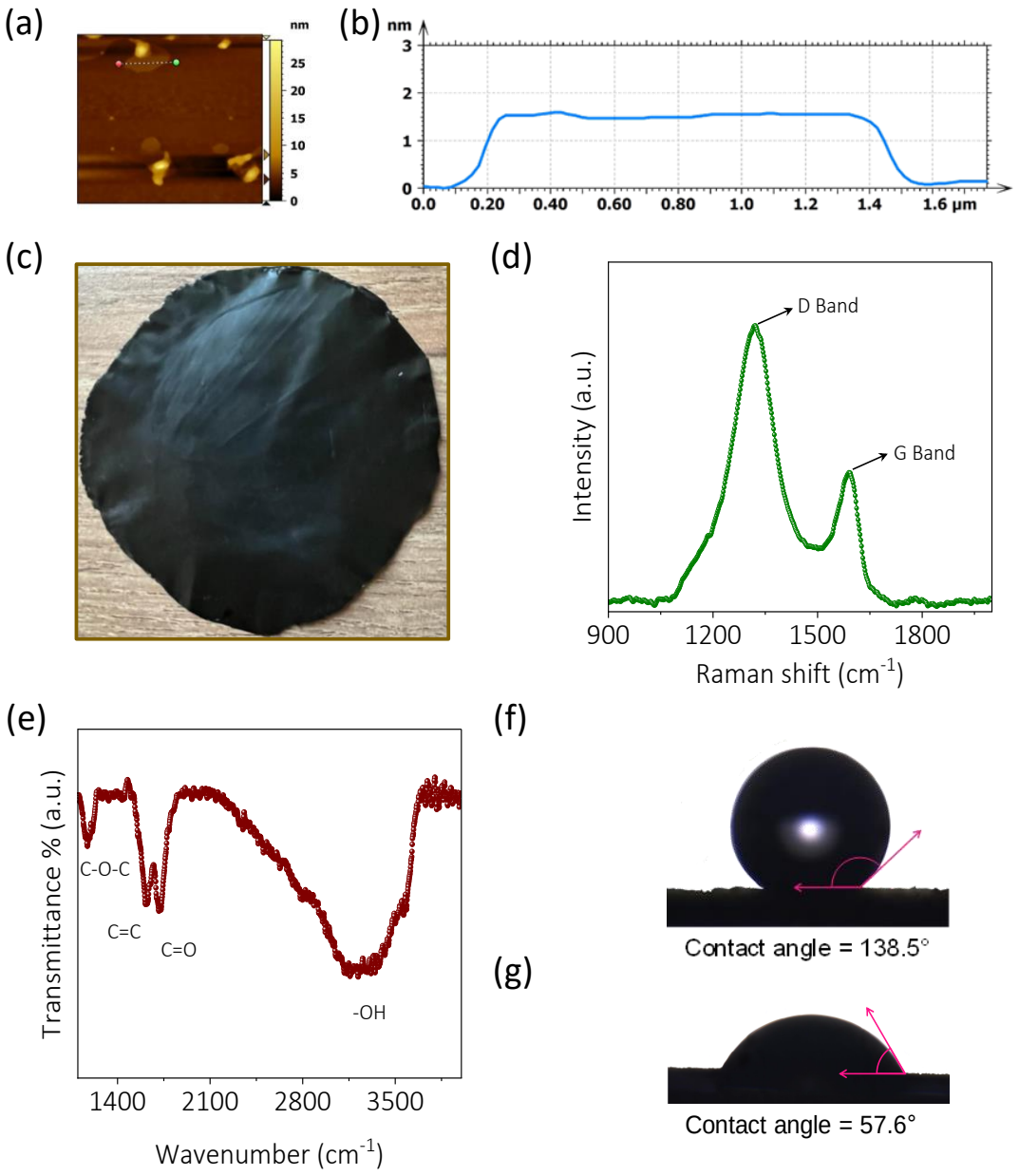

***Figure 6.1**: Characterization of graphene oxide (GO). (a) AFM image and (b) height profile of synthesized GO. (c) Photograph of the GO membrane. (d) Raman spectra of GO membrane. (e) FTIR spectra of GO membrane. Contact angle of (f) graphitic carbon (starting material) and (g) GO membrane.*

expansion of nearly 3 A° along with peak broadening, suggesting the increase in the inter-planar distance because of interlayer water molecules (Figure 6.2c,d). This expansion of the material with the rise in RH% can be attributed to the water molecule incorporation into the interlayers, affirming the hygroscopic nature of the membrane.

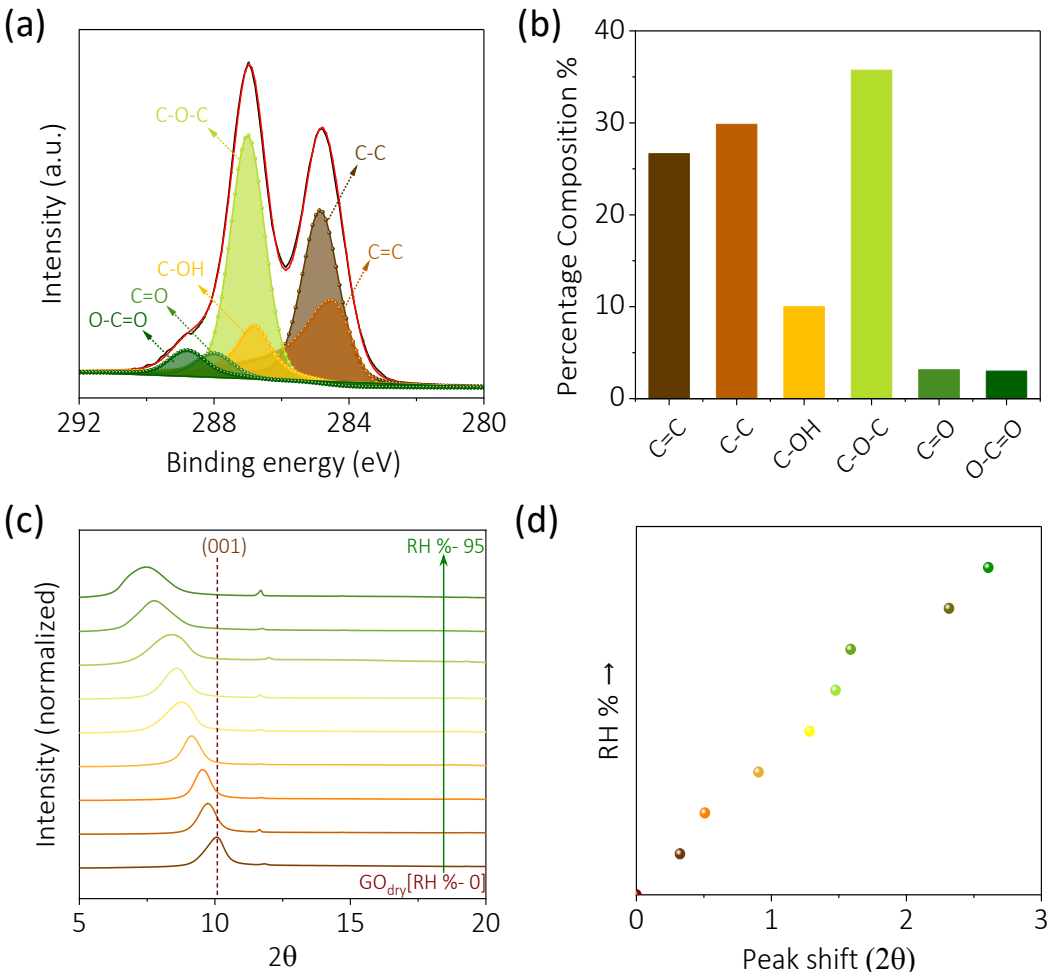

***Figure 6.2**: X-ray photoelectron spectra of GO membrane. (a) de-convoluted C1s regime and (b) percentage composition of various functionalities. XRD analysis of GO membrane (c) at varying RH% and (d) the observed peak shift.*

To elucidate the extent of hygroscopicity, water dynamic studies were conducted on the synthesized GO membrane as well as the standard proton-conducting Nafion membrane of similar dimensions (Figure 6.3). Both membranes demonstrated a positive trend toward water uptake (Figure 6.3a). The performancemetrics were further analyzed with water uptake percentage (WU%) which is the amount of water uptake with respect to the mass of the membrane (equation 2.11) and hydration number (λ) (equation 2.12) which is the number of water molecules a functionality can hold [17–19].The estimated values $WU\%_{GO}$ were ~ 4 $WU\%_{Nafion}$ and λ_{GO} were ~ 11 λ_{Nafion} attesting to the remarkable hygroscopicity of GO membrane (Figure 6.3b, c). The hydrophilic functionalities increase the hydrophilicity as well as hygroscopicity evident from hydration number adding to this its ability for capillary water condensation helps to achieve a faster rate of sorption of atmospheric water ((Figure 6.3d). This characterization attests to the successful synthesis of

GO membrane with fair incorporation of the oxygenated functionality that can promote proton transport with simultaneous atmospheric water uptake.

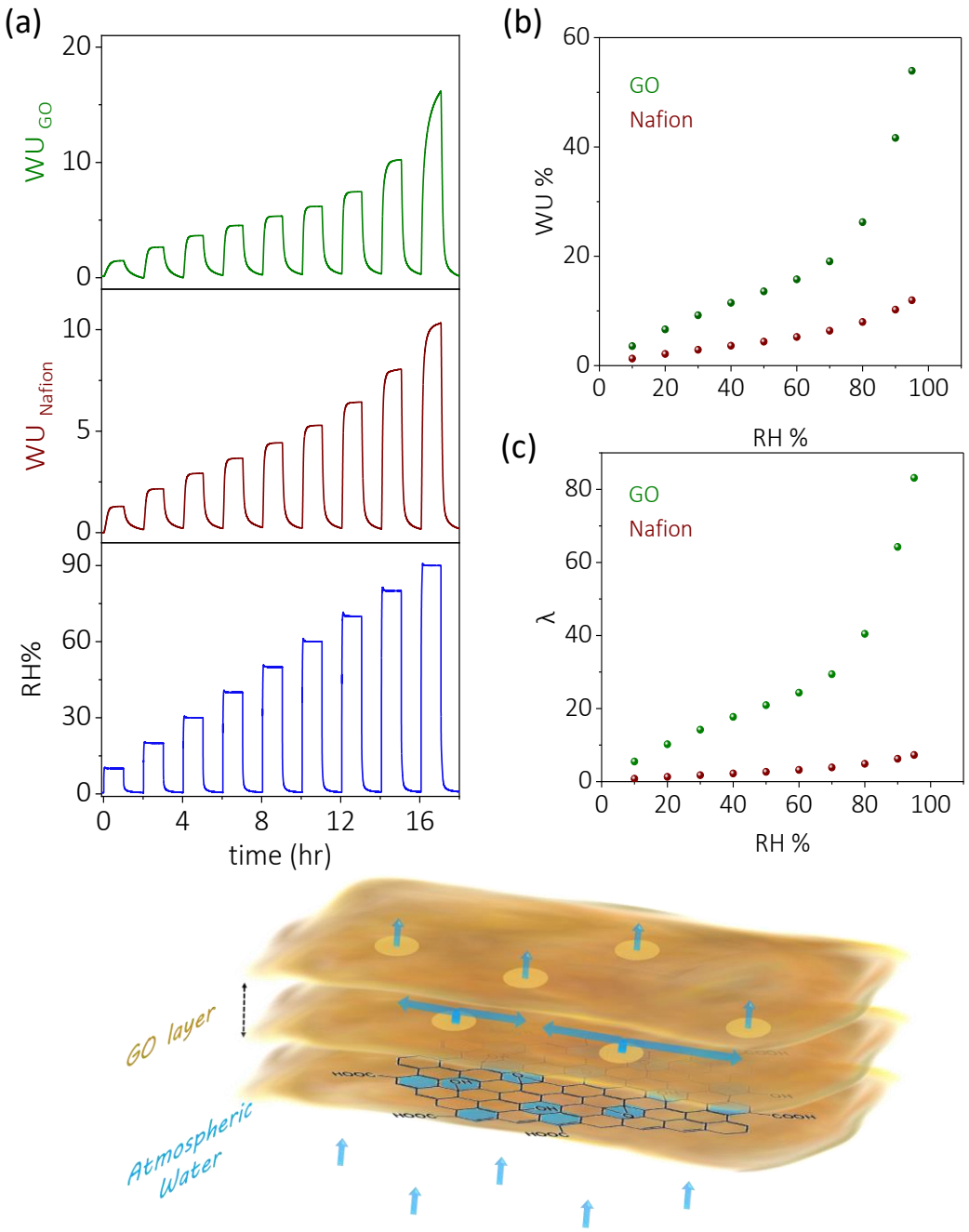

***Figure 6.3**: Water dynamic studies. (a) amount of water uptake (WU) (in mg) by GO membrane (green trace, top panel) and Nafion membrane (brown trace, middle panel) at varying RH% (blue trace, bottom panel). (b) water uptake percentage (WU %) with respect to mass of membrane vs RH% of GO membrane (green trace) and Nafion membrane (brown trace). (c) Hydration number (λ) vs RH% of GO membrane (green trace) and Nafion membrane (brown trace). (d) Schematics of atmospheric uptake affected by capillary action, hydrophilic functionalities (water captivated via hydrophilic functionalities in (blue) and water channels in blue).*

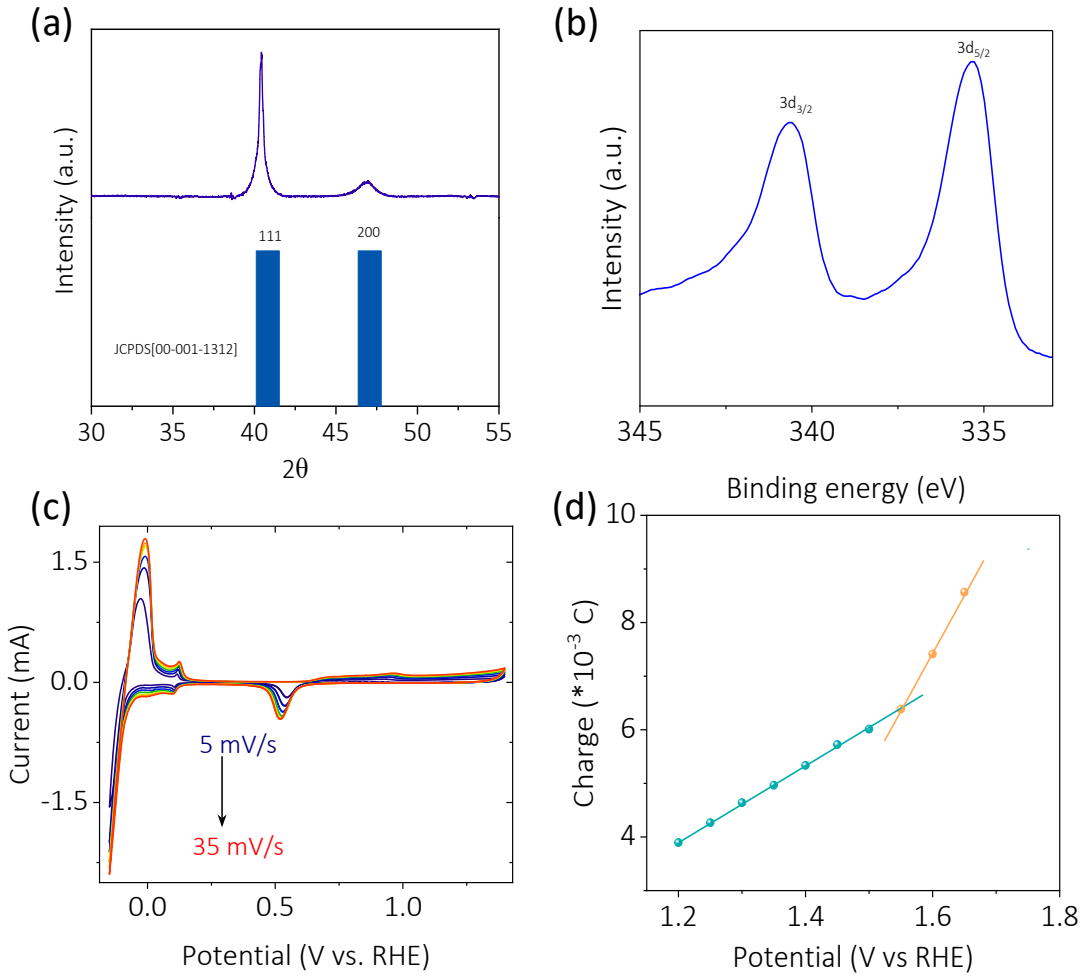

***Figure 6.4**: Characterization of palladium black. (a) XRD pattern, (b) XPS analysis, (c) cyclic voltammogram at varying scan rate in 0.5 M H_2SO_4. (d) Charge vs potential plot for calculating electrochemical active surface area of palladium black.*

The electro-catalytic material active towards oxygen evolution reaction (OER)/oxygen reduction reaction (ORR) at the positive electrode was fabricated by combining Pt black with iridium oxide/ruthenium oxide to maximize its efficiency towards atmospheric water splitting and oxygen reduction reaction[20,21]. The negative electrode for the proposed battery is expected to be a material active towards electro-catalytic hydrogen generation with simultaneous hydrogen storage with the ability to release hydrogen on demand. The benchmark catalyst for HER/HOR is platinum however, it can't be utilized as it is incapable of storing hydrogen beyond a monolayer[22,23]. Palladium is known to be active towards hydrogen evolution reaction (HER)/ hydrogen oxidation reaction (HOR) as well as uptake and release of hydrogen in its bulk by reversible palladium hydride formation. It is a solid solution of hydrogen in palladium, with best values of hydrogen

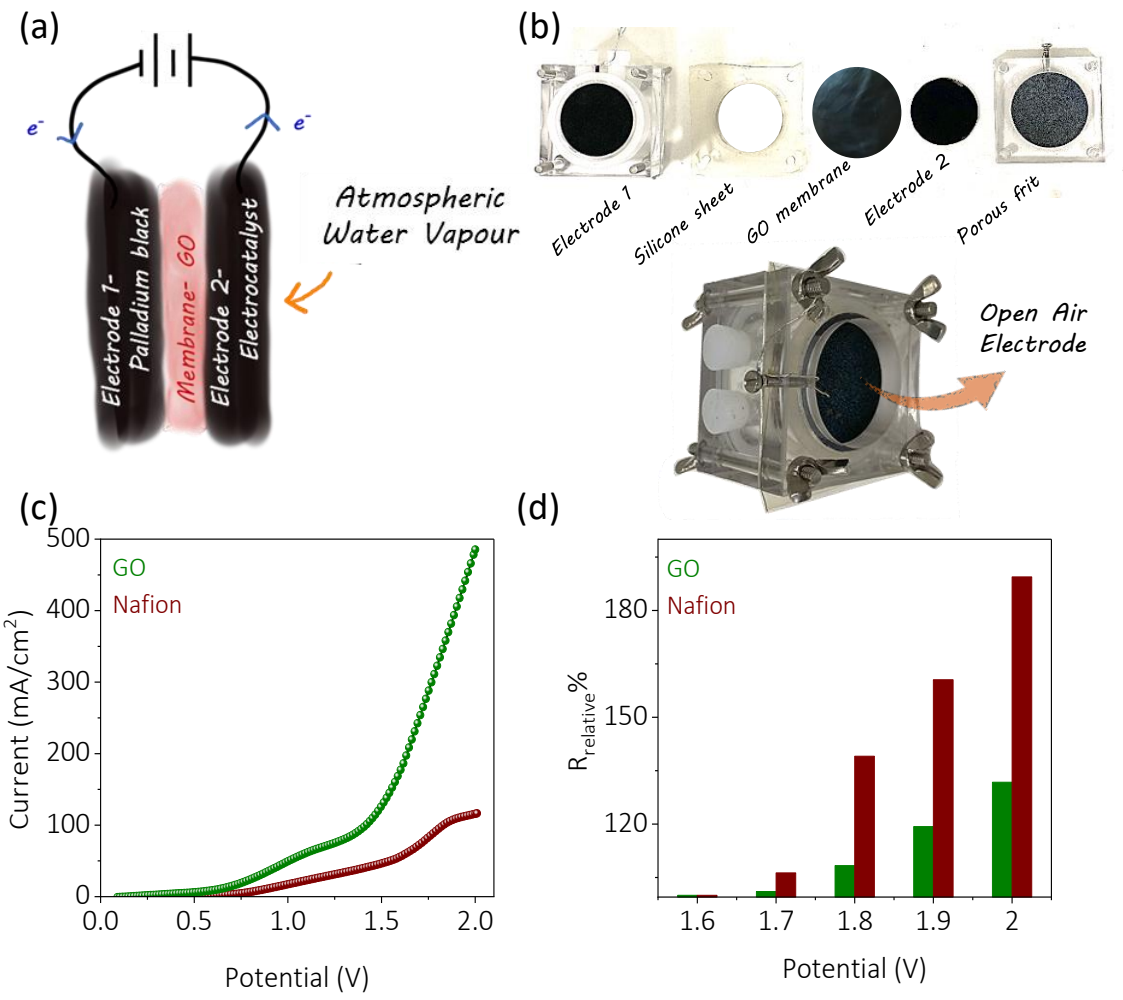

***Figure 6.5**: (a) Schematic representation of the atmospheric water battery. (b) Photograph of all the battery components and fabricated device with the positive electrode open to air. (c) Linear sweep voltammogram of the fabricated device with GO membrane (green trace) and Nafion membrane (brown trace) at a scan rate of 1 mV/s. (d) Relative electrolytic resistance observed at various operating potentials of the battery with respect to 1.6 V for GO membrane (green trace) and Nafion membrane (brown trace).*

uptake as high as 1000 times its volume[24,25] and therefore, Pd black was chosen as the negative electrodefor simultaneous HER and reversible hydrogen storage. The synthesized palladium black was characterized with powder XRD and XPS analysis. XRD analysis confirms the face-centered cubic phase (JCPDS 00-001-1312) (Figure 6.4a). The XPS analysis shows metallic palladium (Pd^0) features with asymmetric peaks at 335.2 eV and 340.5 eV corresponding to $Pd3d_{5/2}$ and $Pd3d_{3/2}$ with a difference of nearly 5.26 eV (Figure 6.4b). The electrochemical analysis of the synthesized palladium black demonstrates HER/HOR capability along with hydrogen adsorption/desorption features and the electrochemical active area of the material (ECSA) was calculated from equation 2.3 to be nearly 12.6 m^2/g (Figure 6.4c,d).

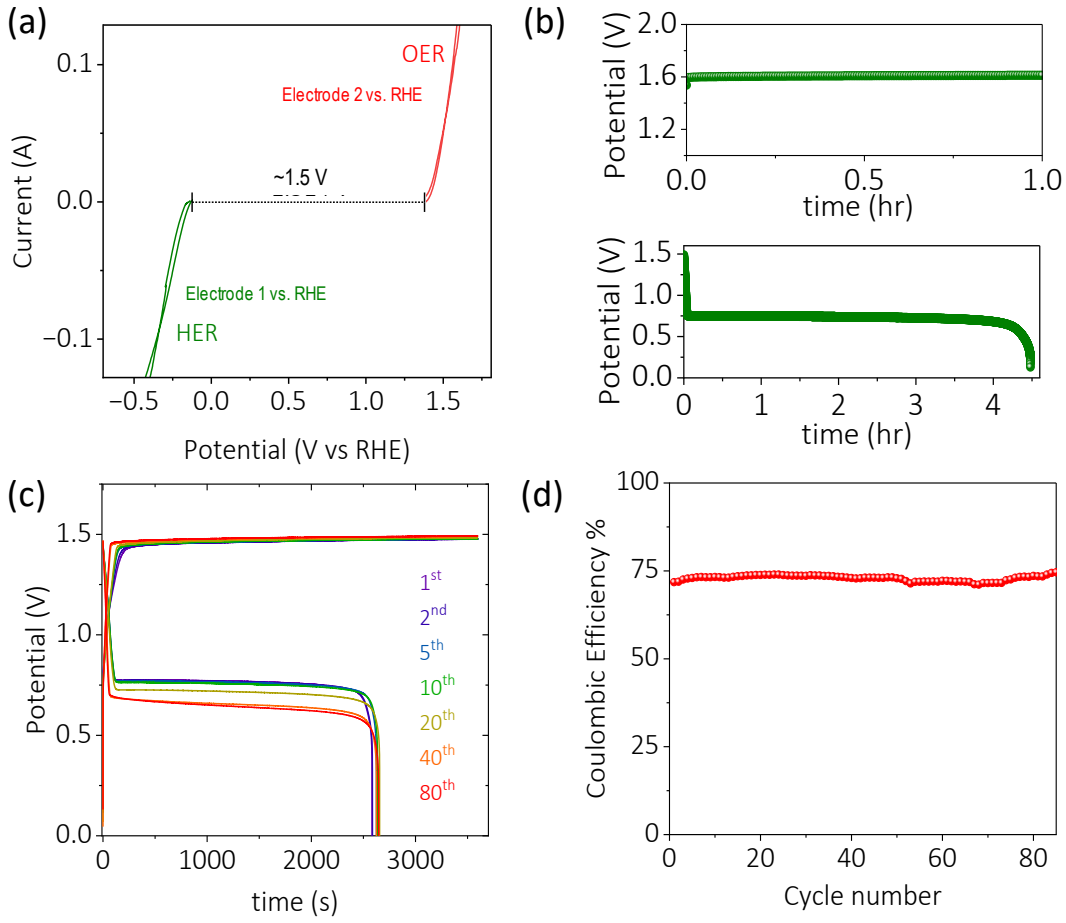

***Figure 6.6**: (a) The battery cyclic voltammogram obtained in three electrodes with an internal reversible hydrogen electrode (RHE) as reference electrode at a scan rate of 1 mV/s (electrode-1 response green trace and electrode 2 response red trace). (b) Battery charged at a constant potential of 1.6 V for an hour (top panel) and discharged at a current of 10 mA/cm^2(bottom panel). (c) Galvanostatic charge- discharge of the battery at 10 mA/cm^2. (d) Coulombic efficiency of battery during galvanostatic charge-discharge at 10 mA/cm^2.*

The battery was fabricated with the hygroscopic GO membrane sandwiched between the negative electrode (palladium black (Pd@C) with a loading of 2.5 mg/cm^2) and the positive electrode (Pt/IrO_x/RuO_x @Ti mesh with a loading of 2 mg/cm^2). The positive half-cell was kept open to the atmosphere to facilitate the uptake of atmospheric water (Figure 6.5a,b). Performance metrics of the device fabricated with GO membrane exhibited around 4 times higher performance than that of Nafion incorporated device (Figure 6.5c). Further, the internal electrolytic resistance of the device at varying operating potentials was monitored with impedance spectroscopy, and the relative resistance with respect to that at 1.6 V ($R_{relative}$%) was estimated. An increase in resistance was observed for both the devices along with the operating potentials, however, resistance increase was dominant for the Nafion incorporated device as

compared to GO at each operating potential (Figure 6.5d). The absorbed atmospheric water is not only the reactant but also a key component in proton transport between the electrodes. With the rise in the operating potential, there is an increase in electrochemical water oxidation, which is supposed to decrease the membrane water content unless and until it is simultaneously replenished by atmospheric water uptake. Therefore, the GO membrane with its higher water uptake capability dictates performance metrics by reducing the internal electrolytic resistance.

The individual electrode response in the battery configuration was obtained with battery cyclic voltammograms in three electrodes with an internal reversible hydrogen electrode (RHE) as the reference electrode at a scan rate of 1 mV/s. The current-potential response from both the battery electrodes with respect to the RHE was monitored simultaneously. The signals obtained clearly point out the oxygen evolution reaction (OER) [water oxidation/water splitting] at the negative electrode (red trace) with the simultaneous oxygen evolution reaction (HER) on the other electrode (green trace) (Figure 6.6a). The onset potentials at both electrodes marked a difference of nearly 1.5 V, (Figure 6.6a) which should be the minimum potential required to charge the battery. Therefore, the atmospheric water absorbed by the GO membrane is oxidized by the device suggesting that the device functions as an electrolyzer during the battery charge. In order to check the feasibility of the device as an electrolyzer as well as battery, the device was first charged at a constant potential of 1.6 V for an hour (Figure 6.6b, top panel), and the device could be discharged at 10 mA/cm^2 for as long as nearly 4.5 hr (Figure 6.6b, bottom panel). These studies confirm the successful fabrication of a device that can harvest atmospheric water, store the hydrogen, and release it on demand. The galavanostatic charge–discharge cycles of the device were carried out at 10 mA/cm^2, which demonstrates decent cyclability of the system (Figure 6.6c). Further, the columbic efficiency of the system exhibited a value of nearly 73% (Figure 6.6d).

Battery chemistry at the anode and cathode was elucidated by utilizing different in-situ electrochemical techniques. To understand the battery chemistry on the open-air side, an in-situ electrochemical mass spectrometry technique was utilized. The outlet from the positive electrode was connected to the mass spectrometry analyzer throughout span of the experiment. A constant potential of 1.7 V was applied to the battery, and the corresponding positive current indicates the battery is in charge mode. The simultaneous mass spectrometry analyzer provides positive signals for oxygen evolution (Figure 6.7a, b). The presence of oxygen signal was only for the duration of application of the constant potential of 1.7 V, confirming it to be a product of the electrochemical reactions during charge. The in-situ electrochemical mass

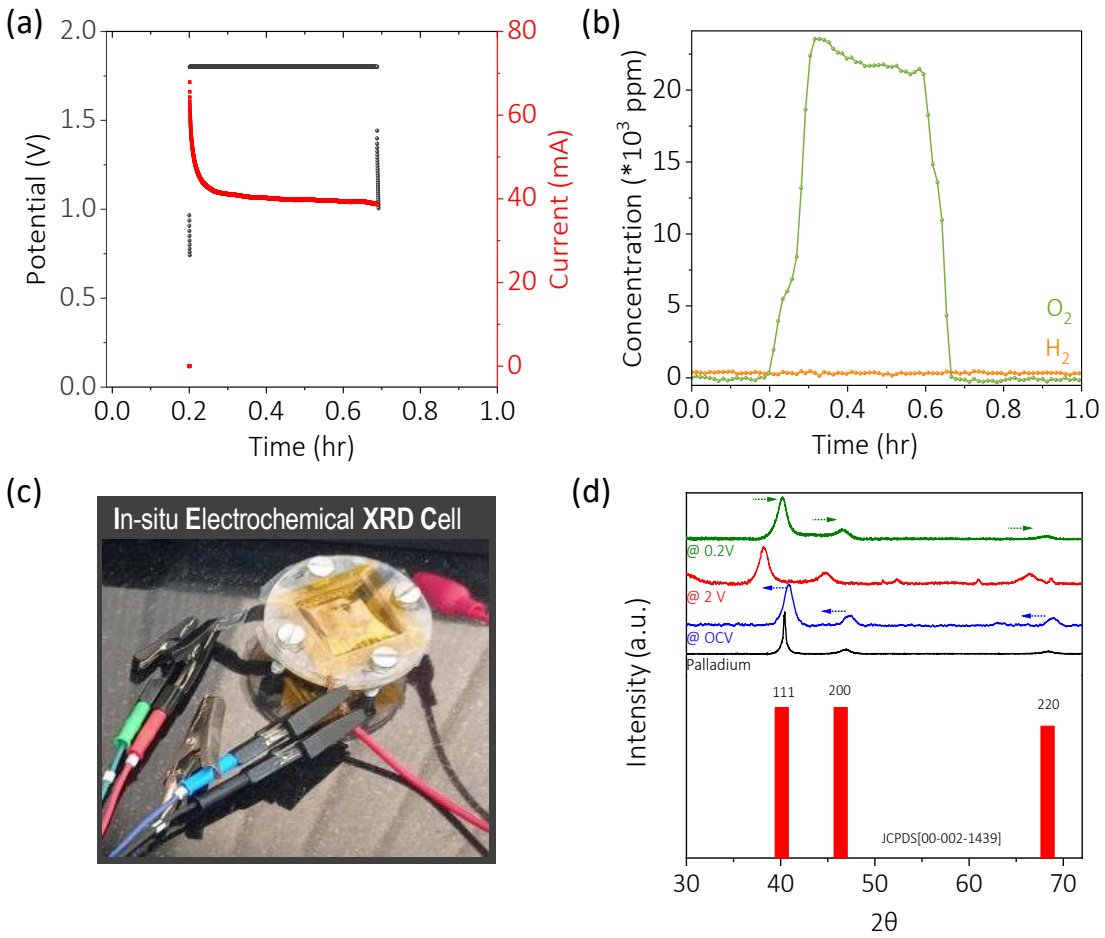

***Figure 6.7**: (a) Current vs time (red trace) graph obtained on application of 1.7 V (black trace) and the simultaneous (b) electrochemical mass spectra of the cathode exhaust showing the presence of oxygen (green trace). In-situ electrochemical XRD analysis of anode. (c) Photograph of the home made in-situ electrochemical XRD cell. (d) XRD pattern of Pd standard (JCPDS 00-001-1312, red bars), ex-situ powder XRD pattern of palladium (black trace), and in-situ electrochemical XRD pattern of Pd at open circuit potential (blue trace), at 2 V (red trace) and at 0.2 V (green trace).*

spectrometry analysis attests that on the battery charge, atmospheric water was absorbed by the GO membrane and is then electrochemically oxidized leading to oxygen evolution. Further, to understand the battery chemistry at the negative electrode, in-situ electrochemical XRD analysis of the Pd was carried out with a homemade in-situ electrochemical XRD cell (Figure 6.7c). XRD pattern of the negative electrode in the in-situ cell at open circuit potential (OCP) was analogous to JCPDS 00-001-1312, demonstrating three key peaks corresponding to [111], [200], [220] with a lattice parameter of nearly 3.85 A° (Figure 6.7d). On battery charge at 2 V, all the key peaks were found to downshift by a value of nearly 2.6 units (2 theta), altering the lattice parameter to nearly 4.04 A° with a difference of about 0.2 A° (Figure 6.7d). However, the evolution of any new peaks was absent with the intensity ratio of the existing peaks being intact. All of these

observations confirm the expansion of the crystal without any alteration to the crystal symmetry on battery charge. It's known that on hydrogen uptake, palladium expands without any alteration of the crystal symmetry. The modification of the lattice parameter of Pd from nearly ~3.85 A° to ~4.04 A° attests to the formation of palladium hydride, β-PdH_x where x can be 0.5 or higher [26–29]. These affirms that on battery charge the negative electrode-palladium converts to palladium hydride, resulting in the expansion of the crystal. On battery discharge at 0.2 V, the XRD patterns regain back to that of at the OCP, the release of stored hydrogen from palladium. These in-situ electrochemical analysis, confirms that on battery charge the atmospheric water absorbed by GO membrane is splitted, releasing oxygen at the positive electrode with simultaneous hydrogen storage at the negative electrode as palladium hydride (Scheme 6.2a, eq.6.1, eq. 6.2). During the battery discharge, these stored hydrogen is released prompting the palladium hydride to palladium conversion at the negative electrode with the release water to the atmosphere (Scheme 6.2b, eq.6.3, eq. 6.4).

Battery Charge

Electrode 1: $Pd + 2H^+ + 2e^- \rightarrow 2Pd\text{-}H$ (eq.6.1)

Electrode 2: $H_2O \rightarrow O_2 + 2H^+ + 2e^-$ (eq.6.2)

Battery Discharge

Electrode 1: $2Pd\text{-}H \rightarrow Pd + 2H^+ + 2e^-$ (eq.6.3)

Electrode 2: $O_2 + 2H^+ + 2e^- \rightarrow H_2O$ (eq.6.4)

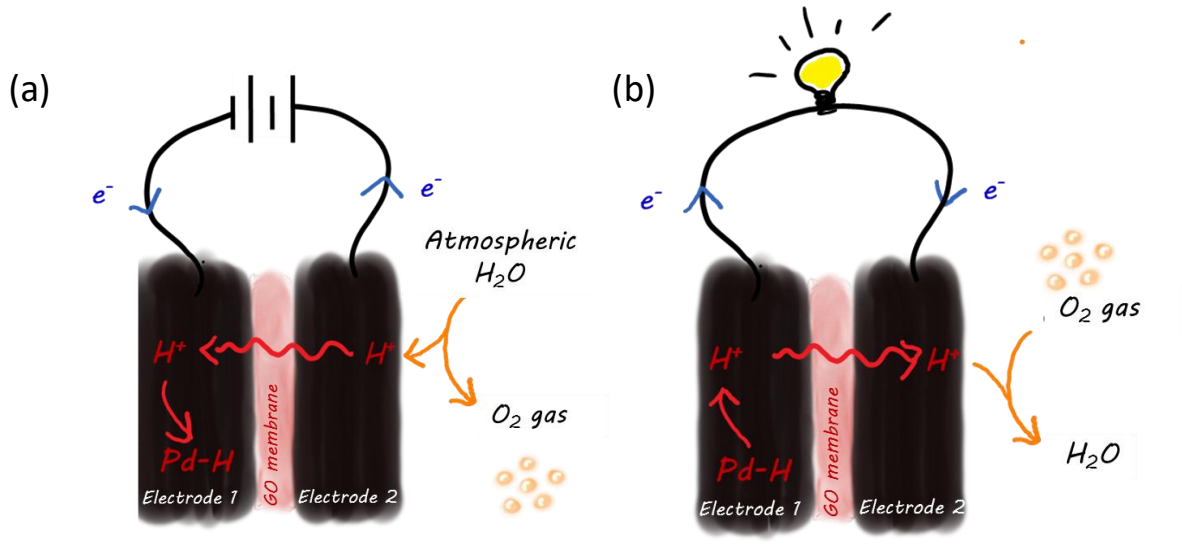

***Scheme 6.2**: Schematic representation of battery on (a) charge and (b) discharge.*

Conclusion:

A rechargeable atmospheric water battery is demonstrated which combines the three facets of hydrogen economy in a single device. The device uptakes and splits atmospheric water, and stores the hydrogen at the negative Pd electrode. This hydrogen is released on demand during electricity production. The device consists of a hygroscopic GO membrane to uptake atmospheric water and reversible hydrogen storage at a palladium-based electrode which facilitates electrochemical water oxidation during battery charge and the reverse during battery discharge. In-situ electrochemical techniques evidence the involvement of protons during the charge–discharge chemistry and extended cycling. The integration of hydrogen production, storage, and utilization in a single device holds significance for improving efficiency, reducing infrastructure complexity, and promoting the use of clean and versatile hydrogen as a key component of future energy systems. This approach aligns with the broader goals of sustainable energy development and has the potential for a low-carbon energy economy.

References:

1 A. J. Sangster, *Int. J. Sustain. Green Energy*, 2014, **3**, 115.

2 M. K. Hubbert, *Science*, 1949, **109**, 103–109.

3 A. Rehman, M. M. Alam, I. Ozturk, R. Alvarado, M. Murshed, C. Işık and H. Ma, *Environ. Sci. Pollut. Res.*, 2023, **30**, 9699–9712.

4 UN-Energy, *Energy Compacts – Annual Progress Report* 2022

5 UNEP, *Emissions Gap Report 2023: Broken Record – Temperatures hit new highs, yet world fails to cut emissions (again)*, United Nations Environment Programme, 2023, vol. 164.

6 International Energy Agency, *Net Zero by 2050: A Roadmap for the Global Energy Sector*, 2021.

7 UNSD & IEA, *Tracking SDG7: The Energy Progress Report 2023*, 2023.

8 S. Bourne, *Fuel Cells Bull.*, 2012, **2012**, 12–15.

9 M. Ball and M. Wietschel, *Int. J. Hydrogen Energy*, 2009, **34**, 615–627.

10 A. Roy and S. Pramanik, *Int. J. Hydrogen Energy*, 2023, **49**, 792–821.

11 D. Pashchenko, *Renew. Sustain. Energy Rev.*, 2023, **173**, 113117.

12 N. Armaroli and V. Balzani, *ChemSusChem*, 2011, **4**, 21–36.

13 CMS Law - Legal Services*, Facing the Future of Hydrogen: An International Guide,* 2021, vol. 1.

14 P. Muthukumar, A. Kumar, M. Afzal, S. Bhogilla, P. Sharma, A. Parida, S. Jana, E. A. Kumar, R. K. Pai and I. P. Jain, *Int. J. Hydrogen Energy*, 2023, **48**, 33223–33259.

15 W. Gao, G. Wu, M. T. Janicke, D. A. Cullen, R. Mukundan, J. K. Baldwin, E. L. Brosha, C. Galande, P. M. Ajayan, K. L. More, A. M. Dattelbaum and P. Zelenay, *Angew. Chemie Int. Ed.*, 2014, **53**, 3588–3593.

16 M. R. Karim, K. Hatakeyama, T. Matsui, H. Takehira, T. Taniguchi, M. Koinuma, Y. Matsumoto, T. Akutagawa, T. Nakamura, S. Noro, T. Yamada, H. Kitagawa and S. Hayami, *J. Am. Chem. Soc.*, 2013, **135**, 8097–8100.

17 Y. Zheng, U. Ash, R. P. Pandey, A. G. Ozioko, J. Ponce-González, M. Handl, T. Weissbach, J. R. Varcoe, S. Holdcroft, M. W. Liberatore, R. Hiesgen and D. R. Dekel, *Macromolecules*, 2018, **51**, 3264–3278.

18 T. Maneerung, J. Liew, Y. Dai, S. Kawi, C. Chong and C. H. Wang, *Bioresour. Technol.*, 2016, **200**, 350–359.

19 R. Lin, J. Liu, Y. Nan, D. W. Depaoli and L. L. Tavlarides, *Ind. Eng. Chem. Res.*, 2014, **53**, 16015–16024.

20 M. E. G. Lyons and S. Floquet, *Phys. Chem. Chem. Phys.*, 2011, **13**, 5314.

21 R. Frydendal, E. A. Paoli, B. P. Knudsen, B. Wickman, P. Malacrida, I. E. L. Stephens and I. Chorkendorff, *ChemElectroChem*, 2014, **1**, 2075–2081.

22 Z. Ma, C. Chen, X. Cui, L. Zeng, L. Wang, W. Jiang and J. Shi, *ACS Appl. Mater. Interfaces*, 2021, **13**, 44224–44233.

23 G. A. Kamat, J. A. Zamora Zeledón, G. T. K. K. Gunasooriya, S. M. Dull, J. T. Perryman, J. K. Nørskov, M. B. Stevens and T. F. Jaramillo, *Commun. Chem.*, 2022, **5**, 20.

24 G. L. Holleck, *J. Phys. Chem.*, 1970, **74**, 503–511.

25 H. Kobayashi, M. Yamauchi, R. Ikeda, T. Yamamoto, S. Matsumura and H. Kitagawa, *Chem. Sci.*,

2018, **9**, 5536–5540.

26 J. A. Eastman, L. J. Thompson and B. J. Kestel, *Phys. Rev. B*, 1993, **48**, 84–92.

27 A. Maeland and T. B. Flanagan, *Platin. Met. Rev*, 1966, **10**, 20–23.

28 R. J. Wolf, M. W. Lee and J. R. Ray, *Phys. Rev. Lett.*, 1994, **73**, 557–560.

29 J. E. Schirber and B. Morosin, *Phys. Rev. B*, 1975, **12**, 117–118.

Chapter 7:

Summary and future outlooks

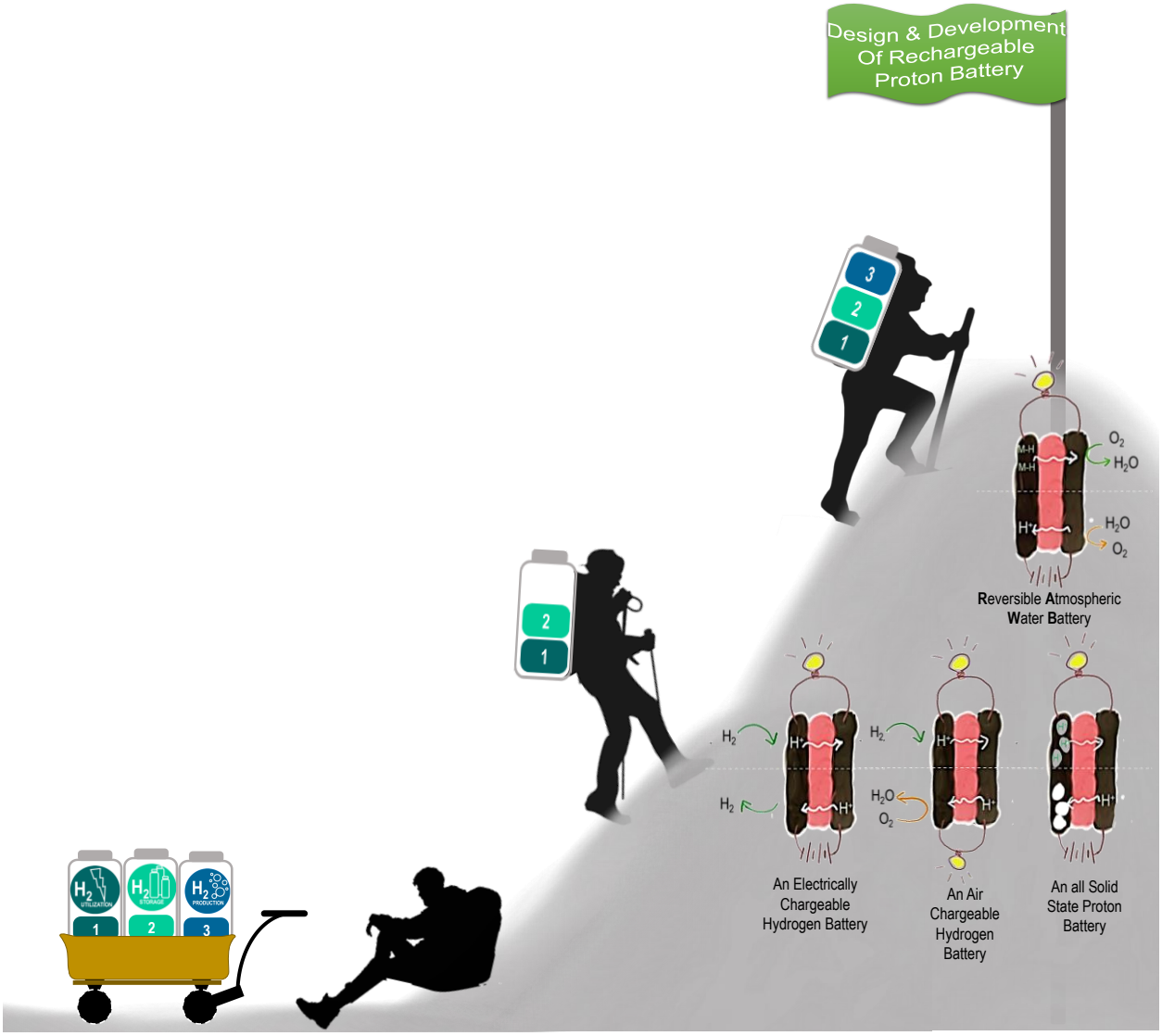

Scheme 7.1: *Schematic representation of the thesis titled "Design and development of rechargeable proton battery".*

This Chapter provides a brief summary and future outlook of the work reported in this thesis. The major aim of thesis is to combine the three key steps of hydrogen economy in a single device. In this context, the first three working Chapters (Chapter 3-5) deal with the integration of hydrogen storage and hydrogen utilization in a single device. In Chapter 3, to enable this integration, gaseous hydrogen was coupled with a

hydrogen storing organic molecule leading to an electrically chargeable hydrogen battery. In Chapter 4, this electrically chargeable hydrogen battery is transformed into air chargeable hydrogen battery by coupling the hydrogenation/dehydrogenation chemistry of the organic molecule with the oxygen redox reactions. In order to avoid the direct usage of gaseous hydrogen, in Chapter 5, the anodic half-cell is modified with a hydrogen storing transition metal oxide whose reversible hydrogen storage potential is close to the redox reactions of gaseous hydrogen. Chapter 6 deals with the integration of all the aspects of hydrogen economy in a single device. To enable this integration, atmospheric water is harvested as a source for molecular hydrogen by utilizing hygroscopic GO membranes. The produced hydrogen is stored in Pd based electrocatalyst whose utilization is enabled by coupling it with an air electrode during the discharge chemistry. This way, all the three key aspect of hydrogen economy such as hydrogen production, hydrogen storage and hydrogen utilization are combined in a single device by harvesting atmospheric water (Scheme 7.1). Nevertheless, efforts to integrate the key aspects of hydrogen economy is executed with precious metal based electrocatalysts. Therefore, in order to bring down the overall cost of the device, non-precious catalyst development is of extreme importance. Higher temperature operation is questionable with a GO membrane as it can get reduced at higher temperatures. This required development of robust proton conducting membranes which can simultaneously capture atmospheric water while maintaining chemical as well as mechanical integrity at higher temperatures. Nevertheless, the demonstration of combining the three major components of hydrogen economy in a single working device offer prospects for implementing a zero carbon footprint.

List of Publications

First Author Publications

- **Neethu Christudas Dargily**, Ravikumar T., Zahid M. Bhat, Mruthyunjayachari C. D., Alagar Raja K.,Manu Gautam, Muhammed Musthafa O. T. **(2018)**. A Rechargeable Hydrogen Battery. *The Journal of Physical Chemistry Letters*, 9(10), 2492–2497.
- **Neethu Christudas Dargily**, Ravikumar T., Mruthyunjayachari C. D., Muhammed Musthafa O. T. **(2022)**. An Air Chargeable Hydrogen Battery by Reversible Electrochemical Trapping of the Protons. *Green Chemistry* 24, 8820-8826.
- **Neethu Christudas Dargily**, Giddaerappa K., Rahul M., Ravikumar T., Surbhi Sharma, Muhammed Musthafa O. T. **(2023)**. Electro Fenton's Reaction Coupled Zn-Air Battery for In-situ Pollutant Degradation. *Green Chemistry,* 25, 8652-8660

Co-author Publications

- Alagar Raja K., Shabbah Begum, Mohammed Azeezulla N., **Neethu Christudas Dargily**, Mruthyunjayachari C. D., Zahid M. Bhat, Muhammed Musthafa O. T. **(2020)**. Unprecedented Isomerism–Activity Relation in Molecular Electrocatalysis. *The Journal of Physical Chemistry Letters*, 11(1), 263–271.
- Zahid M. Bhat, Deepraj P., Shane Ardo, Ravikumar T., Alagar Raja K., **Neethu Christudas Dargily**, Mruthyunjayachari C. D., Muhammed Musthafa O. T. **(2020)**. An Electrochemical Neutralization Cell for Spontaneous Water Desalination. *Joule*, 4, 1–13.
- Sanchayita M., Alagar Raja K., Zahid M. Bhat, **Neethu Christudas Dargily**, Muhammed Musthafa O. T. **(2020)**. Isomerism-Activity Relation in Molecular Electrocatalysis: A Perspective. *Electroanalysis*, 32, 2387 – 2392.
- Manu Gautam, Zahid M. Bhat, Abdul Raafik, Le Vot S, Mruthyunjayachari C. D., Alagar Raja K., **Neethu Christudas Dargily**, Ravikumar T., Olivier Fontaine, Muhammed Musthafa O. T. **(2021)**. Coulombic Force Gated Molecular Transport in Redox Flow Batteries. *The Journal of Physical Chemistry Letters*, 12 (5), 1374–1383.
- Zahid M. Bhat, Ravikumar T., **Neethu Christudas Dargily**, Abdul Raafik, Alagar Raja K, Mruthyunjayachari C D, Mahesh Itagi, Harish M.N.K., Stefan A. Freunberger, Muhammed Musthafa O. T. **(2021)**. Ambient Condition Alcohol Reforming to Hydrogen with Electricity Output. *ACS Sustainable Chemistry & Engineering* 9(8), 3104–11.
- Ravikumar T., Manu Gautam, Zahid M. Bhat, Abdul Raafik, Mruthunjayachari C.D., Sanchayita M., **Neethu Christudas Dargily**, and Muhammed Musthafa O. T. **(2021)**. An Atmospheric Water Electrolyzer for Decentralized Green Hydrogen Production. *Cell Reports Physical Science,* 2(11), 100627.
- Shambhulinga A., Ravikumar T., Zahid M. Bhat, Mruthyunjayachari C. D., **Neethu Christudas Dargily**, Sanchayita M., Alagar Raja K., Muhammed Musthafa O. T. **(2022)**. Wireless Chemical Charging of a Metal-Ion Battery by Magnetic Particles. *ACS Sustainable Chemistry & Engineering*, 10(1), 259–66.
- Sur, S., Ravikumar T., Zahid M. Bhat, **Neethu Christudas Dargily**, Sanchayita M., Liu, X., Cai, P., Wen, Z., and Muhammed Musthafa O. T. **(2022)**. Hybrid Alkali–Salt–Acid Electrochemical Device for Electricity-Efficient Desalination and H_2 Generation. *ACS Sustainable Chemistry & Engineering* 10, 10781–10788.

A Rechargeable Hydrogen Battery

Author:
Neethu Christudas Dargily, Ravikumar Thimmappa, Zahid Manzoor Bhat, et al

Publication: Journal of Physical Chemistry Letters

Publisher: American Chemical Society

Date: May 1, 2018

PERMISSION/LICENSE IS GRANTED FOR YOUR ORDER AT NO CHARGE

This type of permission/license, instead of the standard Terms and Conditions, is sent to you because no fee is being charged for your order. Please note the following:

- Permission is granted for your request in both print and electronic formats, and translations.
- If figures and/or tables were requested, they may be adapted or used in part.
- Please print this page for your records and send a copy of it to your publisher/graduate school.
- Appropriate credit for the requested material should be given as follows: "Reprinted (adapted) with permission from {COMPLETE REFERENCE CITATION}. Copyright {YEAR} American Chemical Society." Insert appropriate information in place of the capitalized words.
- One-time permission is granted only for the use specified in your RightsLink request. No additional uses are granted (such as derivative works or other editions). For any uses, please submit a new request.

If credit is given to another source for the material you requested from RightsLink, permission must be obtained from that source.

BACK CLOSE WINDOW

An air chargeable hydrogen battery by reversible electrochemical trapping of the protons

N. Christudas Dargily, R. Thimmappa, M. C. Devendrachari and M. O. Thotiyl, *Green Chem.*, 2022, **24**, 8820 **DOI:** 10.1039/D2GC02927H